Cosmic Ray Anomalies and Positrons from the Dark Side

Aaron C. Vincent

Department of Physics

McGill University
Montréal, Québec
April 2012

A thesis submitted in partial fulfilment
of the requirements for the degree of

Doctor of Philosophy

Abstract

This thesis examines two recent anomalous cosmic ray (CR) positron detections in the context of the ongoing search for the particle nature of dark matter (DM), which composes 85% of the matter content of the Universe. The first CR anomaly, detected by the European INTEGRAL/SPI experiment via 511 keV gamma rays from the center of the Galaxy, suggests an unaccounted-for production of low-energy positrons in the region surrounding the galactic center (GC). We model the production of electron-positron pairs from the decay or interaction of cold dark matter in an Einasto profile. We show that the INTEGRAL signal can be fit by scattering DM in a halo with the shape parameters predicted by many-body simulations, with a significance on par with previous phenomenological fits, but with six fewer degrees of freedom. This can be achieved with annihilating low-mass DM, or with scattering of excited dark matter (XDM), with cross-sections compatible with thermal WIMP production in the early universe. The second CR anomaly is the rising positron fraction from 10 to 200 GeV observed by the PAMELA satellite and confirmed by NASA's Fermi-LAT. Although previous studies had considered Sommerfeld-enhanced DM annihilation as a possible source, they did not consider the full impact of the dark matter substructure predicted to exist by simulations. We show that including this substructure can give a better fit to the PAMELA and Fermi data, but that this is not sufficient to overcome the strict gamma-ray bounds from the Fermi-Large Area Telescope (LAT) diffuse gamma ray data. We finally show that a single, nearby subhalo can explain the excess, while simultaneously avoiding gamma ray and dipole anisotropy constraints, and that it is possible to create a Sommerfeld-enhanced particle physics model that produces the required annihilation cross-section and is compatible with cosmological bounds.

Résumé

Nous examinons dans cette thèse deux détections récentes de positrons dans le rayonnement cosmique, dans le contexte d'une origine possible sous la forme de matière sombre (MS). Quoique celle-ci englobe 85% de la matière dans l'univers, sa détection jusqu'à présent ne s'est faite que par son intŕaction gravitationnelle. La première anomalie, observée par le satellite Européen INTEGRAL via un excès de rayons gamma de 511 keV issus du centre de la Voie Lactée, suggère une production élevée de positrons dans cette région. En modélisant la production de paires d'électrons-positrons par la décomposition ou l'intéraction de MS dans un profil Einasto, nous obtenons un ajustement d'aussi bonne qualité que les meilleures études précedentes purement phénomńologiques, mais avec six degrés de liberté en moins. Ceci peut être réalisé avec l'annihilation de MS d'environ 1 MeV, ou avec la diffusion de MS à plusieurs niveaux d'énergie (XDM) de masse élevée, avec des sections efficaces consistantes avec la production thermique de WIMPs au début de l'Univers. La deuxième anomalie, mesurée par le satellite PAMELA et confirmée par le Large Area Telescope (LAT) de Fermi, est constituée d'une fraction de positrons qui s'élève de 10 à 200 GeV et qui ne peut être expliquée par le spectre d'antimatière secondaire attendu. Quoique des études précédentes ont considéré une explication en terme de MS qui s'annihile à l'aide d'un mécanisme de Sommerfeld, nous avons été les premiers à examiner l'impact des milliers de subhalos (SH) de MS qui devraient exister selon les simulations numériques. Nous démontrons que l'inclusion des SH donne un meilleur ajustement aux données de PAMELA et Fermi, mais que ce n'est pas suffisant pour obéir aux limites établies par les observations gamma de Fermi-LAT. Nous montrons finalement qu'un seul SH très proche pourrait expliquer l'anomalie PAMELA, sans enfreindre les contraintes de rayonnement gamma et d'anisotropie dipolaire actuelles et qu'il est possible de créer un modèle de physique des particules qui produit la section efficace nécéssaire et qui est toutefois consistante avec les limites établies par la cosmologie.

DEDICATION

This thesis is dedicated to my parents Connie and Warwick, the most devoted and passionate scientists I know.

"More power!" — *Sifu P'ng Chye Khim, 1939-2010*

ACKNOWLEDGEMENTS

For chapter 2, I thank Evan Mcdonough for his contributions to our skymap models, and I thank the anonymous referee for insightful comments that helped to improve our presentation. For chapters 3 and 4, I thank Ilias Cholis for kindly giving us access to his modifications to the GALPROP code, and Troy Porter for valuable help with the Fermi data analysis. I thank Ran Lu, Scott Watson and Neal Weiner for helpful discussions and correspondence concerning GALPROP.

I also thank all of the great postdocs and graduate students in the High Energy Theory group at McGill, for the many insightful, educational and creative discussions both at McGill and in the many great restaurants and brewpubs of Montréal.

I thank my evaluation committee Guy Moore, Matt Dobbs, Vicky Kaspi and Tony Moffat for their corrections and suggestions, as well as for great questions and insightful comments during my thesis defense. Finally, I am deeply grateful to my supervisor Jim Cline for ensuring the excellent quality both of the science and its presentation in these studies, as well as the other work I have undertaken throughout my Masters and PhD. His attention to detail and insistence on scientific rigor and clarity have greatly sharpened the quality of the work presented here, and my own approach to research in physics would not have been the same without him.

Statement of Originality

This thesis is based on original research carried out with collaborators James Cline, Pierrick Martin and Wei Xue, and is presented here with their permission.

- Chapter 2 was published as ref. [1] and examines the dark matter contribution to the morphology of the INTEGRAL/SPI 511 keV excess. This was the first study to statistically demonstrate that a dark matter model can explain the 511 keV signal with as much significance as the usual phenomenological parametrization. I performed the modelling and numerical computations, as well as the analysis of the maximum likelihood ratio (MLR) results, including results presented in the tables and figures.

- Chapter 3 is based on ref. [2]. It concerns the impact of the distribution of Milky Way dark matter subhalos on the observation of cosmic ray positrons, and was the first study to account for the subhalo contribution to the PAMELA/Fermi flux. I performed all of the simulations with GALPROP, which included my own modifications of the code, and the main results presented in the paper come from my numerical calculations. I was also responsible for a large fraction of the writing.

- Chapter 4 is based on ref. [3], a follow-up to the previous item, and examines the impact of gamma rays from the models described in Chapter 3. It was the first consistent picture of gamma-ray constraints from the model of ref. [2]. Again, I was responsible for the numerical elements of this study including DM halo modelling, cosmic ray propagation, as well as the computation of inverse-Compton gamma rays. I was responsible for most of the writing, especially sections I-IV.

Table of Contents

List of Figures

List of Tables

Chapter 1

Introduction

The modern picture of particle physics was truly born in the 20th century with the powerful realization that many laws of physics are governed by simple symmetries of nature: Lorentz invariance, CP symmetry, rotational invariance, and the various gauge symmetries of the standard model of particle physics. If symmetries provide the laws, then their systematic breaking provides the structure: for example the Higgs mechanism gives particles the masses we observe today, and the breaking of matter-antimatter symmetry early in the history of the universe has allowed the formation of galaxies, stars, planets and the myriad phenomena of everyday life.

Finding hints of these symmetries, for example by observing the production of antimatter in nature, therefore provides us clues about physics at energy scales much higher than that of everyday physics. The motivation behind this thesis is to examine two unexplained sources of positrons in the cosmos — one at low energies, the other at high energies — as a possible portal to the physics of the dark sector, separated from the standard model in the hot, early universe.

The central theme in Chapters 2, 3 and 4 is the particle nature of dark matter. We will therefore begin with a review of the relevant DM physics. We will then proceed to introduce the low-energy (Section 1.2) and high-energy (Section 1.3) positron anomalies which motivated the in-depth studies that make up the body of this thesis.

1.1 Dark Matter

Our understanding of the Universe and its composition has figuratively exploded over the past century. The rapid development of observational technology during the 20th century first allowed astronomy to progress beyond simple $F = ma$ mechanics, and then ushered in an era of "precision cosmology." Measurements on scales that range from stars, galaxies, clusters and large-scale structure all the way to the boundary of the visible universe — an astounding 13.5 billion light-years — provide an unprecedented picture of our Universe. This has allowed for an amazing range of theoretical and observational discoveries: the number of cosmology and astrophysics-related Nobel prizes awarded has grown from one in the entire first half of the 20th century,[1] to a much more respectable 8 since the 1970s. This includes the 2011 prize awarded to Perlmutter, Schmidt and Riess, for the 1997 discovery of the accelerated expansion of the universe.

This progress has brought cosmology to a rather humbling impasse, however. Indeed, careful accounting puts only 4% of our universe in the form of baryonic matter that we understand — the leptons, quarks and photons of the standard model of particle physics. The rest is in two forms:

- 74% is dark energy, responsible for the accelerated expansion of the universe, and
- 22% is dark matter, which has the same gravitational behavior as baryonic matter, but with very weak interactions with itself and other matter.

Our focus will be on the second component, which is by far the most important on galactic scales: the missing 85% of the matter content of the universe. Beginning with a short historical overview, I will lay out the necessary background to connect this mysterious form of matter to observational cosmic ray physics.

[1] It could even be argued that Hess's 1936 prize, "For the discovery of cosmic radiation" was only accidentally astrophysical in nature.

1.1.1 A short observational history

The first hints of a hidden sector of matter came from local stellar motions observed by Oort in 1932 and from the orbital velocities of galaxies in the Coma cluster by Zwicky in 1933. The easiest way of estimating the mass distribution of a stable system is to measure its components' velocities relative to the centre of mass. By applying the virial theorem

$$2\langle T\rangle = -\langle V\rangle, \tag{1.1}$$

Zwicky found [5, 6] that to properly explain the observed relative velocities of the "nebulae" (galaxies) within the Coma cluster, an average mass-to-luminosity ratio of $\gamma = 500$ was needed. This contrasted sharply with ratios of $\gamma \sim 3$ measured in local stellar systems at the time. Even taking into account the approximations (steady state, uniform spherical distribution, ...) it was clear that counting the luminous galaxies in a cluster did not provide a good estimate of the enclosed mass.

These results remained uncorroborated until the early 1970s, when new spectroscopic techniques allowed Ruben to measure the rotational speeds of galaxies to radii that extended well beyond stellar orbits by observing the doppler shifts of lines emitted by diffuse gases. If the majority of a galaxy's mass is in the form of luminous baryonic matter such as stars and gas, equation (1.1) implies that the orbital velocity v_r of a test particle sufficiently far from the centre should follow:

$$v_r^2 \sim \frac{M}{r}. \tag{1.2}$$

where r is the distance from the galactic centre of mass, and M is the galaxy's mass. By studying the rotational velocities first of Andromeda [7], then of 21 more spiral galaxies [8], Ruben and collaborators found that rather than following (1.2), the rotational speeds at large r remained nearly constant or rose, as shown in Figure 1.1. This suggested the existence of a dark, massive matter component that extends diffusely to radii well beyond the baryonic radius of each galaxy.

Since these studies, evidence from many areas of astronomy and cosmology have contributed to the case for a dominant non-baryonic component of the matter sector.

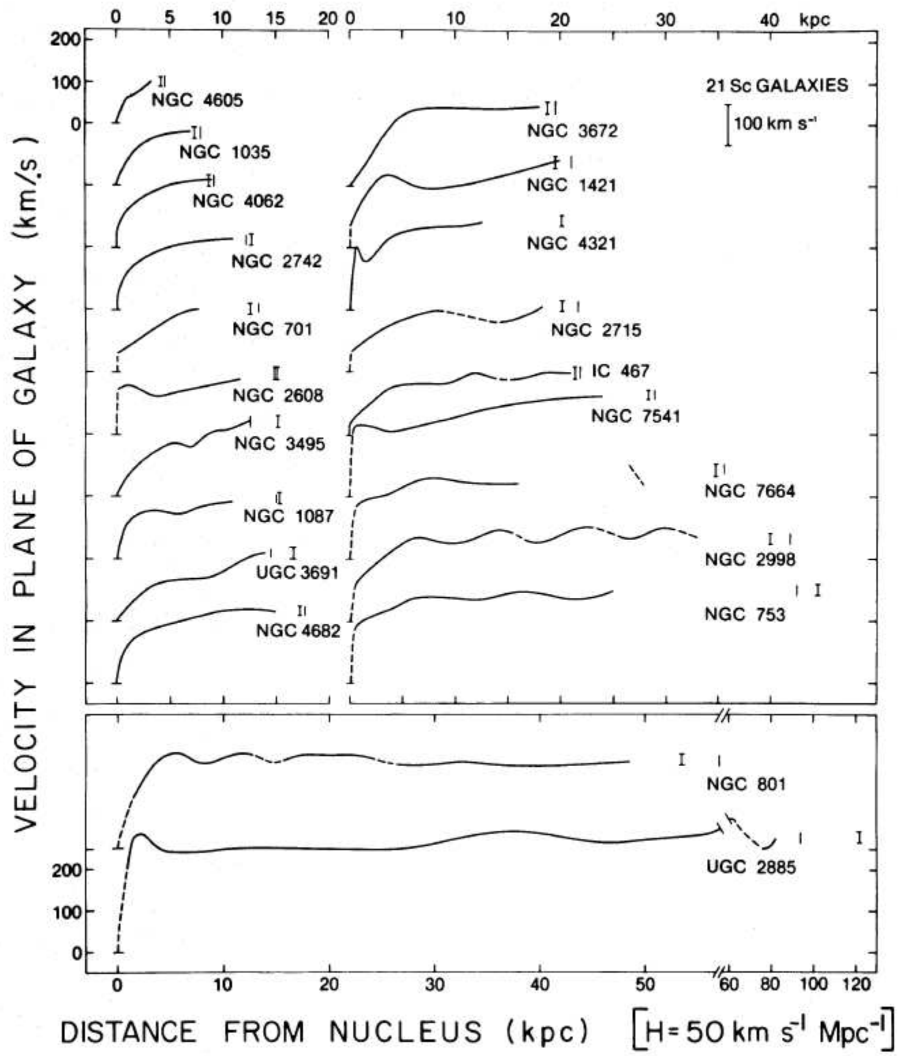

Figure 1.1: The galactic rotation curves of 21 spiral galaxies measured by Ruben *et al.* with newly available spectroscopic techniques in the 1970s. Rather than falling as $1/\sqrt{r}$ as the radius increases beyond the luminous extent (typically $\sim$ 10 kpc), the velocities remain approximately constant, or even rise, over very large radii. This implies the presence of an invisible, dominant matter component in every galaxy. Figure from [8].

While many alternate theories[2] have emerged as explanations of individual phenomena such as galactic rotation curves, DM has greater overall success in explaining disparate phenomena. Gravitational lensing is perhaps the most compelling direct piece of evidence available. By observing the lensing of light through large galaxy clusters, it is possible to infer the existence of a substantial invisible component of matter that is deflecting the light emitted by background galaxies. Further clues come from observations of the Bullet cluster, and more recently of the MACS J0025.4-1222 cluster, shown in Figure 1.2 (a). In both cases, the collision between two galaxy clusters has allowed observers to distinguish three separate components of matter: the hot baryonic gases visible in the X-ray spectrum, the individual galaxies, and the large dark matter component, visible via gravitational lensing. While the gaseous components in each collision can be seen to have merged into a distinct "blob," the invisible lensing components have passed through each other, highlighting their tiny self-interaction cross-section. Such a separation of the baryonic component from the lensing component of matter is very difficult to explain without invoking an invisible matter component.

Finally, detailed calculations from elemental nucleosynthesis, as well as fitting the the acoustic peaks of the cosmic microwave background, have strengthened the case for dark matter and in conjunction with supernova and large-scale structure data have produced the concordance model as we know it, illustrated in Figure 1.2 (b):

$$\Omega_\Lambda = 0.74 \quad \Omega_m = 0.26, \tag{1.3}$$

where Ω_Λ and Ω_m are respectively the dark energy and matter contributions to the overall density of the Universe.

[2] For example MOND, or Modified Newtonian Dynamics, which purports that long-distance (IR) corrections, *e.g.,* $\Delta\phi \propto r$, to the Newtonian potential are instead responsible for results such as Ruben's (ref. [9] provides a review of many of the various MOND theories.)

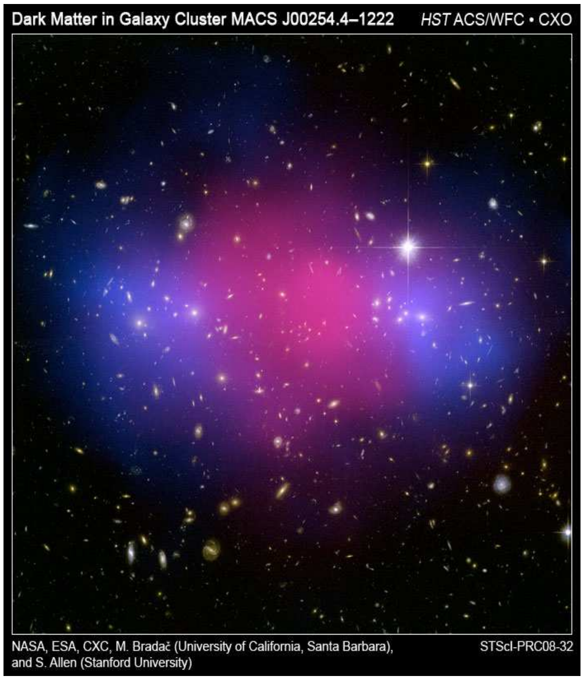

(a)

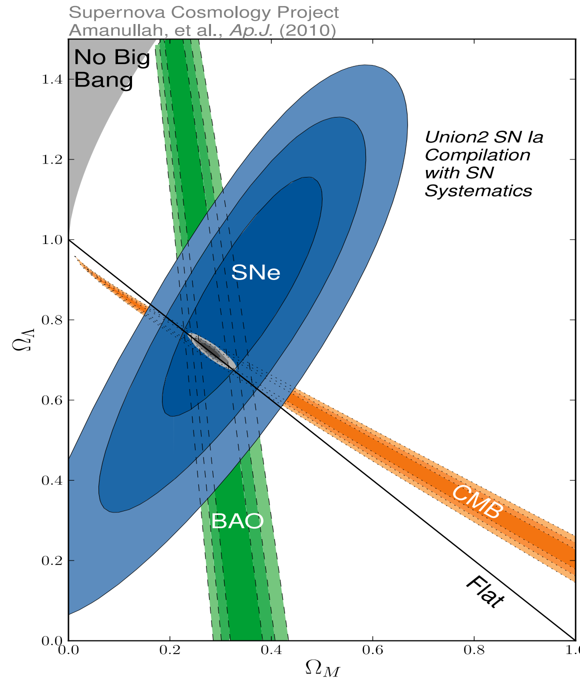

(b)

Figure 1.2: Left: X-ray (pink) and lensing (blue) map of the matter in the colliding cluster MACS J0025.4-1222. The collision has ripped the dark component from the baryonic gasses, whose interaction can be seen in the center. Image by NASA, ESA, CXC, M. Bradac (University of California, Santa Barbara), and S. Allen (Stanford University) [10]. Right: some of the observations giving rise to the concordance model of cosmology, which predicts $\Omega_\Lambda = 0.74$ and $\Omega_m = 0.26$. SNe refers to supernova redshift measurements, BAO and CMB refer to measurements of the power spectrum of baryon acoustic oscillations before decoupling. BAO measurements are of larges-scale structure (small scale oscillations), whereas CMB measurements are from direct observation of the cosmic microwave background, and constrain oscillations on large scales. Figure from [11].

1.1.2 The CDM paradigm and the WIMP miracle

Observations at all scales allow the following statements to be made about the particle nature of DM:

- DM must be sufficiently slow at redshift $z \sim 1000$ to allow the efficient collapse of structure into the galaxies and clusters observed today. A relativistic matter component would stream away and suppress structure formation. Dark matter must therefore be **cold** enough to form bound structures.[3]

- To obtain the correct properties, such as the fluffy halos required to explain measured galactic rotation curves, DM cannot be allowed to efficiently radiate energy and collapse to a lower-energy configuration like the compact disks of the baryonic component of galaxies. This implies a weak[4] coupling not only to the Standard Model (SM) photon, but to any light gauge boson that may be present in the invisible sector. Because of this, we may say that DM must be **dark**.[5]

From these constraints arises the *cold dark matter* (CDM) paradigm, upon which much of modern cosmology theory is built. Any theory of dark matter must therefore take care to preserve these properties.

There is one final element of modern DM theory that should not be overlooked. If dark matter was produced thermally in the early universe, then its abundance today is a direct measurement of the DM coupling to other sectors. As the early universe cooled, the equilibrium population of dark matter steadily decreased as it became less energetically favourable to produce DM than to destroy it. However, as soon as the rate of loss due to annihilation $-\dot{n}_{\chi,\mathrm{ann}} = n_\chi^2 \langle \sigma v \rangle_{\mathrm{ann}}$ fell below the loss due to Hubble expansion $-\dot{n}_{\chi,H} = 3Hn_\chi$, DM annihilation was no longer possible, as the particles were being diluted faster than they could find each other. This resulted in a "freeze-out" of the density. The thermally-averaged self-annihilation cross-section

---

[3] "cold" means that DM must be non-relativistic at decoupling, to allow structure to form hierarchically from smaller scales upwards. However, recent studies of the matter power spectrum, which is related to the "missing dwarf problem" have suggested that a slightly warmer DM model is preferred (see *e.g.,* [12].)

[4] We say "weak", rather than "zero" since dark matter may not be completely dark; see, *e.g.,* ref. [13].

[5] Strictly speaking, *transparent* is a more accurate descriptor.

can therefore be directly calculated from today's measured relic dark matter density. It is:

$$\langle \sigma v \rangle_{\rm ann} = 3 \times 10^{-26} {\rm cm}^3 {\rm s}^{-1}. \tag{1.4}$$

What is extraordinary is that this cross-section is of the order of magnitude of cross-sections due to weak interactions, prompting the speculation that DM could be coupled to electroweak physics. This is the origin of the so-called WIMP miracle, for *weakly interacting massive particles*. Given that extensions of the standard model such as supersymmetry generically predict new weakly-interacting particles, the WIMP miracle is often perceived as the mother of all hints that cosmology has provided us on the particle nature of dark matter. Nevertheless, WIMPs are not the only consistent models of dark matter; the WIMP miracle could simply be a numerical coincidence. The asymmetric dark matter (ADM) paradigm, for instance [14] makes use of baryogenesis to sequester the "missing" antimatter of the universe in the dark sector. In this case $n_{SM} = n_{DM}$, meaning that $m_{DM} \sim (5-15)m_p$ depending on the exact model. This naturally gives an explanation to the similar orders of magnitude of dark matter and baryons in the universe today. In this model, no present-day self-annihilation is expected. Models of non-thermally produced dark matter, such as light Peccei-Quinn axions produced coherently in a phase transition, can do equally well in providing a framework for CDM (see *e.g.* [15]).

While the models discussed in Chapters 2-4 do not rely specifically on the properties of the models described above, it will be important to preserve as much model-independence as possible. We will indeed show that the proposed DM explanations of the cosmic ray anomalies are fully consistent with the WIMP hypothesis.

1.1.3 Dark Matter in the Milky Way: many-body simulations

An aspect of dark matter physics that is highly relevant to this thesis is its distribution on galactic scales. Determining this distribution is a problem which is conceptually simple, but technically very challenging. In principle, one can study the dynamics of collapsing cold, pressureless matter by solving the fluid dynamics equations. Solving for the seven unknowns[6] $\rho, \mathbf{v}, S, \phi, p$ requires seven differential equations: the continuity equation, Euler's fluid equations, the entropy conservation equation, the Poisson equation and the equation of state. These nonlinear equations cannot be solved analytically for general initial conditions, and a numerical approach is needed. Unfortunately, the grid required to solve these equations must become intractably fine to study the nonlinearities that arise over the full collapse history.

The solution to this problem is to rather treat the dark matter as a collection of a very large number N of gravitationally interacting particles. The force acting on each particle i is:

$$\mathbf{F}_i = -\sum_{j \neq i}^{N} \frac{m_i m_j \mathbf{r}_{ji}}{|\mathbf{r}_{ji}|^3} \tag{1.5}$$

where $\mathbf{r}_{ji}$ is the vector from particle i to each other particle j in the sum. By starting with initial conditions obtained from the primordial power spectrum, it is then possible to numerically evolve the equations of motion (1.5) until today. The accuracy of the output is therefore solely dependent on the numerical resolution. The first such simulation that allowed the substructure of an evolved DM halo to be seen was performed with $N = 10^6$ particles on a single workstation and took a year to complete [16]. Subsequent advances in parallel computing have allowed simulations to exceed 10^9 particles. Recent projects that simulated the collapse of galaxy-sized collections of particles include *Aquarius* [17] and *Via Lactea II* [18].

Even with stochastic initial conditions (set by the spectrum of primordial perturbations), the results of these simulations agree remarkably well on a number of predictions. The first is a large diffuse halo, which extends well beyond the distribution of baryons and is approximately spherical, rather than disk-like. The steady state DM distribution is highly peaked in the center, and decreases as a power law with radius r. Many empirical parametrizations have been suggested for this profile.

[6] Density, the three velocity components, entropy, gravitational potential and pressure, respectively.

The most popular by far is the Navarro-Frenk-White profile:

$$\rho(r) = \rho_s \frac{2^{3-\gamma}}{(r/r_s)^\gamma (1 + r/r_s)^{3-\gamma}}. \tag{1.6}$$

where γ and r_s are parameters fit to the N-body simulation results. Other profiles have been proposed, mainly with the goal of alleviating the singularity that occurs at $r = 0$. One such distribution, of which we will make extensive use, is the Einasto profile:

$$\rho(r) = \rho_s \exp\left(- \left[\frac{2}{\alpha} \left(\frac{r}{r_s} \right)^\alpha - 1 \right] \right), \tag{1.7}$$

where, again, r_s and α are set by simulation results. Accepted values for a Milky Way-sized galaxy are $r_s = 26$ kpc and $\alpha = 0.17$ [18]. The overall normalisation ρ_s is determined from observation.

The distribution of relative velocities v_{rel} is roughly Maxwellian, with a cutoff at the escape velocity v_{esc}:

$$f(v_{\text{rel}}, \sigma) = 4\pi \frac{1}{(2\pi\sqrt{2/3}\sigma)^{3/2}} v_{rel}^2 \exp\left[-\frac{1}{2} \left(\frac{v_{\text{rel}}}{\sqrt{2/3}\sigma} \right)^2 \right] \Theta(v_{\text{esc}} - v_{\text{rel}}), \tag{1.8}$$

where Θ is the usual Heaviside step function and σ is the dispersion:

$$\sigma^2 = \sum_{i=x,y,z} \langle (v_i - \langle v_i \rangle)^2 \rangle. \tag{1.9}$$

The dispersion as a function of radius resembles the distribution in Figure 1.3.

While these profiles are very similar at radii of a few kpc and above, their shapes in the inner galaxy have been the source of some contention. Due to their finite resolution, N-body simulations cannot adequately predict the behavior of DM in the central few parsecs of a simulated galaxy. Whereas the Einasto and NFW profiles are quite cuspy in the center, some observational studies (see *e.g.,* [19]) and some simulations of dwarf spheroidals [20] which include the effect of baryons predict a flatter "cored" dark matter profile — even though other simulations such as [21] predict an *increase* in central density from the inclusion of baryons. These are complicated processes to model and to observe, and the "cusp-vs-core" issue remains largely unresolved.

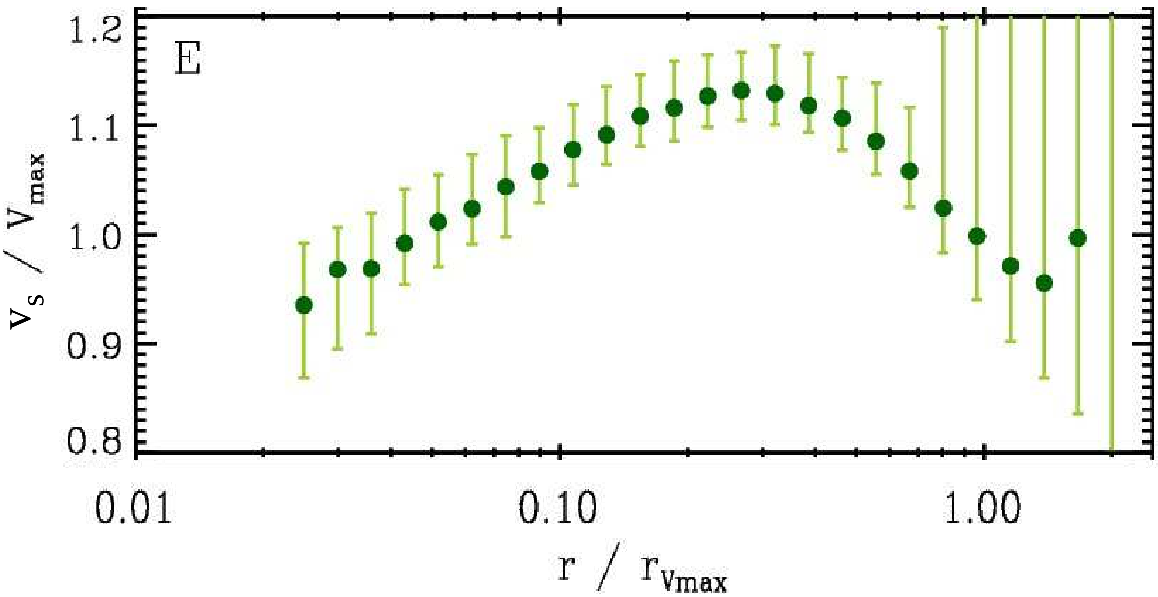

Figure 1.3: Radial velocity dispersion of subhalos in the *Via Lactea II* simulation, taken from ref. [4].

What is clear is that the general shape (1.7) is a robust prediction of CDM simulations on Milky Way scales. For this reason, it will be a central hypothesis in our modelling, even though cored profiles will also be examined for comparison. There are two final predictions of N-body simulations that will be of particular interest to us: triaxiality and substructure.

Triaxiality

Given the complicated dynamics that give rise to steady states of DM halos, it is unrealistic to expect them to be completely spherical. Simulations indeed predict (*e.g.,* [22],[21] and references therein) a degree of triaxiality $a \neq b \neq c$, where a, b and c are the scales of the respective axes. DM-only simulations predict ratios b/a and c/a as low as $0.4 - 0.6$, but the presence of baryons may soften this to $0.8 - 0.9$ [21].

Substructure

In addition to the main diffuse galactic halos, many self-similar layers of substructure are predicted to arise within every galactic object. These often-neglected subhalos are the primary focus of Chapters 3 and 4. Simulations such as *Via Lactea II* predict thousands or more subhalos which extend thousands of kpc beyond the visible galaxy. These localized overdensities are less than a kpc across and are characterized by a density profile that is also NFW or Einasto. Velocity dispersion within these subhalos is much smaller than in the main halo, meaning that Sommerfeld-like attractive forces (see Section 1.3) can lead to enhanced DM-DM interaction. These subhalos are known to contain sub-substructure, and due to the finite resolution of N-body simulations, it remains unclear how deep this recursion goes.

1.1.4 Detection of dark matter

In order to fully understand the particle nature of dark matter, we require a method of measuring its interaction with the Standard Model (SM). Such techniques come in three varieties:

Collider searches aim to produce dark matter directly, from the collision of high-energy SM particles in experiments such as the Large Hadron Collider (LHC). These would be seen by detectors as missing energy in a collision. While collider searches can give very precise data on mass and cross-section of new particles, they cannot by themselves tell whether this new particle is dark matter, or some other new particle that simply lives long enough to escape the detectors.

Direct detection experiments aim at directly observing the "wind" of DM that the Earth is constantly streaming through, by searching for nuclear recoils from DM-nucleus collisions. These obviously depend greatly on the local DM properties, and require very stringent control over backgrounds such as cosmic ray particles and radioactive decays from the surrounding environment, including the detectors themselves. For this reason, experiments must be carried out deep underground. Such experiments include CRESST [23], Xenon [24], CoGeNT [25], PICASSO [26] and CDMS [27].

Indirect detection involves searching for the signature of dark matter decay, scattering or annihilation. If these processes' final states contain SM particles, we should observe an overabundance of such products in regions known to be DM-rich, such as satellite galaxies or the Galactic center.

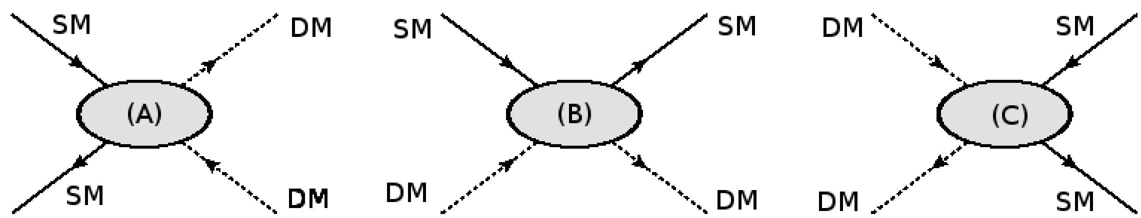

Figure 1.4: Sketch of the three possible methods of detecting particle dark matter, which can be seen as crossings of the same Feynman diagram. A) Direct production of DM in colliders; B) direct detection by scattering with SM particles; and C) indirect detection by observing the products of DM annihilation, scattering and decay in space.

From a theoretical point of view, these three detection methods probe the same physics, but in slightly different ways; this is illustrated in Figure 1.4. A fully confirmed detection of particle dark matter will therefore require agreement between all three channels. While the first two aspects have been the focus of much attention in the past few years, we will concentrate on the final aspect: indirect detection. The most obvious signature of dark matter decay or annihilation in the region around our galaxy would be the presence of gamma-ray lines from processes such as $\chi\chi \to \gamma\gamma$, where χ is the dark matter particle. The photons in this case would have an energy $E_\gamma = m_\chi$, producing an unmistakable signature of a new particle. So far, searches by gamma-ray telescopes such as the Fermi Large Area Telescope (LAT) have only placed upper bounds on these processes [28]. More indirect tools must be used if the decay or annihilation is to heavy SM particles. Such searches can include:

(I) the final-state radiation accompanying the production of charged particles (FSR);

(II) bremsstrahlung and inverse-Compton scattering from daughter particle interactions with the interstellar medium;

(III) detection of decay or annihilation products of the daughter particles and

(IV) direct detection of the cosmic ray particles themselves on Earth.

If these daughter particles consist of electron-positron pairs, these processes are all relevant. As will be shown in detail, low-energy positrons will be mainly visible via (III), whereas at high energies processes (I), (II) and (IV) will be important.

With this background in mind, we may now turn to the two anomalies behind the originial work presented in this thesis. Firstly, the low-energy positrons seen in the galactic center by the INTEGRAL/SPI experiment, and secondly the high-energy positrons observed near Earth by the PAMELA and Fermi-LAT experiments.

1.2 Positron anomalies: low energy

The first paper, presented in Chapter 2, is motivated by large flux of 511 keV photons that is observed to come from the direction of the galactic center. First observed in 1972 [29], this signal appeared as a bump around 470 keV on top of the expected gamma-ray continuum. Subsequent balloon experiments [30] were able to confirm that this was indeed a peak at $E_\gamma = 511$ keV — exactly the mass of the electron. This unambiguously points to an origin of these gamma-rays: a steady annihilation of electron-positron pairs near the galactic center.

In the 1990's, the NASA CGRO/OSSE[7] space-borne experiment was able to confirm this signal, and to show that in addition to a diffuse bulge component in the inner galaxy, a disk-like structure could be seen in the 511 keV sky [31].

The most recent, and by far most precise data from the 511 keV sky come from the ESA's INTEGRAL/SPI[8] experiment. SPI has been gathering gamma-ray data in the 20 keV to 8 MeV range, with a spectral resolution of around 2 keV, since INTEGRAL's launch in 2002. SPI has a 16° field of view, and a sensitivity of 2×10^{-5} photons cm^2 at 511 keV. As of now, eight years of observational data are publicly available. What is quite amazing about this particular signal is that its shape, a bulge-to-disk ratio $B/D > 1$ illustrated in Figure 1.7, is not observed at *any other frequency* of the EM spectrum.

[7] Compton Gamma Ray Observatory/Oriented Scintillation Spectrometer Experiment.

[8] INTErnational Gamma-Ray Astrophysics Laboratory/SPectrometer for Integral.

It should be noted that gamma-ray astronomy in the MeV range is very difficult. Not only are the observed event rates quite low (an average of one photon per 10 minutes in the case of the 511 keV line), but it is a region that is intrinsically noise-dominated. Since the atmosphere is opaque to gamma-rays, balloon or space-borne detectors must be used. These are subject to elevated fluxes of cosmic ray particles, which create high-energy secondary particles including nucleons, mesons and charged leptons, as well as radioactive isotopes. The decays of these secondary particles, as well as the beta and gamma radiation from the radioactive species create a very large gamma-ray background with a spectrum that falls within the region of observational interest. In addition to the continuum background, over 300 gamma-ray lines due to these processes were catalogued and identified by [33] and [34]. For these reasons, it has taken 40 years to obtain the current picture of the 511 keV sky.

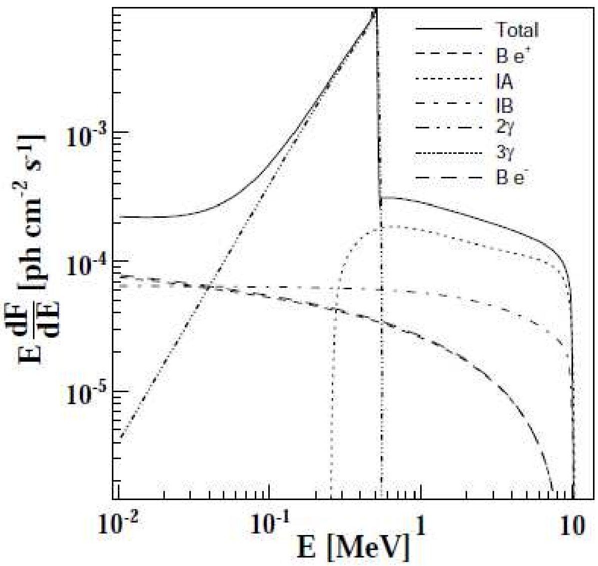

Figure 1.5: The spectrum expected from positrons injected into the interstellar medium ISM at 10 MeV. B e^+, e^-: Bremsstrahlung; IA: in-flight annihilation; IB: internal Bremsstrahlung; 2γ and 3γ: p-Ps and o-Ps contributions, respectively. (Figure from [32]).

As will be shown, the signal observed by INTEGRAL/SPI is not consistent with any known astrophysical source of positrons. After a brief introduction to positron astrophysics, we will motivate the need for a component such as dark matter to explain the SPI observations.

1.2.1 Positron annihilation

When a positron meets an electron, the annihilation releases at least $2m_e = 2\times 511$ keV of radiation. This can occur *in-flight*, creating two back-to-back photons, or via the formation and subsequent decay of the bound state *positronium*. Much like the ground state of the hydrogen atom, positronium can occur in two spin states: para-positronium (p-Ps), a singlet state in which the e^+ and e^- spins are anti-aligned, giving a total angular momentum $L = 0$; or ortho-positronium (o-Ps), a triplet state in which the spins are aligned and the angular momentum is $L = 1$.

The decay products of positronium must conserve angular momentum: p-Ps can therefore decay to two back-to-back 511 keV photons, whereas o-Ps must produce an odd number of photons, whose energies can be distributed in the continuum up to 511 keV. Thus, by observing the ratio between the continuum below 511 keV and the intensity of the 511 keV peak, it is possible to infer the fraction of signal originating from positronium decay versus in-flight annihilation. This is called the positronium fraction [35]:

$$f_{Ps} = \frac{8I_{\mathrm{continuum}}/I_{\mathrm{peak}}}{9 + 6(I_{\mathrm{continuum}}/I_{\mathrm{peak}})}. \tag{1.10}$$

Measuring f_{Ps} can give important information about the interstellar medium (ISM) in which positron annihilation is occurring [36]. Conversely, an accurate value of f_{Ps} is required to predict the amplitude of the 511 keV signal from a given positron source model.

The continuum *above* 511 keV provides information on the positrons themselves. If positrons are created and injected into the ISM at relativistic energies, one expects additional spectral components [32]:

- Line broadening due to the Doppler shift of the 511 keV signal;
- high-energy bremsstrahlung;
- internal bremsstrahlung, or final-state radiation, associated with the production of the positrons; and
- inverse Compton scattering, associated with the interaction of the e^+ with the interstellar radiation field (ISRF).

These contributions are illustrated in Figure 1.5.

1.2.2 INTEGRAL/SPI Observations

Over eight years of observation, the spectrometer on board the INTEGRAL satellite has clearly identified a flux of 1.7×10^{-3} photons per second at 511 keV, 1.05×10^{-3} ph s^{-1} of which comes from a circular region of radius $\sim 8°$ around the galactic center [37], once background has been accounted for. This corresponds to a luminosity of about $10^3 L_\odot$. Given a measured positronium fraction $f_{Ps} = 0.97$ [36], the signal implies an annihilation of approximately 1.5×10^{43} positrons every second in a spherical region of a few kiloparsecs surrounding the galactic center, in addition to a fainter $0.3 \times 10^{43} e^+ s^{-1}$ in an extended disk-like region confined to the galactic plane. If a steady state is assumed, this means that the *creation* of $\sim 1.8 \times 10^{43}$ positrons every second must be accounted for. Put differently, this corresponds to 3 solar masses-worth of antimatter being created — and annihilating — in the Milky Way over its lifetime! The spectrum around 511 keV observed by INTEGRAL/SPI, illustrated in Figure 1.6, also provides useful information. The observed flux below the peak is slightly higher than the continuum background. This can be modeled by an orthopositronium continuum. Conversely, there is no excess at energies above the peak: this tells us that the positrons responsible for the SPI observation are being injected into the ISM at energies $E_{e^+} \lesssim 3$ MeV. As we shall see, this provides a useful constraint on the possible origin of these positrons. Finally, the peak itself can be modeled by a broad line and a

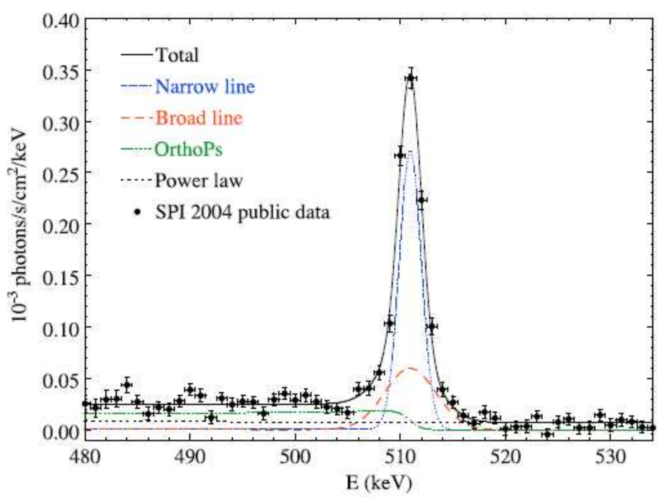

Figure 1.6: Spectrum observed by the INTEGRAL/SPI experiment around 511 keV. (Figure from [36]).

narrow line contribution, which is consistent with positronium formation occurring in a mix of neutral warm and ionized warm interstellar media [36].

In the context of Chapter 2, the morphology of the 511 keV signal in the sky is of particular interest. While the balloon results of the 1970's placed the origin of the 511 keV line at or near the galactic center, it took the skymaps of OSSE and then SPI to give a more complete view of the 511 keV sky. Since the fourth year of SPI data, the disk component has clearly been visible in addition to the bulge, an axisymmetric source that extends approximately 10 degrees from the galactic center. Due to the high backgrounds, the 511 keV data cannot be plotted directly. We must rather rely on reconstructions that depend on a background and source model. One recent reconstruction is shown in Figure 1.7. The most recent INTEGRAL observations put

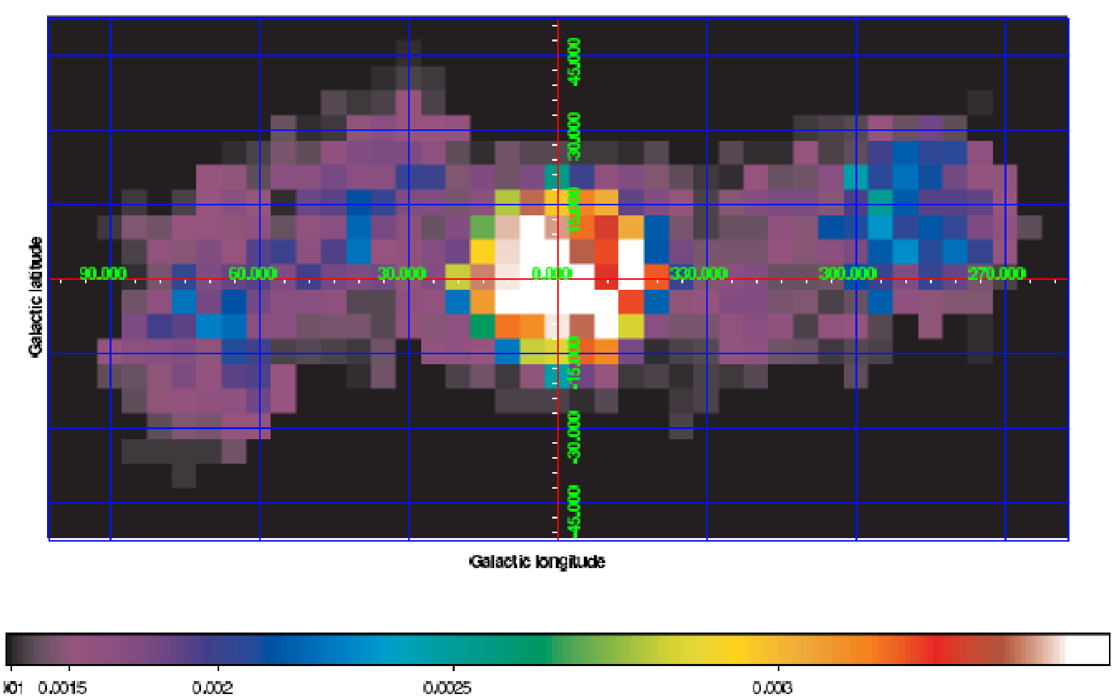

Figure 1.7: Intensity map of center of the 511 keV sky of INTEGRAL/SPI data. Scale is photons cm^{-2} s^{-1}. Lines of latitude (longitude) are spaced 15° (30°) apart. (Figure from [38].)

the bulge-to-disk ratio[9] $B/D > 1.4$. This is perhaps the most intriguing element of the 511 keV line since, as we shall see in Section 1.2.3, no known astrophysical sources can reproduce such a distribution.

Many authors have produced empirical fits to the SPI data, the most accurate being by Weidenspointner *et al.* [39]. After repeating their fitting procedure with more recent data, this became the benchmark comparison model for our own fitting procedure. They fit the signal with two 2D concentric gaussians, with FWHM = $3°$ and $11°$, respectively, in addition to a disk component modeled by a young stellar disk. This type of fit is informative but of limited utility, since it does not propose a physical origin for the positrons.

It is worth examining known astrophysical sources of positrons, to see if any combination thereof can explain the INTEGRAL/SPI intensity, spectrum and morphology around 511 keV. As will be shown, this is a difficult order in spite of the plethora of different positron sources in the Milky Way.

1.2.3 Positron sources in the Milky Way

Radioactivity

The most obvious place to look for low-energy positrons is in processes involving radioactive beta decay. β^+ particles are positrons that are naturally produced with energies at the MeV scale. Synthesis of radioisotopes is known to occur in stars, supernovae and novae.

The most well-known contributor is ^{26}Al, which is produced both during H-burning in massive stars and explosively in supernovae. ^{26}Al has a lifetime of 740 000 years, which means that it can easily escape its progenitor before injecting positrons into the ISM. It also produces an excited ^{26}Mg nucleus, which emits a gamma-ray photon

[9] This is the ratio of fluxes: $B/D = \Phi_{\rm bulge}/\Phi_{\rm disk}$.

at 1809 keV upon de-exitation:

$$
\begin{aligned}
{}^{26}\mathrm{Al} &\rightarrow \beta^+ +^{26} \mathrm{Mg}*, \\
{}^{26}\mathrm{Mg}* &\rightarrow^{26} \mathrm{Mg} + \gamma.
\end{aligned}
\tag{1.11}
$$

The 1809 keV line has been observed by CGRO/OSSE and more recently by INTEGRAL/SPI. Diehl *et al.* [40] fit the INTEGRAL/SPI data to a young stellar disk distribution, which is consistent with a massive star/supernova origin. Since a β decay of ^{26}Al gives one 1809 keV photon and one positron, it points to an unambiguous source of 511 keV radiation that must be included in any model.

Other radioactive isotopes are known to be produced in the galaxy [41], but their abundances and distribution are much more uncertain. ^{44}Ti is expected to be produced in the inner layers of supernovae. Due to a shorter lifetime (59 years) and more uncertainty in the production mechanism, the amount of ^{44}Ti injected into the ISM is not well constrained. Type Ia supernovae also produce ^{56}Ni, which eventually decays to ^{56}Fe $+\beta^+$ over 83 days. The most contentious issue regarding this channel is the amount of ^{56}Ni or ^{56}Co that is ejected before decaying. If the decay occurs before ejection, it is quite unlikely that the decay products escape into the ISM before annihilating. Hypernovae and gamma-ray bursts are similarly expected to produce ^{56}Ni, but the rates are not known.

A final source of radioactive elements are novae, which consist of a binary system in which a dense object such as a white dwarf accretes matter from its companion, resulting in hydrogen burning on the surface. Novae are known to produce radioactive isotopes ^{13}N and ^{18}F, but their half-lives are too short to allow decay products to escape into the ISM. They also produce ^{22}Na, which produces β^+ particles over 2.6 years. However, production rates are two orders of magnitude lower than the INTEGRAL/SPI observations require [41].

The main issue surrounding a β^+ decay origin of the 511 keV signal concerns its morphology: all of the sources mentioned above should have a distribution that is correlated with the stars in the galaxy and predict a ratio $B/D < 0.5$. While these isotopes (especially ^{26}Al) certainly contribute to the disk signal, the bulge component remains unexplained.

High-energy processes

A second place to look for the production of positrons is in high-energy processes such as proton collisions with other nucleons, or gamma-gamma processes in hot dense media. The collision of cosmic ray protons with each other and with other elements can produce positively-charged mesons, which decay preferentially to muons, then to positrons. The typical energies of the decay products will be on the order of 30-40 MeV, however — much too large for our purposes.

Microquasars and X-ray binaries (XRBs) are expected to eject positrons. In fact, 100 or so such objects could produce enough positrons to account for the INTEGRAL/SPI observations. In a 2008 analysis, Weidenspointner et al. [42] correlated an asymmetry in the reconstructed SPI skymap with the distribution of Low-mass X-ray binaries (LMXRBs) in the Milky Way (Figure 1.8). However, the latter study used an incomplete catalog of sources and it is not clear if the full distribution even reproduces this asymmetry [43]. Complicated diffusion mechanisms must still be invoked if they are to explain a bulge of positrons around the GC. More recent analyses [44] combining OSSE and SPI data suggest that the apparent asymmetry is really an offset of the 511 keV central component with respect to the galactic center by $1° - 2°$.

Pulsars can also act as positron sources. These objects are rapidly rotating magnetized neutron stars, resulting from a previous supernova explosion. This rotation induces strong electric fields which can extract electrons from the surface, creating a hot dense plasma field known as the magnetosphere. The photons emitted by synchrotron radiation as these electrons travel along the field lines can be so energetic that $e^{\pm}$ pair-production from γ-γ collisions, or from the γ-$\mathbf{B}$-field interaction is possible [45]. When this relativistic "wind" of particles hits the surrounding ejecta from the pulsar's projenitor, a shock occurs, slowing down the wind and creating a relativistic magnetized fluid known as a pulsar wind nebula (PWN). This shock accelerates electron-positron pairs, which can be seen directly through radio, X-ray and gamma-ray observations of synchrotron and inverse-Comption scattering. In addition to having very large energies, it is unclear what proportion of positrons manage to escape the PWN.

Finally, p-p and γ-γ processes are expected to produce $e^{\pm}$ pairs in the supermassive black hole (SMBH) at the GC. While this scenario has the advantage of producing positrons that could at least be distributed in a spherically symmetric manner, propagation mechanisms must be invoked to transport the positrons 1 to 2 kpc away from the GC, and then slow them down enough to avoid overproduction of > MeV photons in the gamma-ray spectrum.

Table 1.1 summarizes the known astrophysical sources of e^+ in the galaxy. Checkmarks indicate whether the criteria of intensity, spectrum and morphology can be adequately explained. None of the rows contain three checkmarks, which is overwhelmingly due to a single factor: morphology. With the possible exception of the SMBH, no known source reproduces a B/D greater than 0.5 — far from the required $B/D > 1.4$.

Source	Intensity	Spectrum	Morphology
Massive stars (^{26}Al)	✓	✓	×
SNe (^{44}Ti)	✓	✓	×
SNIa (^{56}Ni)	× (?)	✓	×
Novae	×	✓	×
Hypernovae/GRBs (^{56}Ni)	?	✓	×
Cosmic ray $p - p$	?	×	×
LMXRBs	✓	✓	×
Microquasars	✓	✓	×
Pulsars $\gamma - \gamma$	✓	×	×
Central black hole	?	×	✓(?)

Table 1.1: Summary of possible positron sources in the galaxy (Table adapted from [41]).

1.2.4 Dark Matter to the rescue

The near-spherical shape of the dark matter halo therefore seems perfectly tailored to this problem. Indeed, many authors have considered a dark matter source of

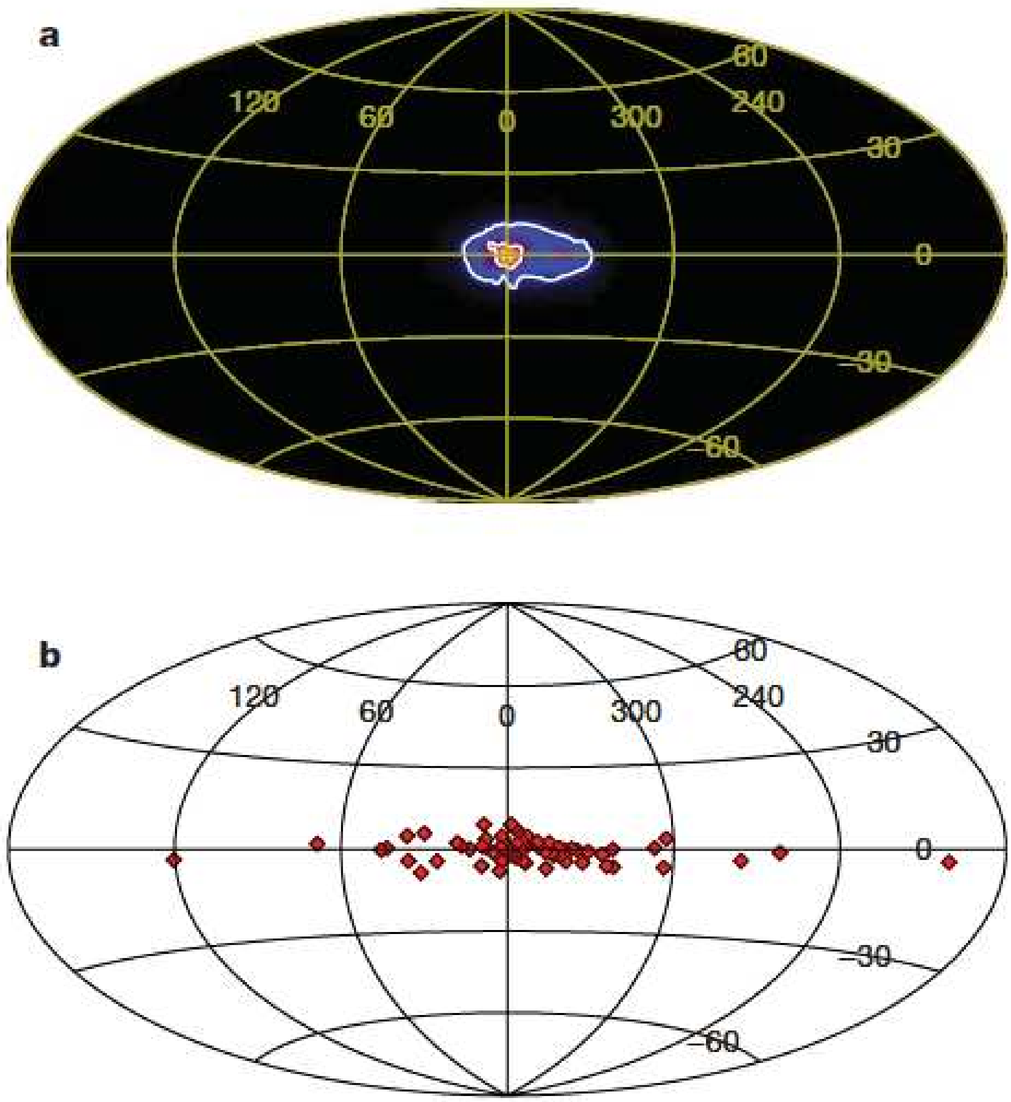

Figure 1.8: The asymmetry a) resulting from the analysis of [42] of the 2007 INTEGRAL/SPI 511 keV data could have been explained by b) the distribution low-mass X-ray binaries (LMXRBs). This map is incomplete, however, and does not include 511 keV sources that are obscured in the X-ray band. This scenario is thus disfavoured by more recent analyses, although a certain asymmetry may indeed be present in the 511 keV signal (Figure from [42]).

positrons to explain the INTEGRAL/SPI excess. References [46, 47, 48, 49, 50, 51, 52, 53] constitute an incomplete list.

The generation of $e^{\pm}$ pairs from dark matter is conceptually simple. The decay or annihilation of dark matter can generate some intermediate gauge boson, which may act as a force mediator in the dark sector. If this boson has some non-zero mixing term with the standard model photon in the Lagrangian $\mathcal{L}$ such as:

$$\mathcal{L} \ni \epsilon F_{\mu\nu} B^{\mu\nu}, \tag{1.12}$$

where $B^{\mu\nu}$ and $F_{\mu\nu}$ are the dark boson and photon field strengths, respectively, then the processes illustrated in Figure 1.9 (a) may occur. A portal to the standard model could also be present in the form of a massive scalar mediator ϕ — for instance a dark Higgs boson — which would couple to the fermions via Yukawa interactions.

In order to obtain the correct spectrum, the DM mass may not be much larger than a few MeV. To circumvent this awkward constraint, [47] proposed a model of excited dark matter (XDM). If the dark matter has two (or more) distinct energy states χ and $\chi*$, then the spectral measurements of Figure 1.6 only constrain the mass difference $\delta = m_{\chi*} - m_{\chi}$. Depending on the lifetime of the metastable state, XDM deexitation can look to an observer like dark matter decay (left-hand side of Figure 1.9 (b)) or annihilation (right-hand side). This leaves the mass free again, allowing the same model of DM to also explain direct detection results ($m_{\chi} \sim 10$ GeV), or the high-energy anomalies that will be the focus of Chapters 3 and 4.

Whereas other authors have provided fits to reconstructions of the SPI data, our goal in Chapter 2 was to directly compare the predictions of an XDM model with the INTEGRAL/SPI data in a statistically meaningful way. Our conclusions are rather striking. By using an Einasto profile with parameters determined by the *Via Lactea II* simulation, chosen because it was specifically engineered to simulate a Milky Way-sized halo, we show that the INTEGRAL/SPI 511 keV morphology can be fit by scattering XDM. The significance of this fit is just as good as previous empirical fits that did not suggest a physical production mechanism, and we require only two degrees of freedom rather than the 8 of these previous studies.

1.3 Positron anomalies: high energy

Chapters 3 and 4 concern a second positron cosmic ray anomaly, which corresponds to an unexpectedly high flux of positrons in the 10-1000 GeV region. Given the high energies involved, this particular anomaly has only been quantified relatively recently. A certain amount of high-energy antimatter is expected to exist, with fluxes that fall off as a power law of energy. These are mainly generated as secondary particles from the collision of cosmic ray protons with each other and with heavier species.

Observations by the PPB-BETS[10] [54] and then the ATIC[11] [55] balloon experiments, published in 2008, pointed to an unexpected increase in the total flux of $e^+ + e^-$ compared with predictions around 10 GeV. Simultaneously, the PAMELA[12] [56] sattelite observed an unexpected rise in the positron fraction:

$$\frac{\Phi_{e^+}}{\Phi_{e^+} + \Phi_{e^-}} \tag{1.13}$$

from 10 GeV to the end of its observational range at 100 GeV. The first year of $e^+ + e^-$ data from the Fermi telescope [57] confirmed an excess above predicted backgrounds, although it was a less pronounced peak than the balloon-borne experiments observed. In 2011 the Fermi-LAT collaboration confirmed the PAMELA observation [58], extending the rising positron fraction observation beyond 200 GeV. These results are presented in Figure 1.10.

Dark matter interpretations of the electron/positron excess have been proposed since the ATIC peak was first seen [60, 49, 61, 62, 63, 64, 65, 66, 67, 68]. A DM particle with a $\sim$ TeV mass can produce high energy leptons through decay or annihilation

[10] Polar Patrol Balloon — Balloon-borne Electron Telescope with Scintillating fibers

[11] Advanced Thin Ionization Calorimeter

[12] Payload for Antimatter Matter Exploration and Light-nuclei Astrophysics

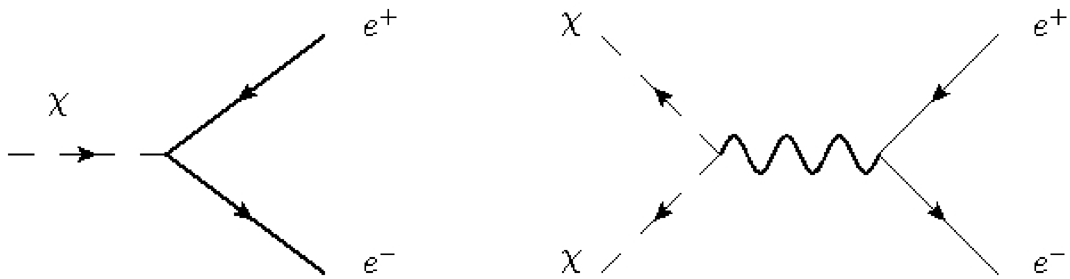

(a) Decaying/annihilating DM

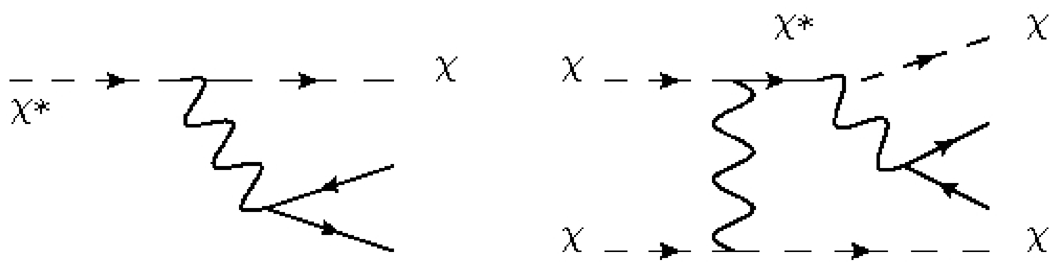

(b) Excited DM

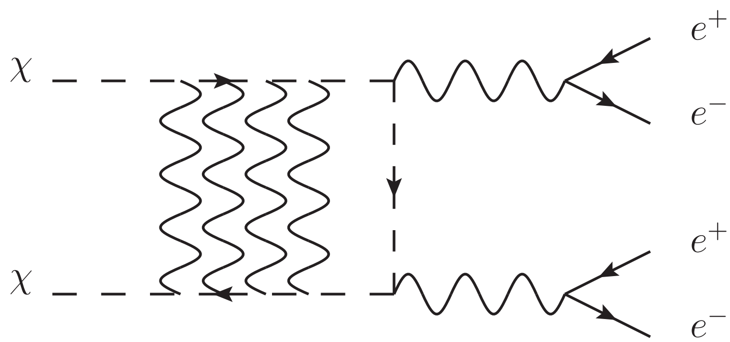

(c) Sommerfeld enhanced DM

Figure 1.9: Different ways of producing positrons from dark matter. (a) decay or annihilation to low- or high-energy standard model particles. (b) excited dark matter (XDM) emission of a low-energy $e^{\pm}$ pair. (c) Sommerfeld-enhanced collision resulting in two $e^{\pm}$ pairs, giving a smooth fit to the Fermi $e^{+} + e^{-}$ spectrum. In every case the intermediate gauge boson can kinetically mix with the SM photon, which allows production of standard model particles.

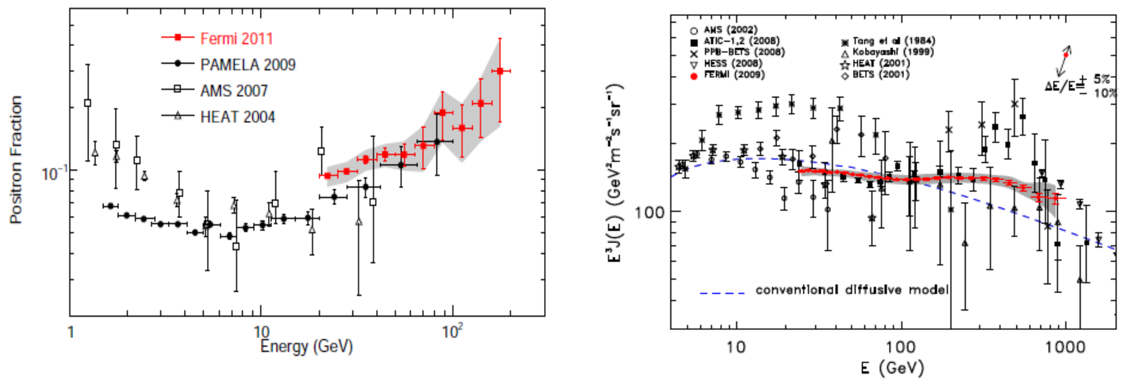

Figure 1.10: Left: the positron fraction $e^+/(e^+ + e^-)$ as a function of energy, as observed by PAMELA and subsequently confirmed in 2011 by Fermi. An example cosmic ray background can be seen for example in Figure 3.5. Image from Fermi [58]. Right: the spectrum of electrons + positrons observed by the Fermi-LAT. Image from Fermi [59].

into one or two $e^\pm$ (or $\mu^\pm$ pairs (Figure 1.9 (a) or (c)). The most recent spectral data from Fermi and PAMELA favours the annihilation scenario $\chi\chi \rightarrow 4e$ due to its softer spectrum than the $2e$ final state. This is possible provided that:

- The DM is "leptophilic", *i.e.* it annihilates primarily to $e^\pm$ or $\mu^\pm$ pairs. This is necessary since PAMELA and other experiments have not observed a corresponding excess in antiprotons. The simplest way to ensure this is to constrain the mass of the intermediate gauge boson to $m_B < 2m_p$.
- Some mechanism exists to enhance the annihilation cross-section $\langle\sigma v\rangle_{\rm ann}$. As our results will show, the cross-section necessary to reproduce the PAMELA excess is two to three orders of magnitude larger than the relic abundance cross-section. An attractive force, such as a Sommerfeld enhancement $\propto 1/v_{\rm rel}$, can provide this boost without strongly affecting the thermal freeze-out of dark matter.

The term "Sommerfeld enhancement" does not refer to any exotic phenomenon: it is simply the effect of an attractive (or repulsive) force on scattering at low velocities. Since it is central to many annihilating dark matter models and has been the source of some misunderstanding between the particle and astronomy communities, it is worth a brief review before continuing.

Sommerfeld Enhancement

Sommerfeld enhancement is a non-perturbative effect[13] that is easiest understood by looking at the reduced Schrödinger equation for two scattering χ particles [49]:

$$-1\frac{1}{2\mu}\nabla^2\psi_k + V(r)\psi_k = \frac{k^2}{2m_\mu} \tag{1.14}$$

with the usual asymptotic condition as $r \to \infty$:

$$\psi \to e^{ikz} + f(\theta)\frac{e^{ikr}}{r}. \tag{1.15}$$

ψ is the two-particle wavefunction, k is the relative momentum, $\mu = m_\chi/2$ is the reduced mass of the system and r is the inter-particle separation. We assume annihilation has occurred when the two particles hit each other, *i.e.* when $r = 0$. This means that the annihilation cross-section σ_{ann} will be proportional to $\psi_k(0)$. The enhancement, or boost factor, is then the ratio of the annihilation rate *with* an attractive potential to the rate *without*:

$$S \equiv \left|\frac{\psi_k(0)}{\psi_k^0(0)}\right|^2, \tag{1.16}$$

where ψ_k^0 is the solution to (1.14) in the case $V(r) = 0$. (1.14) is rotationally invariant, so it is separable into angular and radial components:

$$\psi_k = \sum_l c_l P_l(\cos\theta) R_{kl}(r), \tag{1.17}$$

with the Legendre polynomials P_l. The radial equation can thus be written:

$$-\frac{1}{m_\chi}\frac{1}{r^2}\frac{\mathrm{d}}{\mathrm{d}r}\left(r^2\frac{\mathrm{d}}{\mathrm{d}r}R_{kl}\right) + \left(\frac{l(l+1)}{r^2} + V(r)\right)R_{kl} = \frac{k^2}{m_\chi}R_{kl}. \tag{1.18}$$

[13] It can also be viewed as a resonant exchange of gauge bosons in the "ladder" diagram of Figure 1.9 (c).

If $V(r)$ vanishes quickly enough at infinity, the asymptotic solution is:

$$R_{kl}(r) \to \frac{1}{r}\sin\left(kr - \frac{1}{2}l\pi + \delta_l(r)\right). \tag{1.19}$$

We are only interested in the $l = 0$ component, since only R_{k0} is nonzero at $r = 0$. The non-interacting wavefunction R^0_{k0} can be found by observing that the plane wave is composed of states with all angular momenta:

$$e^{ikz} = e^{ikr\cos\theta} = \sum_l i^l(2l+1)j_l(kr)P_l(\cos\theta). \tag{1.20}$$

The 0^{th} spherical Neumann function is $j_0(\rho) \equiv \sin(\rho)/\rho$. This allows us to rewrite (1.16):

$$S \equiv \left|\frac{R_{k0}(0)}{k}\right|^2. \tag{1.21}$$

$R_{k0}(r)$ turns out to be analytically expressible only for a limited number of potentials $V(r)$. For example, the Coulomb case $V = -\alpha/r$ can be solved with hypergeometric functions [49], yielding the enhancement:

$$S_{\text{Coulomb}} = \frac{\alpha\pi/v}{1 - e^{-\alpha\pi/v}}, \tag{1.22}$$

where v is the relative velocity. The rough proportionality with $1/v$ is important: it means that a collection of interacting particles can have very different annihilation cross-sections depending on their temperature: annihilation in the hot early universe can be suppressed relative to the rates today.

We are however interested in the exchange of a *massive* force carrier ϕ, with mass m_ϕ. In this case the potential takes the Yukawa form:

$$V(r) = -\frac{\alpha}{r}e^{-m_\phi r}, \tag{1.23}$$

and (1.14) must be solved numerically. It may be recast into the form [69]:

$$\frac{\mathrm{d}^2\zeta_k}{\mathrm{d}x^2} = -\left(\frac{f\alpha}{x}e^{-x} + \left(\frac{v}{f}\right)^2\right)\zeta_k, \tag{1.24}$$

with $f = m_\phi/m_\chi$, $x = m_\phi r$ and $\zeta_k = rR_{k0}$. Since $R_{k0}(0) \to$const., we must have $\zeta_k(0) = 0$. The second boundary condition is the properly normalized asymptotic form[14] :

$$\zeta_k(x \to \infty) \to \sin\left(\frac{v}{f}x + \delta\right). \tag{1.25}$$

The numerical solution for a set of parameters α, f is illustrated in Figure 1.11. The $1/v$ enhancement still exists, but there are two additional elements: 1) the finite range of the Yukawa interaction imposes a saturation to the enhancement; and 2) the crest-like features that correspond to resonances where $S \propto 1/v^2$. These occur because of the presence of zero-energy bound states, which allow efficient capture at low relative velocity. These resonant enhancements thus provide an elegant mechansim to obtain large cross-sections at late times.

We may now turn to the propagation of cosmic rays from their point of origin to detectors such as PAMELA and Fermi.

1.3.1 Cosmic Ray Propagation

While many open questions remain, especially concerning the highest energy cosmic rays (CRs), their origin below the knee at 10^{15} eV is mainly understood to be from acceleration by the supernova remnants (SNRs) of the Milky Way. This "shock" acceleration can be directly measured by observing synchrotron and high-energy processes in the SNRs [70]. These objects are mainly confined to the plane of the galaxy, and models give a power law spectrum of protons and other primary particles that is consistent with observations.

At such high energies where $p \gg m$, understanding the propagation of cosmic rays CRs is as important as understanding their source. A large fraction of the CR electrons, and nearly all of the CR antiparticles, are created as secondary particles during the propagation of primaries in the ISM. Meanwhile, the spectrum and flux of

[14] This can be alternatively seen as an initial value problem $\tilde{\zeta}(0) = 0$; $\tilde{\zeta}'(0) = 1$, with $\zeta \equiv \tilde{\zeta}/A$, where A is the asymptotic amplitude of $\tilde{\zeta}$. This is more suitable to numerical solution.

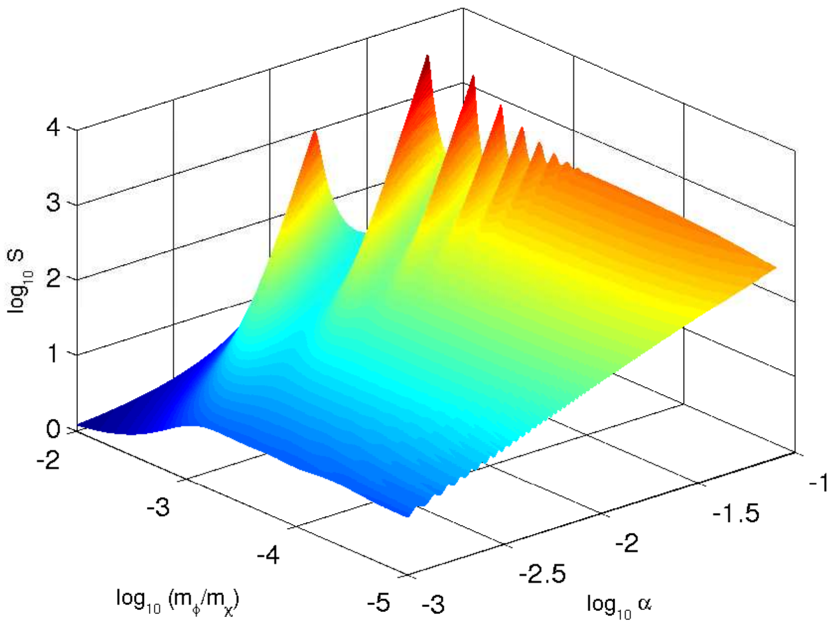

(a)

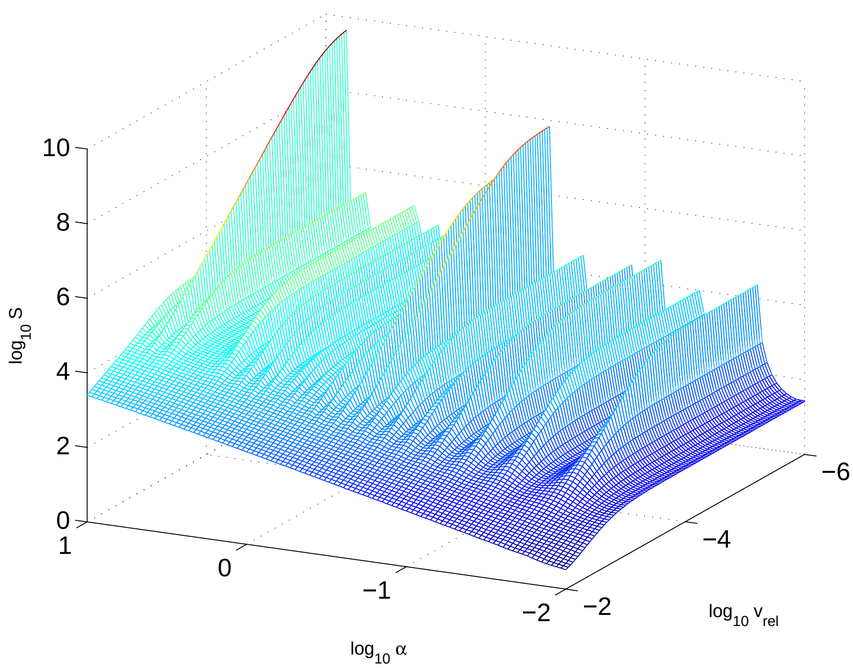

(b)

Figure 1.11: Sommerfeld enhancement due to a Yukawa interaction potential (1.23) as a function of the coupling α, ratio of masses $f = m_\phi/m_\chi$ and relative velocities v_{rel}. (a): for varying $f = m_\phi/m_\chi$ at fixed v =150 km/s. (b): for varying relative velocities, $f = 0.003$.

all CR species depend on their diffusion in the ISM. Interaction with other species, with the galactic magnetic field and with the interstellar radiation field (ISRF) must all be accounted for. These effects are parametrized as a diffusion equation for the density per unit momentum $\psi_i(\vec{x}, p, t)$ of each species i [71]:

$$\frac{\partial \psi_i}{\partial t} = q(\vec{x}, p) + \nabla \cdot \left(D_{xx} \nabla \psi_i - \vec{V}_c \psi_i \right) + \frac{\partial}{\partial p} p^2 D_{pp} \frac{\partial}{\partial p} \psi_i - \frac{\partial}{\partial p} \left(\dot{p} \psi_i - \frac{p}{3} (\nabla \cdot \vec{V}_c) \psi_i \right) - \frac{1}{\tau_f} \psi_i - \frac{1}{\tau_r} \psi_i. \tag{1.26}$$

From left to right: $q(\vec{x}, p)$ is the source, or injection term, D_{xx} describes diffusion in real space, D_{pp} parametrizes reacceleration, $\dot{p}$ describes energy loss, $\vec{V}_c$ is the convection velocity, $1/\tau_f$ is the fragmentation rate, and $1/\tau_r$ is the radioactive decay rate. Spatial diffusion for a species with charge Z and speed β is parametrized as:

$$D_{xx} = \beta D_{0xx} \left(\frac{R}{R_0} \right)^{\delta}. \tag{1.27}$$

R is the rigidity p/Z and D_{0xx} is the diffusion coefficient at some reference rigidity R_0. D_{0xx} and δ can be determined by comparing the solutions of (1.26) to measurements of CR data.

Computing the distribution of CR species today is therefore a matter of solving for the steady state of the diffusion equation: $\dot{\psi}(\vec{x}, t) = 0$. In the case of electrons and positrons, equation (1.26) is simplified due to the absence of spallation or decay. Reacceleration and convection are furthermore subdominant to diffusion and energy loss, which is due to interaction with photons via synchrotron radiation and inverse-Compton scattering. The energy loss rate $\dot{p}$ can be parametrized as:

$$b(\vec{x}, E) \equiv -\frac{\mathrm{d}E_e}{\mathrm{d}t} = \frac{32\pi\alpha_{em}^2}{3m_e^4} E_e^2 \left[u_B + u_\gamma R(E_e) \right] \tag{1.28}$$

where u_B is the energy density of the interstellar magnetic field, and u_γ is the energy density of the ISRF, which contains three distinct components:

- The cosmic microwave background, which is uniformly distributed in the galaxy,
- Starlight, which peaks near the GC and is centred in the visible region of the spectrum and

- Thermal radiation from dust, which peaks in the infra-red.

These energy distributions are illustrated in Figure 1.12 and their spatial distributions can be found in Figure 4.1. The factor $R(E_e)$ encodes the relativistic corrections to the Thompson scattering formula, and is also illustrated in Figure 1.12.

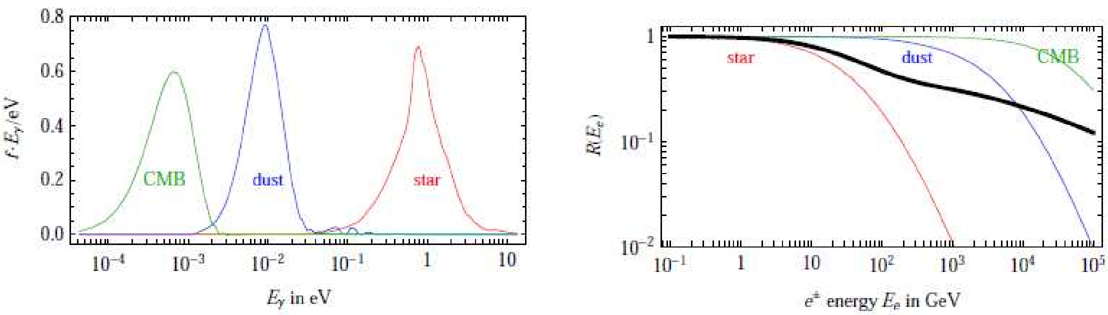

Figure 1.12: Left: the spectrum of each component of the interstellar radiation field (ISRF). Right: the factor $R(E_e)$ in equation (1.28) for each ISRF component. Both figures from [64].

The source term $q(\vec{x}, p)$ is composed of secondary sources, such as spallation products, as well as the primary sources of $e^\pm$ injected into the ISM: stars, supernovae, and the annihilating dark matter that is of particular interest to us. If the source is the collision of dark matter (for example Figure 1.9 (a)), then the source term takes the form:

$$q_{\chi\chi\to e^+e^-} = \frac{1}{2}\left(\frac{\rho_\chi(\vec{x})}{m_\chi}\right)^2 \langle\sigma v\rangle_{\rm ann}\frac{\mathrm{d}N_{e^\pm}}{\mathrm{d}E}. \tag{1.29}$$

If the gauge boson mass is small enough that electrons are the only annihilation products, the injection spectrum can be approximated as:

$$\frac{\mathrm{d}N_{e^\pm}}{\mathrm{d}E} = \frac{1}{m_\chi}\delta(m_\chi - E), \tag{1.30}$$

for the two-lepton final state, and

$$\frac{\mathrm{d}N_{e^\pm}}{\mathrm{d}E} = \frac{2}{m_\chi}\Theta(m_\chi - E), \tag{1.31}$$

for the 4-lepton final state, where $\Theta(x)$ is the Heaviside step function. We will see that due to the smoothness of the latter function, this is the favoured channel to fit the PAMELA and Fermi data. As the intermediate gauge boson's mass is increased, the spectrum of each daughter species becomes more difficult to compute. Such an analysis using Monte Carlo techniques was done by [72].

Equation (1.26) can be solved semi-analytically, using Green's function methods, or fully numerically. By discretizing the propagation equation, codes such as the publicly available GALPROP [73] and DRAGON [74] can solve the steady-state (1.26) via a Crank-Nicholson method on a cylindrical grid in two (assuming angular symmetry) or three dimensions. The advantages of the numerical approach include greater control over the space- and energy-dependence of the propagation parameters such as the ISRF distribution and the galactic magnetic field, as well as a complete computation of the secondary particle production. Diffusion parameters, as well as the size of the diffusion zone,[15] are tightly constrained by observations of secondary/primary ratios such as the boron to carbon ratio as well as the ratios between different Fe isotopes. This means that one cannot consistently "tune" the parameters to obtain the correct fit without accounting for heavier species.

We will make substantial use of the GALPROP code in Chapters 3 and 4, since we will need to solve for 1) the background electron and positron spectrum and 2) diffusion of $e^{\pm}$ over very large distances, through a varying ISRF.

Primaries vs. secondaries

Since its earliest measurements, the spectrum of cosmic ray protons has been known to fall as a single power law $\sim E_p^{-3}$. If the majority of cosmic ray electrons and positrons were produced as secondary particles, their spectrum should fall off at least as fast as the CR proton spectrum.[16]

The sharp rise in the positron fraction and the softening of the falloff of the $e^{\pm}$ spectrum therefore point us to a primary source of positrons — and most likely,

[15] Particles that hit the boundary are assumed to escape the Galaxy.

[16] Actually, it should be much faster, given that the efficiency of energy-loss from ICS scales inversely with mass.

electrons — with an injection energy $\sim$ TeV in the Galaxy. Using standard parameters $D_{0xx} = 0.19$ kpc^2/Myr, $\delta = 0.41$ and an energy loss rate[17] of $\tau_e = 10^{16}$ s GeV [75], we can estimate the characteristic propagation distance Δx of a TeV electron:

$$(\Delta x)^2 \sim \left(\frac{E}{4\text{GeV}}\right)^{\delta} D_{0xx}\frac{\tau}{2E} \sim (0.5 \text{ kpc})^2. \tag{1.32}$$

The obvious — and commonly-held — interpretation is that the observed flux of $e^\pm$ should be produced within a kpc of our position. However, we shall see that if a sufficiently large source of $e^\pm$ exists many kpc away, *e.g.,* in the form of DM subhalos outside the diffusion zone, it is possible for the flux at earth to be large enough to explain the PAMELA signal without violating other constraints.

1.3.2 Gamma Rays

It is possible to constrain the distribution of high-energy electrons and positrons far away from the Earth's location in the Galaxy by looking for by-products of their interactions with the ISM. The energy lost (1.28) to the B-field is visible as radio-frequency synchrotron radiation, whereas ICS losses appear as gamma-ray photons in the $\gtrsim 10$ GeV range. The production of high-energy electrons is also accompanied by large fluxes of final-state radiation (FSR), also known as internal bremsstrahlung. A detailed presentation of the FSR spectrum is given in Section 4.3.

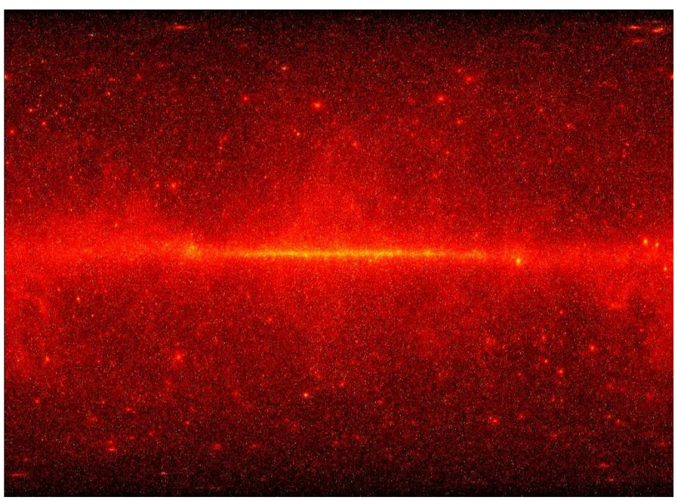

Figure 1.13: Projection of the full diffuse gamma ray sky, reconstructed from the first year of Fermi-LAT data.

[17] this is just the right-hand side of (1.28), evaluated locally, divided by E_e^2.

Since the ISM is mainly transparent to gamma-rays, they are an ideal probe of the distribution of TeV electrons in the inner Milky Way. The Fermi-LAT has mapped the high-energy gamma ray sky to an unprecedented accuracy since its launch in 2008, and the diffuse gamma ray data are publicly available [77].

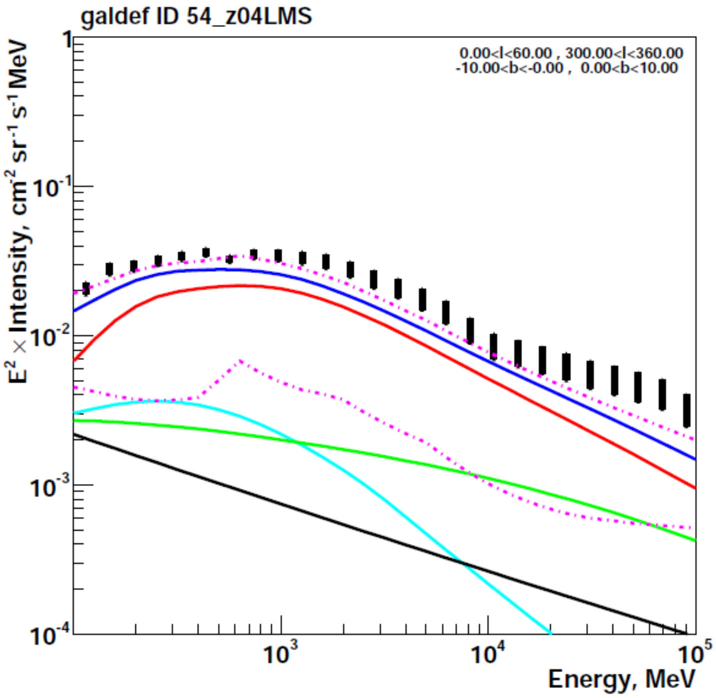

Figure 1.14: The gamma-ray spectrum in the range $-60° < \ell < 60°, -30° < b < 30°$ and simulated contributions. Red: pion decay; green: inverse Compton; black: isotropic component; blue: total, without sources; magenta: point sources, and total with sources. Figure from [76].

The gamma ray spectrum at a given latitude b and longitude ℓ in the sky can be computed with line-of-sight integrals, in analogy with the procedure used for the 511 keV flux, although an extra factor $\mathrm{d}N_\gamma/\,\mathrm{d}E$ must account for the spectral shape. In the case of annihilating dark matter, this takes the form (4.16) or (4.10,4.12) for ICS and FSR contributions, respectively.

Cosmic ray models may then be directly compared with gamma-ray data. Using the output from propagation codes such as GALPROP, the gamma-ray flux can be approximately modeled. An example from [76] is presented in Figure 1.14. Background sources include: final-state photons from pion decay, inverse-Compton scattering (ICS) products of secondary electrons and positrons, point sources such as stars, pulsars and supernova remnants, as well as an isotropic "extra-galactic" contribution.

Since the normalization of some of these components depends on the fitting procedure itself, it is more useful to use the gamma ray data as an upper bound: if the predicted gamma ray flux from known sources[18] exceeds the measured fluxes at a certain confidence level at any location in the sky, the model can be considered ruled out.

The most constraining region in the sky for dark matter models is in fact the galactic center (GC). Although the GR fluxes are largest at the GC, this is also the region where DM production is expected to be highest, due to 1) the cuspy center of the dark matter halo; and 2) the low dispersion velocities, which tend to boost annihilation in Sommmerfeld-enhanced models.

1.3.3 Astrophysical sources of primary positrons

Speculation on the nature of the PAMELA excess has been rife since its first observation. In fact, the high-energy processes outlined in Section 1.2.3 appear as perfect candidate sources for this new anomaly.[19]

As mentioned in Section 1.2.3, the large fields and hot dense plasmas of pulsars and pulsar wind nebulae are perfect environments for the creation of $e^{\pm}$ pairs at high energies. Many studies (see *e.g.,* [78, 79, 80, 81]) have considered this scenario and it is arguably the favoured contender among standard astrophysical proposals. While a pulsar origin by itself is unlikely, the pulsar + PWN scenario appears able to provide enough very high-energy positrons to explain the PAMELA excess, given the known distribution of pulsars in the Galaxy. If this is the case, the spectrum is expected to be

[18] This includes the background particles with non-DM origins.

[19] A notable exception is the Sgr A* black hole: this can be easily discounted, though. The inverse-Compton gamma-ray flux expected from a point source of positrons diffusing to our position would be much larger than what is expected — and already ruled out — from a diffuse dark matter halo.

dominated by a few nearby objects[20] [79]. These should give rise to additional spectral features at high energies associated with the individual pulsars. These conclusions are based on assumptions about the fraction of positrons which manage to escape the nebulae, which is still not well understood [45].

Supernova remnants (SNRs) are also a prime candidate, since SNR shocks are already thought to produce and accelerate the heavier cosmic ray species. It has been proposed [83] that positrons (and electrons) produced as secondaries *inside* in the shock region of an SNR are subject to the same acceleration as other CR species, leading to an increase in the positron fraction with energy. This was shown to give a flatter spectrum than secondary production in the ISM, and can ostensibly give the proper spectral shape after diffusion in the Galaxy. This calculation does not include nonlinear effects such as turbulence, or phenomena that would limit the escape of positrons.

Jets from X-ray binaries, gamma ray bursts, CR interaction with dense gas clouds and magnetars form an incomplete list of possible nearby objects that may produce high-energy positrons, although they are on less firm theoretical footing than pulsars or SNRs.

Finally, it has been suggested that the misidentification of even a small number of protons as positrons could be responsible for the rise seen the PAMELA data [84]. With the recent Fermi positron fraction data, this hypothesis can be be discounted.

1.3.4 Subhalos in the Milky Way

As mentioned at the beginning of Section 1.3, dark matter origin has been the focus of a large number of studies since the high-energy positron anomaly was first observed. These models were found to be highly constrained by the ICS and final-state radiation associated with large $e^{\pm}$-pair production near the galactic center, even for less cuspy isothermal dark matter profiles. These constraints are explicitly calculated

[20] It is even possible that a *single* nearby pulsar such as Geminga can be responsible for the entire flux [82].

in Chapter 4. At the same time, substructure has been searched for gamma ray signals of annihilating DM [85, 86, 87, 88, 4, 67]. A few studies have examined the effects of nearby substructure ([89, 90] and, more recently [91]); our aim in Chapters 3 and 4 was to determine the impact of the complete set of substructure. In Chapter 3 we show that an improved fit to the PAMELA and Fermi data can be obtained by including the contribution of the several thousand subhalos predicted by *Via Lactea II*. Furthermore, the results presented in Chapter 4 demonstrate that although this results in a reduced gamma-ray flux from the GC, it is not enough to overcome the stringent bounds from Fermi-LAT.

We will finally show that a nearby subhalo similar to the ones predicted by *Via Lactea II* could produce the correct positron fraction without violating gamma-ray and $e^{\pm}$ dipole anisotropy constraints if it is centred within a few hundred parsecs of the Sun.

Chapter 2

Interacting dark matter contribution to the Galactic 511 keV gamma ray emission: constraining the morphology with INTEGRAL/SPI observations

Work published with Pierrick Martin and James M. Cline
in JCAP 1204 (2012) 022

Abstract

We compare the full-sky morphology of the 511 keV gamma ray excess measured by the INTEGRAL/SPI experiment to predictions of models based on dark matter (DM) scatterings that produce low-energy positrons: either MeV-scale DM that annihilates directly into e^+e^- pairs, or heavy DM that inelastically scatters into an excited state (XDM) followed by decay into e^+e^- and the ground state. By direct comparison to the data, we find that such explanations are consistent with dark matter halo profiles predicted by numerical many-body simulations for a Milky Way-like galaxy. Our results favour an Einasto profile over the cuspier NFW distribution and exclude decaying dark matter scenarios whose predicted spatial distribution is too broad. We obtain a good fit to the shape of the signal using six fewer degrees of freedom than

previous empirical fits to the 511 keV data. We find that the ratio of flux at Earth from the galactic bulge to that of the disk is between 1.9 and 2.4, taking into account that 73% of the disk contribution may be attributed to the beta decay of radioactive ^{26}Al.

2.1 Introduction

The 511 keV gamma ray line observed by the INTEGRAL/SPI experiment is consistent with the annihilation of $\sim (1.5 \pm 0.1) \times 10^{43}$ low-energy positrons per second in a region within $\sim$ 1 kpc of the galactic center (GC), in addition to a fainter ($(0.3 \pm 0.2) \times 10^{43}$ e^+ s^{-1}) disk-like component that extends along the galactic plane [37]. The line is mostly due to parapositronium annihilation of thermal or near-thermal positrons [92, 36]. The absence of γ rays from e^+ annihilations in flight implies that the positrons are injected with energies less than $\sim$ 3 MeV [93]. No astrophysical source has been proven to yield such positrons with the required concentrated and approximately axially symmetric spatial distribution.

Among conventional sources, radioactive ejecta from stars, supernovae and gamma-ray bursts can produce a large enough rate of positrons through β^+ decay, but their spatial distribution is not sufficiently confined toward the bulge: they predict a ratio of bulge to disk luminosities $B/D < 0.5$, whereas observations demand $B/D > 1.4$. Other proposed mechanisms also suffer from this problem. In addition, positrons from pair creation near pulsars or from *p*-*p* collisions associated with cosmic rays or the supermassive black hole tend to be too energetic. Low-mass X-ray binaries have received attention as a possible source, but these also do not give rise to large enough B/D [43]. A comprehensive review of these sources and the challenges they face is given in [41].

Dark matter (DM) interactions have the potential to explain the observed excess, either through direct annihilations of light ($\sim$ few MeV) DM particles into e^+e^- pairs [46], or by the excited dark matter (XDM) mechanism, in which excited states of heavy DM (χ) are produced in χ-χ collisions, with subsequent decay of the excited state into the ground state and an e^+e^- pair [47, 48]. The latter scenario has the theoretical advantage that the DM mass is relatively unconstrained, requiring only that the splitting between the ground and excited states be less than a few MeV.

XDM as an explanation for the INTEGRAL/SPI 511 keV excess came under greater scrutiny in recent years after it was proposed [49] that nonabelian DM models could naturally have small $\sim$ MeV mass splittings and simultaneously explain additional recent cosmic ray anomalies [56, 59] as well as hints of direct DM detection [94]. Ref. [50] found that it is not possible to get a large enough rate of positrons for 511 keV emission in the nonabelian models that require production of *two* e^+e^- pairs (one at each interaction vertex). However, the original model of [47] can give a large enough rate [53] since only one such pair need be produced, which is energetically easier. Moreover, variant models involving metastable DM that scatters through a smaller mass gap [51, 52] also give a large enough rate, and are largely free of threshold velocity issues.

The aforementioned studies focused primarily on matching the overall rate of positron production, either ignoring morphological constraints or estimating them in a rough way. Ref. [95] is the only rigorous analysis with respect to dark matter models, done at a time when relatively little data had yet been accumulated. More recently, ref. [96] carried out a study of DM predictions for the 511 keV angular profile, but comparing to a previous fit to the observed shape [97] rather than directly to the data.

Our purpose in the present work is to improve upon these earlier papers by testing the DM model shape predictions directly against the most recent INTEGRAL data. We will then examine how these DM models compare to the phenomenological models obtained in previous studies, such as [39, 38], where the 511 keV celestial signal is represented by analytical shape functions with several free parameters. As we will see, an interesting feature of the DM models is that their predictions depend on far fewer parameters and they can thus be a more attractive candidate if they are shown to provide as good a fit as the phenomenological parametrizations.

In the remainder of the chapter, we first present the known sources of positrons in the galaxy, before discussing our procedure for modeling the 511 keV sky in Sections

2.3 and 2.4. We give our main results, along with the details of our fitting procedure, in Section 2.5 and briefly discuss the implications of this study in Section 2.6.

2.2 Known backgrounds

In order to correctly model the possible contribution to the 511 keV signal from DM scattering, it is necessary to subtract from the data the contributions from known sources of low-energy positrons. They can be produced from β^+ decay of ^{26}Al expelled from massive stars, as well as from ^{44}Ti and ^{56}Ni produced in supernovae. These contributions should be correlated with the stars in the galaxy, thus contributing dominantly to the disk component of the observed signal.

The contribution of ^{26}Al can be more directly assessed than that of the other radio-isotopes. During ^{26}Al decay, the de-excitation of the resulting ^{26}Mg nucleus produces a gamma ray signal at an energy of 1809 keV whose magnitude and morphology has also been mapped by INTEGRAL/SPI [40]. Since each decay produces a positron and an 1809 keV photon, one can unambiguously determine the fraction of the 511 keV signal originating from ^{26}Al. Ref. [37] showed that it accounts for roughly half of the disk component of the 511 keV signal, and we will confirm this. The contribution of ^{44}Ti and ^{56}Ni positrons cannot be evaluated in that way because of their shorter lifetimes. A corollary is that positron escape from supernovae and their remnants can be a serious issue, and can prevent the determination of the positron injection rate directly from the isotope yields [98, 99]. Estimates of the isotope production in stars and of positron escape fractions suggest that it should make up most of the remaining disk emissivity [41, 37].

2.3 Dark Matter Halo Profile

Many-body simulations of the formation of galactic halos by collapsing dark matter particles predict a triaxial halo (see for example [22]), which however becomes more approximately spherical near the galactic center when the effects of baryons are taken into account [21]. For simplicity we will consider the halos to be spherically symmetric in most of the present work, although we will show that adding a realistic degree of oblateness does not significantly alter the fit. To further constrain the shape of the halo we will refer to results of the *Via Lactea II* simulation [100], which modeled the collapse of a Milky Way-sized ($2 \times 10^{12}\, M_\odot$) collection of over 10^9 particles. We chose *Via Lactea II* because it was specifically geared towards the study of the dark matter halo of the Milky Way. Among the many known parametrizations of the radial mass-energy density distribution, two have been especially successful at parametrizing results of recent simulations. These are the Einasto profile

$$\rho(r) = \rho_s \exp\left(-\left[\frac{2}{\alpha}\left(\frac{r}{r_s}\right)^\alpha - 1\right]\right) \tag{2.1}$$

and the generalized Navarro-Frenk-White (NFW) profile,

$$\rho(r) = \rho_s \frac{2^{3-\gamma}}{(r/r_s)^\gamma (1 + r/r_s)^{3-\gamma}}. \tag{2.2}$$

In both cases r is the galactocentric radius, while r_s, α and γ are parameters fit to N-body simulation results. The main galactic halo of the *Via Lactea II* simulation may be fit to an Einasto profile with $r_s = 25.7$ kpc and $\alpha = 0.17$, or to an NFW profile with $r_s = 26.2$ kpc and a central slope of $\gamma = 1.2$ [101]. The overall density normalization ρ_s can be computed from the local dark matter density which we take to be $\rho_\odot = 0.4$ GeV cm^{-3} [102] at the sun's position $r_\odot = 8.5$ kpc [103].

2.4 DM and the 511 keV sky distribution

Although the decaying DM scenario [104] was already shown to be highly disfavoured in refs. [95, 96], for completeness we will retest it in the present work. The flux of 511 keV photons from an e^+ produced in the decay of a metastable DM particle χ of mass m_χ is

$$d\Phi = 2(1 - 0.75 f_p) \frac{d\Omega}{4\pi} \int_{l.o.s.} \frac{\rho(\ell)}{m_\chi \tau} d\ell \tag{2.3}$$

The integral is along the observer's line of sight parametrized by ℓ, τ is the lifetime, $\rho(\ell)$ is its position-dependent density and $f_p = 0.967 \pm 0.022$ is the positronium fraction [36]. It corresponds to the global probability that a given e^+e^- annihilation take place via positronium formation. The latter can occur in the triplet state ortho-positronium (o-Ps) or the singlet state para-positronium (p-Ps). To conserve angular momentum, only p-Ps may decay into two 511 keV photons.

If the positrons are instead produced in a scattering or annihilation event, the observed flux takes a similar form:

$$d\Phi = 2(1 - 0.75 f_p) \frac{d\Omega}{4\pi} \int_{l.o.s.} \frac{1}{2} \frac{\langle \sigma v \rangle \rho^2(\ell)}{m_\chi^2} d\ell \tag{2.4}$$

where $\langle \sigma v \rangle$ is the thermally averaged cross-section for annihilations or excitations of the DM particles that produce e^+e^- pairs. Henceforth we will use "scattering" as shorthand for either XDM scattering or annihilating light DM, since both processes will look like (2.4) to an observer. The density-squared dependence of this integral means that the observed flux is much more concentrated in the galactic center than in the decay case; this is why scattering gives a much better fit to the observed shape than do decays.

The forms (2.3,2.4) are only strictly correct if positrons annihilate close to where they were formed. Despite recent studies [105, 106] the problem of positron transport in the interstellar medium cannot be considered as fully settled. In the absence of strong theoretical and observational constraints, we will assume that positron transport is a small effect in the present investigation. We will briefly return to this issue in Section 2.6.

Moreover, we have for simplicity assumed that $\langle \sigma v \rangle$ in (2.4) is independent of r, but this is not a good approximation for all models. In particular, for the standard XDM scenarios with a total energy gap $\delta E > 0$ between the ground state and excited state(s), there is a threshold value for the relative velocity, $v_t = 2\sqrt{\delta E / m_\chi}$, which appears in the excitation cross section as $\sigma v \sim \sigma_0 \sqrt{v^2 - v_t^2}$ [47]. Because the DM velocity dispersion $v_0(r)$ depends strongly upon r near the galactic center, this factor can then introduce significant r dependence into the phase-space average $\langle \sigma v \rangle$. There are several situations where this is not important: MeV DM undergoing pure annihilations [46, 107], metastable XDM models where $\delta E \ll m_e$ or $\delta E < 0$ [50, 52], and standard XDM models where $m_\chi \gtrsim$ TeV, in which case v_t is small compared to $v_0(r)$. For XDM models with $m_\chi \lesssim$ TeV, a more detailed study should be done.

In addition to the dark matter source of positrons, we included a disk component that models β^+ emission from radioactive isotopes including ^{26}Al and ^{44}Ti, whose flux at earth is analogous to eq. (2.3); the combination $\rho/(m_\chi \tau)$ becomes a density per unit time $\dot{n}$ of positron-producing radioactive decays. We considered two density models for this component. The first is a Robin young stellar disk (YD) model, correlated to the distribution of young stars, [108, 37],

$$\dot{n}_{YD}(x, y, z) = \dot{n}_0 \left[e^{-\left(\frac{a}{R_0}\right)^2} - e^{-\left(\frac{a}{R_i}\right)^2} \right], \tag{2.5}$$

with

$$a^2 = x^2 + y^2 + z^2/\epsilon^2. \tag{2.6}$$

The fixed disk scale radius is $R_0 = 5$ kpc and the fixed inner disk truncation radius is $R_i = 3$ kpc. We varied the vertical height scale $z_0 = \epsilon/R_0$ between 50 pc and 140 pc. (Ref. [40] used the 1809 keV line to fit the ^{26}Al distribution to a YD distribution with $z_0 = 125$ pc.) For comparison we also took an old disk (OD) model:

$$\dot{n}_{OD}(x, y, z) = \dot{n}_0 \left[e^{-\left(0.25 + \frac{a^2}{R_0^2}\right)^{1/2}} - e^{-\left(0.25 + \frac{a^2}{R_i^2}\right)^{1/2}} \right], \tag{2.7}$$

with $R_0 = 2.53$ kpc, $R_i = 1.32$ kpc and a vertical height scale z_0 which was varied from 150 to 250 pc.

2.5 Results

We tested our DM scenario against the INTEGRAL/SPI data by a model-fitting procedure applied to about 8 years of data collected in an energy bin of 5 keV width centred around 511 keV. For this, a model for the sky emission is convolved by the instrument response function and fitted to the data simultaneously to a model for the instrumental background noise in the Ge detectors.

Our fitting procedure is the same as the one described in section 4.2.1 of [37]. The likelihood L of a model assuming a Poisson distribution of events in each of the N

data bins is

$$L = \prod_{i=1}^{N} \frac{\lambda_i^{n_i} e^{-\lambda_i}}{n_i!}. \tag{2.8}$$

n_i is the number of events recorded in bin i by the SPI experiment, and $\lambda_i = \sum_k \alpha_k s_i^k + b_i(\beta)$ is the predicted number of counts per bin, including the background b_i and the source $s_i^k = \sum_j f_j^k R_i^j$. The factor R_i^j is the instrument response matrix and f_j^k is the intensity computed with the line-of-sight integrals. In our case, the sum over k has two terms: the dark matter term and the disk component. The coefficients α_k and β are the scaling factors that are adjusted by the fit. The result of fixing the normalization α_{DM} is to fix $(m_\chi \tau_\chi)^{-1}$ in the case of decay and $\langle \sigma v \rangle_\chi m_\chi^{-2}$ for dark matter scattering. We use the maximum likelihood ratio test to estimate detection significances and errors. We calculate the log-likelihood ratio

$$\mathrm{MLR} = -2(\ln L_0 - \ln L_1), \tag{2.9}$$

where L_1 is the maximized likelihood of the model being tested, and L_0 is the maximum likelihood of the background model only, *i.e.,* $\alpha_k = 0$.

We compare the results of our DM models to the best phenomenological description by Weidenspointner *et al.* [39], where the authors fitted two spheroidal Gaussians and a young stellar disk to the then-available four-year data set.[1] We have updated their analysis, using the currently available eight-year data set and find an MLR of 2693. Although non-nested models cannot be directly compared through the MLR, this serves as a figure of merit for a model such as the dark matter ones to match, if it is to provide a competitive fit relative to the phenomenological shape models.

We performed two analyses, firstly fixing α and r_s to values favoured by *Via Lactea II*, using the young disk model parameters favoured by the ^{26}Al analysis of [40], and

[1] The 8 degrees of freedom in the reference model are: the width and normalization of each Gaussian, the inner and outer disk truncation, the disk scale height and the disk normalization.

Table 2.1: Summary of best fits to the INTEGRAL/SPI data, with parameters fixed to results of the *Via Lactea II* simulation. This corresponds to $r_s = 26$ kpc and $\alpha = 0.17$ for an Einasto profile (2.1) or $\gamma = 1.2$ for an NFW profile (2.2). The disk component is the young disk (2.5) with $z_0 = 125$ pc. All-sky fluxes are in units of 10^{-4} ph cm^{-2}s^{-1}, the lifetimes τ are in seconds, and cross-sections $\langle \sigma v \rangle$ have units of cm^3 s^{-1}. We have highlighted the best fit scenarios in bold.

Channel	**Profile**	**MLR**	**Disk flux**	**DM flux**	**DM lifetime or cross-section**
decay	Einasto only	2139	—	174.5 ± 3.5	$\tau_\chi = 1.1 \times 10^{26} (\mathrm{GeV}/m_\chi)$
	Einasto + Disk	2194	10.60 ± 1.42	148.6 ± 5.1	$\tau_\chi = 1.3 \times 10^{26} (\mathrm{GeV}/m_\chi)$
scattering	Einasto only	2611	—	24.02 ± 0.47	$\langle \sigma v \rangle_\chi = 5.8 \times 10^{-25} (m_\chi/\mathrm{GeV})^2$
	Einasto + Disk	**2668**	$\mathbf{9.98 \pm 1.32}$	$\mathbf{21.16 \pm 0.59}$	$\boldsymbol{\langle \sigma v \rangle_\chi = 5.1 \times 10^{-25} (m_\chi/\mathrm{GeV})^2}$
	Einasto (oblate) + Disk	**2669**	$\mathbf{8.74 \pm 1.31}$	$\mathbf{21.06 \pm 0.61}$	$\boldsymbol{\langle \sigma v \rangle_\chi = 4.9 \times 10^{-25} (m_\chi/\mathrm{GeV})^2}$
	NFW only	1602	—	6.72 ± 0.17	$\langle \sigma v \rangle_\chi = 8.2 \times 10^{-26} (m_\chi/\mathrm{GeV})^2$
	NFW + Disk	2155	26.45 ± 1.25	4.90 ± 0.18	$\langle \sigma v \rangle_\chi = 6.1 \times 10^{-26} (m_\chi/\mathrm{GeV})^2$

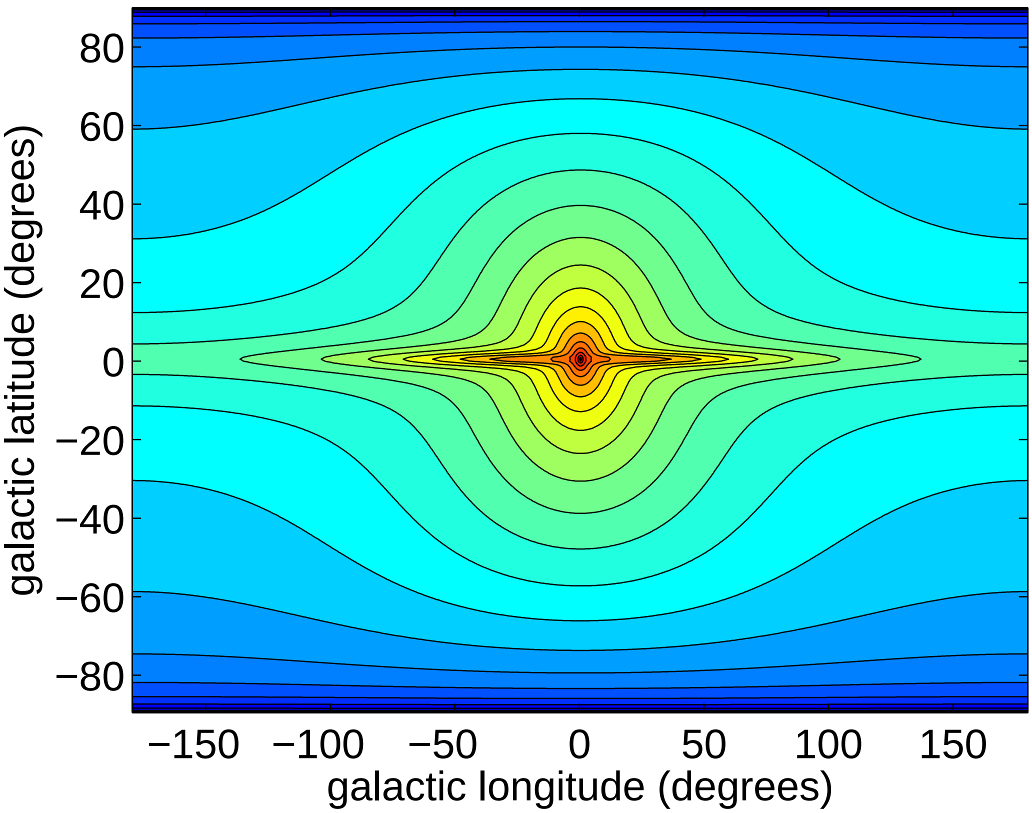

Figure 2.1: Intensity skymap predicted by *Einasto + disk* model. The bulge component is due to emission from scattering or annihilating dark matter in an Einasto profile, and the disk component can be attributed to decay of radioactive species including mainly ^{26}Al.

finding the overall normalizations of the disk and Einasto components that best fit the INTEGRAL/SPI data. As a second analysis, we varied the parameters α and r_s of the Einasto profile, as well as the height scales z_0 for both young and old disk populations. As we will show, adding these three extra degrees of freedom does not signifcantly improve the likelihood of the model, suggesting that the *Via Lactea II* parameters are a good fit for the scattering XDM or annihilating DM hypothesis.

Table 2.1 summarizes our main results. The dark matter halo parameters were set to those favoured by *Via Lactea II*, for an Einasto (NFW) profile with $r_s = 26$ kpc and $\alpha = 0.17$ ($\gamma = 1.2$). We used the young disk model (2.5) of [40], with the

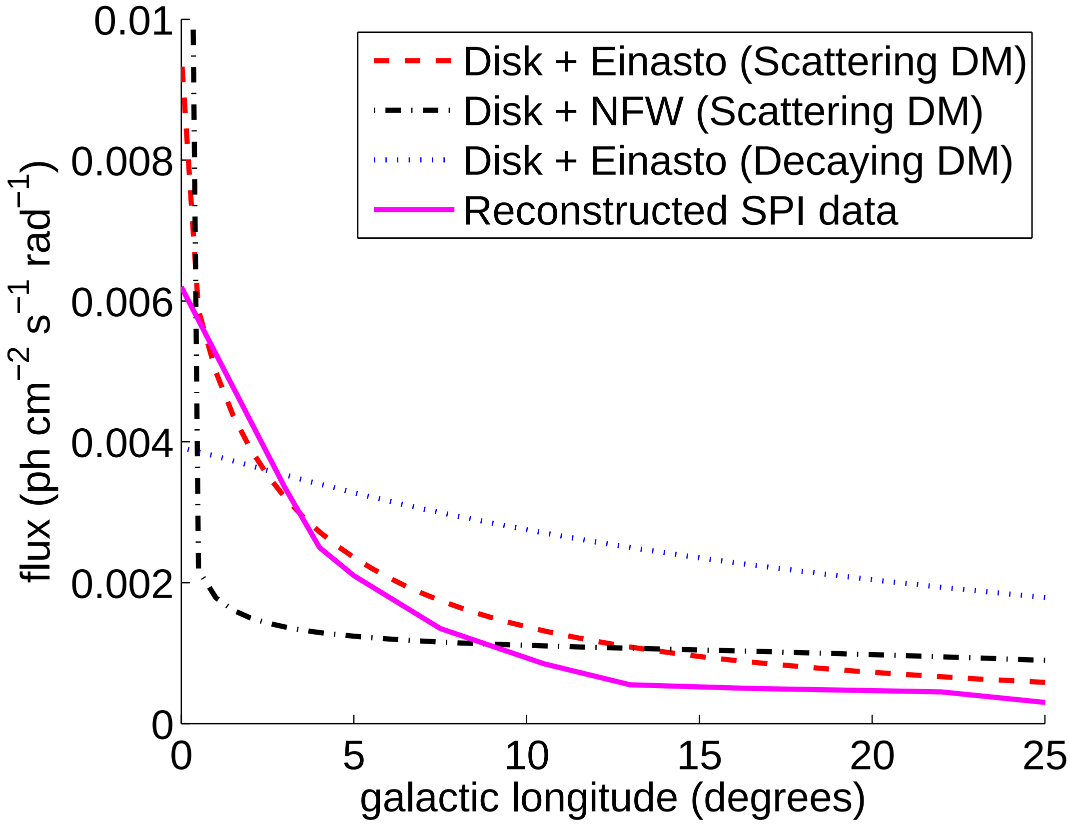

Figure 2.2: Longitudinal dark matter profiles for the three dark matter models considered, including the disk component from radioactive isotopes. Fluxes are integrated over galactic latitudes $-15^\circ < b < 15^\circ$. "Scattering" refers to either scattering multi-state dark matter or annihilating light dark matter. The solid magenta line is left-right averaged, reconstructed SPI data from [41], taken from the skymaps of [42].

fixed scale height $z_0 = 125$ pc corresponding to the ^{26}Al distribution inferred from 1809 keV line data. We considered both decaying (2.3) and scattering (2.4) dark matter. The scattering scenario provided a consistently better fit (ΔMLR$>$ 400), and the fit to the Einasto profile was significantly better than to the NFW profile (Δ MLR= 513). Motivated by the triaxial halo shapes mentioned above [21], we also examined an oblate Einasto profile with a semi-major axis ratio $c/a = 0.8$. This is denoted "Einasto (oblate) + disk" in Table 2.1. While this reduced the required flux from the disk component, it did not produce any significant change in MLR.

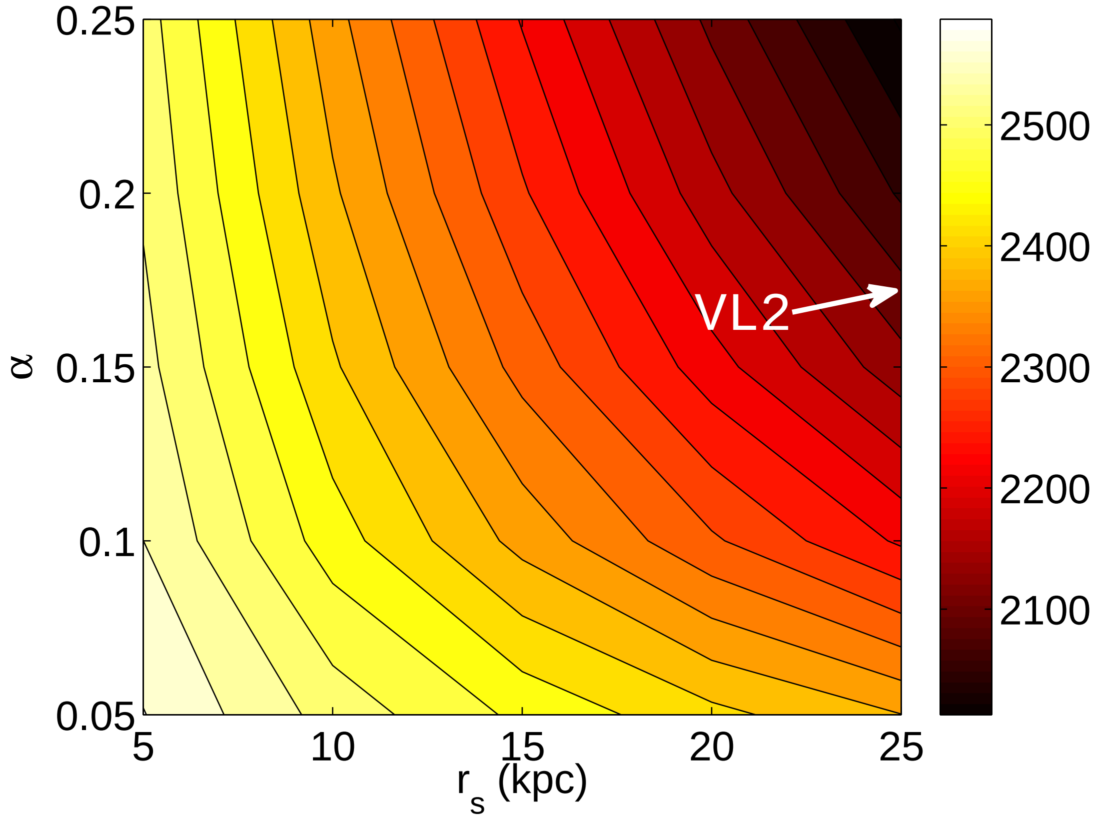

Figure 2.3: Maximum log-likelihood ratio (MLR) obtained in the decaying dark matter + young disk scenario as a function of the Einasto halo parameters. The values favoured by the *Via Lactea II* N-body simulation, labeled *VL2*, do not give a good fit to the INTEGRAL/SPI data and are far away from the favoured region.

The best-fit lifetimes (cross-sections) of the XDM model in the decaying (scattering) scenario are presented in the final column of Table 2.1. Figure 2.1 shows the all-sky map of the Einasto + disk best fit to the INTEGRAL/SPI data, and Figure 2.2 shows the longitudinal profile of the three dark matter models (including disk components) in comparison with a reconstruction of the SPI data. This clearly illustrates how decaying dark matter produces a profile that is far too flat, while an NFW distribution results in an unrealistic sharp central peak. Decaying dark matter in an NFW profile (not illustrated) displays a combination of these flaws. On the other hand, the scattering model produces MLR = 2668, which is not far below that of the

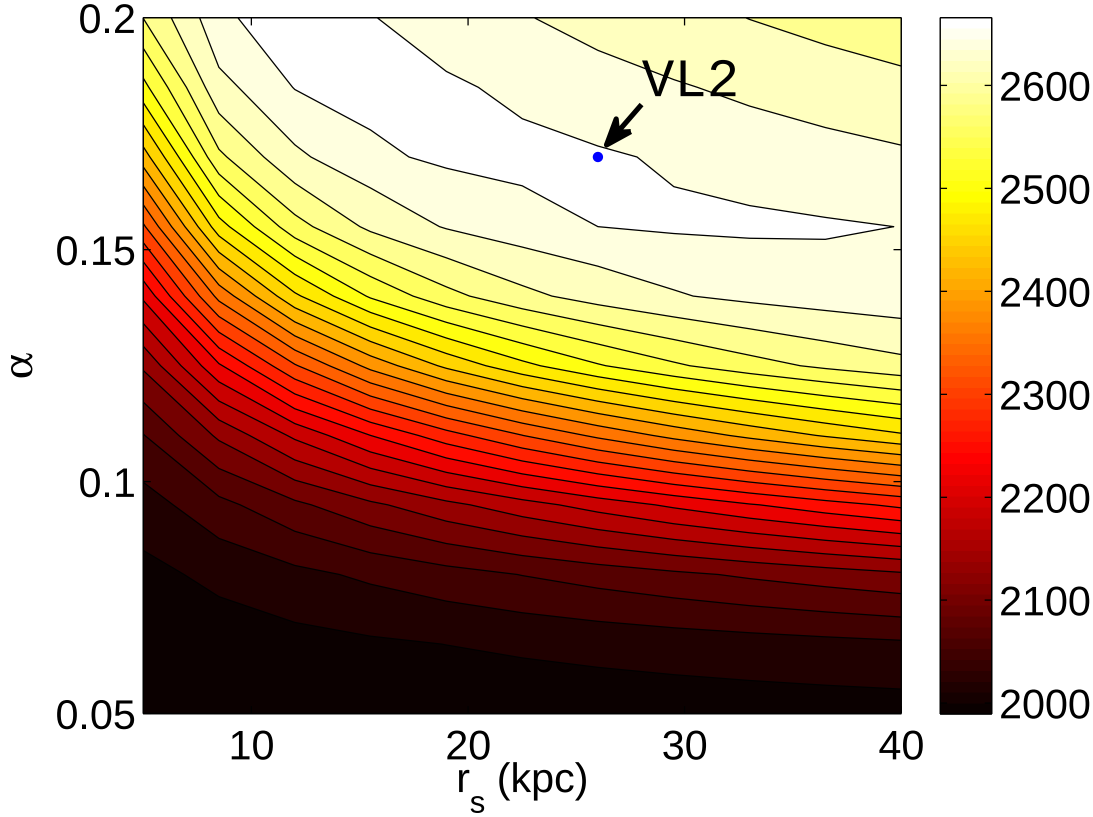

Figure 2.4: Same as Figure 2.3, but with scattering dark matter (2.4). The MLR obtained with the *Via Lactea II* parameters (white dot) is within $\Delta MLR = 5$ of the best fit ($r_s = 12$ kpc, $\alpha = 0.2$), which means that the VL2 parameters likely correspond to the correct model if the scattering or annihilating dark matter hypothesis is true.

best-fit phenomenological model, the latter having MLR = 2693 and six additional fitting parameters. The reduced χ^2 of our dark matter model computed on a pointing basis is as good as that of the phenomenological model, with a value of 1.007.

Letting r_s, α and z_0 vary freely yields some improvement. Figure 2.3 shows a contour plot of the MLR obtained from the decay scenario (2.3). The favoured region in the lower-left corner, with an MLR of 2558, corresponds to an extremely cuspy DM halo that is quite far removed from realistic DM halo models.

The equivalent picture for scattering DM is illustrated in Figure 2.4. The overall best fit was found to be for a profile with $\alpha = 0.2$, $r_s = 12$ kpc and $z_0 = 140$ pc, with an MLR of 2673. However, this difference is only marginally significant. Indeed, by adding three degrees of freedom, such an improvement should happen by chance 17% of the time due to statistical fluctuations in the data. We found that the young disk (YD) model consistently gave a better fit than the old disk (OD) model, and that adjusting z_0 over a range from 70 to 200 pc did not produce any significant improvement in the MLR. Finally, we checked that choosing a closer value for the galactocentric distance of $R_. = 8.2$ kpc, as suggested by recent studes such as [102] produced a negligible change in the fit ($\Delta MLR < 1$).

2.6 Discussion and Conclusion

We have made the first direct comparison of dark matter predictions for the observed 511 keV spatial intensity distribution since the earliest data release of INTEGRAL/SPI. Our favoured fit corresponds to a scattering excited DM or annihilating light DM model in an Einasto density distribtion (2.1) with parameters fixed to the *Via Lactea II* results. We confirm previous analyses showing that decaying dark matter is ruled out due to its too-broad spatial distribution. After correct normalization of the intensity, our best-fit model requires a cross section for $\chi\chi$ to produce positrons of $\langle \sigma v \rangle_\chi = 5.1 \times 10^{-25} (m_\chi/\mathrm{GeV})^2$ cm^{3}s^{-1}. If m_χ is in the 10-1000 GeV range as favoured by most WIMP models, this means $\langle \sigma v \rangle$ is in the interval $[10^{-23}, 10^{-19}]$ cm^{3}s^{-1}. The fact that this is far above the annihilation cross section of 3×10^{-26} cm^{3}s^{-1} needed to get the observed relic density is not problematic, because the physical process required in these models is inelastic scattering to an excited state rather than annihilation.

Because we neglected r-dependence in the averaged cross section $\langle \sigma v \rangle$, these results apply to upscattering XDM with high masses $m_\chi \gtrsim$ a few TeV, metastable XDM models [51, 52], and direct annihilation of MeV DM. To cover the case of lighter XDM models, a more detailed analysis taking account of the radial dependence of the DM velocity dispersion in the Galaxy would be needed. We hope to return to this in future work.

For light $\sim$ MeV DM annihilating directly into e^+e^-, our required cross section is $\langle\sigma v\rangle \sim 10^{-31}$ cm^{3}s^{-1}, which is too small to give the right relic density. This need not be a problem; it only requires there to be additional stronger annihilation channels into invisible particles, for example dark gauge bosons [107] or dark neutrinos [109].

There are two unknowns that could change our analysis in significant ways. One is the distance by which positrons propagate between creation and annihilation. If it is larger than $\sim$ 100 pc, it could alter the overall breadth of the spatial extent of the signal, as well as introduce deviations from axial symmetry, depending on the conditions of the interstellar medium in the bulge. Further observational evidence constraining the structure of magnetic fields (for example synchrotron emission studies [110]) will be needed to reduce these uncertainties. A second unknown is the degree of departure of the DM halo from spherical symmetry, which definitely occurs in N-body simulations [21]. We showed that adding some oblateness had little effect on the fits, though the nature and extent of triaxiality near the galactic center depends heavily upon the inclusion of baryons in the simulations, a challenging field which is still in its early stages. We look forward to improvements in these studies that will help to constrain the theoretically expected extent of triaxiality in the DM halo.

We have confirmed the findings of previous studies concerning the disk emission. Given a young disk model for the distribution of ^{26}Al, the observed flux of 1809 keV gamma rays [40] translates into an expected 511 keV flux of (7.33 $\pm$ 0.89) $\times 10^{-4}$ ph cm^{-2}s^{-1}. This alone accounts for 73% of the disk component favoured by our model. If similar amounts of ^{44}Ti are present in the Galaxy, there is no need for an extra component to explain the disk component of the 511 keV signal. On the other hand, simulations show that in addition to the DM halo, there may also be a DM disk. This would give an extra DM contribution to the disk component of the 511 keV emission. However, there is as yet no direct evidence for a DM disk in our own galaxy [111, 112].

It is worth emphasizing that only two degrees of freedom were required to obtain the MLR of 2668 in the DM scattering/annihilation scenario. This is in contrast to the 8 d.o.f. necessary to obtain an MLR of 2693 with one best-fit phenomenological model. A further advantage of the DM model is that it is motivated by particle physics and cosmology, and it has a concrete, calculable production mechansim for the excess electron-positron pairs. Our results are independent of the details of the DM model, so long as the scattering events lead directly to a low-energy e^+e^- pair.

We find these results to be encouraging for the dark matter interpretation of the 511 keV excess, an anomaly that was first seen in 1972 by balloon-borne detectors [29]. We hope that the experimental hard X-ray / soft gamma-ray astronomy community will be motivated to consider a higher-resolution instrument that would be sensitive to the 511 keV region of the spectrum in the future. Such observations would help to shed more light on this intriguing possibility, which could be the first evidence for nongravitational interactions of dark matter.

Bridge

From low-energy positrons, we now move to high-energy signals as observed by the PAMELA and Fermi-LAT experiments. Whereas the positrons detected in the previous chapter were observed indirectly, through their annihilation line, those observed at high energies, from 10-200 GeV, are captured directly by satellites in orbit around the earth. The higher energies mean that modelling of the cosmic ray propagation will be particularly important, and will significantly affect the results. Once more, the focus is on a particle dark matter interpretation of an unexplained population of positrons. The key differences with the INTEGRAL source are the non-directional nature of the signal, the specific mass required of the DM candidate and the methods of constraining the DM explanation. The next chapter will focus on explaining the lepton data by including subhalos as sources of cosmic ray electrons and positrons, whereas a direct confrontation with gamma-ray constraints from Fermi-LAT will be presented in Chapter 4.

Chapter 3

Leptons from Dark Matter Annihilation in Milky Way Subhalos

Work published with James M. Cline and Wei Xue
in Physical Review D82 (2010) 083512

Abstract

Numerical simulations of dark matter collapse and structure formation show that in addition to a large halo surrounding the baryonic component of our galaxy, there also exists a significant number of subhalos that extend hundreds of kiloparsecs beyond the edge of the observable Milky Way. We find that for dark matter (DM) annihilation models, galactic subhalos can significantly modify the spectrum of electrons and positrons as measured at our galactic position. Using data from the recent *Via Lactea II* simulation we include the subhalo contribution of electrons and positrons as boundary source terms for simulations of high energy cosmic ray propagation with a modified version of the publicly available GALPROP code. Focusing on the DM DM $\to$ 4e annihilation channel, we show that including subhalos leads to a better fit to both the Fermi and PAMELA data. The best fit gives a dark matter particle mass of 1.2 TeV, for boost factors of $B_{\rm MH} = 90$ in the main halo and $B_{\rm SH} = 1950 - 3800$ in the subhalos (depending on assumptions about the background), in contrast to the

0.85 TeV mass that gives the best fit in the main halo-only scenario. These fits suggest that at least a third of the observed electron cosmic rays from DM annihilation could come from subhalos, opening up the possibility of a relaxation of recent stringent constraints from inverse Compton gamma rays originating from the high-energy leptons.

3.1 Introduction and Summary

Recent observations of the spectrum of electrons and positrons by the Fermi collaboration [57] and of the positron fraction $e^+/(e^+ + e^-)$ by the PAMELA experiment [113] hint at a possible new source of cosmic ray e^+ and e^- in the TeV energy region. According to recent models [49, 62, 63, 64, 65, 66, 67], these excesses could be the signal of dark matter (DM) annihilation via a dark sector gauge boson that allows a Sommerfeld-type enhancement at low velocities. Best fits to the electron-positron spectra indicate that the dark matter candidate χ that annihilates within the galaxy should have a mass of around $M_{\mathrm{DM}} \simeq 1$ TeV, and annihilate into two pairs of light leptons via the process DM DM $\to \phi\phi \to 4e$ or DM DM $\to \phi\phi \to 4\mu$. The particle ϕ should furthermore be light enough not to decay into $p\bar{p}$ pairs since excess antiprotons are not observed by PAMELA.[1]

While the visible galaxy spans a diameter of approximately 40 kpc and a height of 8 kpc, N-body simulations [18, 17] predict a roughly spherical structure of dark matter subhalos whose peak concentration occurs ~ 70 kpc from the galactic center (GC) and extends as far as several thousand kpc. Relative velocities between particles in these regions are one to two orders of magnitude smaller than in the Milky Way's main halo, and the relative overdensity of such regions make them ideal sources of DM annihilation products. This has been explored by other authors in the context of gamma ray signals originating from subhalos [85, 86, 87, 88, 4, 67] and found to be

[1] However see ref. [66] for arguments that this constraint may not be necessary, due to astrophysical uncertainties in the background model.

significant. These gamma rays, which originate from final-state radiation, are not the main product of this class of DM annihilation; rather they are by-products of charged particles and neutral pions.

In this chapter we consider the possibility that the excess leptons observed by PAMELA and Fermi/LAT themselves have a strong component originating in the subhalos. This possibility was previously considered in ref. [89], but there it was assumed that one or two nearby subhalos would dominate any additional contribution to the signal. Here we will show that the best fits to the data are found by taking into account the full ensemble of substructures. It will be seen that the subhalos that individually contribute weakly to the lepton flux are nevertheless so numerous that their combined effects cannot be neglected.

We used a modified version of the GALPROP cosmic ray propagation code, in which leptons from distant subhalos give a new source term at the boundary of the diffusion zone. The data of the *Via Lactea II* simulation [18] are taken as our model for the subhalos. We allow for independently adjustable boost factors for the main halo and subhalos, motivated by the fact that Sommerfeld enhancement of the annihilation cross section can be much greater in the subhalos due to their lower velocity dispersion [49]. If we also allow the background electron and positron flux normalizations to be rescaled, as in references [114, 64, 115], we find that the inclusion of subhalos gives a much better fit to both cosmic ray data sets, with the best-fit DM particle mass of $M_{\rm DM} = 1.2$ TeV.

On the other hand, if the e^+ and e^- backgrounds are instead fixed at the GALPROP output level, it is known that there is a discrepancy between the boost factors needed for explaining PAMELA and Fermi, even in the standard main halo-only scenario. This discrepancy remains in the subhalo scenario, where we find that a DM mass of $M_{\rm DM} = 2.2$ TeV improves the fit to the Fermi data, whereas the fit to PAMELA is not improved.

Our results suggest that the inclusion of leptons from DM annihilation in the subhalos surrounding the Galaxy should affect not only the amplitude, but also the shape of the observed spectrum due to inverse Compton scattering (ICS) of the leptons with the radiation fields inside the observable galaxy. This is potentially important because the most recent constraints on this effect [115, 114] effectively rule out the DM annihilation interpretation of the Fermi excess for a non-isothermal profile, and leave only a very reduced corner of parameter space consistent with PAMELA. We hope to quantitatively address the question of whether substructure indeed allows for relaxation of these constraints in the near future.

In Section 3.2 we briefly describe GALPROP and our choices of parameters for cosmic ray propagation. Section 3.3 details the modifications we made to GALPROP in order to include the e^+e^- pairs from DM annihilation in the subhalos. The results are presented in Section 3.4, and conclusions in section 3.5.

3.2 Cosmic ray propagation models

Inside the diffusive zone of the Galaxy, cosmic ray species propagate according to the transport equation [116]

$$\begin{aligned} \frac{\partial \psi}{\partial t} &= q(r,z,p) + \nabla \cdot (D_{xx} \nabla \psi - \vec{V}_c \psi) \\ &\quad + \frac{\partial}{\partial p} p^2 D_{pp} \frac{\partial}{\partial p} \frac{1}{p^2} \psi - \frac{\partial}{\partial p} \left[\frac{dp}{dt} \psi - \frac{p}{3} (\nabla \cdot \vec{V}_c) \psi \right]. \end{aligned} \tag{3.1}$$

$\psi(\vec{x},p,t)$ is the particle density per unit momentum $p \equiv |\vec{p}|$, $q(\vec{x},p)$ is the source term, D_{xx} is the energy-dependent diffusion coefficient, D_{pp} quantifies reacceleration via diffusion in momentum space and $\vec{V}_c$ is the convection velocity. In the case of composite species, terms accounting for radiative decay and fragmentation must furthermore be included. For D_{xx} we use the parametrization [117]

$$D_{xx} = D_{0xx} \left(\frac{E}{4\ \mathrm{GeV}} \right)^{\delta}, \tag{3.2}$$

where E is the particle energy and D_{0xx} is the diffusion coefficient at reference energy $E = 4$ GeV. [2] D_{0xx} and the exponent δ are determined by fitting to heavy nuclei cosmic ray data.

There are two widely-used approaches to cosmic ray propagation within the galaxy. The first is a semi-analytic model in which the baryonic component of the galaxy is accelerated in a thin disk at $z = 0$ from which particles diffuse according to a Bessel series expansion until $z = \pm L_{\rm eff}$, beyond which they freely escape. The second, fully numerical, approach implemented in the publicly available GALPROP [116] package uses a Crank-Nicholson scheme to solve eq. (3.1) within a diffusion zone of height $L_{\rm eff}$ and radius $R_{\rm eff}$. An advantage of the latter technique is that it allows the use of realistic maps of radiation and gas in the propagation scheme. While this is not the focus of this work, it is relevant to point out that differences between models are responsible for differences between fits in recent dark matter annihilation models. This discrepancy has been known for some time; see for example the discussion in ref. [118]. Nevertheless, we shall henceforth focus exclusively on the numerical approach, given its successes in fitting cosmic ray spectra of heavier species. Our simulations were run using a modified version of GALPROP 50.1p that was graciously provided by the authors of ref. [62] and which we further modified to handle subhalo sources.

The strongest available constraints on cosmic ray propagation models are ratios of secondary-to-primary species such as B/C or sub-Fe/Fe. The authors of ref. [117] conducted an exhaustive search of the GALPROP parameter space for input values that gave best fits to 12 secondary/primary cosmic ray experiments. For our simulation runs we took their best fit parameters: $D_{0xx} = 6.04 \times 10^{28}$ cm^2 s^{-1} (0.19 kpc^2/Myr), $L_{\rm eff} = 5.0$ kpc, $\delta = 0.41$, with no convection. We used an Alfvén speed, the typical speed of MHD waves responsible for diffusive reacceleration, $V_A = 31$ km s^{-1}. This gave a slightly better fit to the HEAO B/C data [119]. It should be noted that these

[2] More precisely, diffusion depends on particle rigidity, the energy divided by the charge. We assumed the particles have unit charge here.

parameters are quite different from the corresponding best fits of the semi-analytic model used, for example by Meade et al. [64].

3.3 Including subhalo flux in GALPROP

The many-body simulation *Via Lactea II* [18], which modeled the evolution and collapse of more than 10^9 particles over the history of a Milky Way-sized structure, resolves over 20,000 dark matter subhalos around the galactic host halo. The data characterizing each of these subhalos is publicly available [120]. While the visible galaxy is only some 40 kpc across, these subhalos extend as far out as 4000 kpc from the galactic center. Each subhalo is locally much denser than the host halo and has its own radial velocity dispersion profile. The annihilation rate of dark matter, proportional to ρ^2, should thus spike within these subsystems when compared to the annihilation rate of diffuse DM particles of the host halo.

For a given subhalo i at a distance ℓ_i from the edge of the diffusion zone of the galaxy, the flux of e^+ or e^- on this boundary takes the form

$$\frac{d\Phi_i}{dE} = B_{\rm SH}\langle\sigma v\rangle\,\frac{dN}{dE}(\ell_i)\int_0^\infty \frac{r^2\rho_i^2}{\ell_i^2 M_{\rm DM}^2}\,dr \tag{3.3}$$

where $B_{\rm SH}$ is an average boost factor for the subhalos due to Sommerfeld enhancement for example, and $\rho_i(r)$ is the mass density profile of the subhalo. The unboosted cross section is assumed to be $\langle\sigma v\rangle = 3\times 10^{-26}$ cm^3 s^{-1} in accordance with the standard assumption that the DM abundance was determined by freeze-out starting from a thermal density. In a more exact treatment, the boost factor would be velocity dependent [121, 122] and appear within the average over DM velocities indicated by the brackets in $\langle\sigma v\rangle$. Moreover each subhalo in general has a different boost factor since the velocity dispersions that determine $B_{\rm SH}$ depend on the size of the subhalo [85]. For this preliminary study, we simply parametrize the effect by an average boost factor, where the averaging includes the sum over all subhalos as well as the integration over velocities.

The energy spectrum dN/dE of electrons from the DM annihilations is taken for simplicity to be a step function at the interaction point, $dN/dE = M_{\rm DM}^{-1}\Theta(M_{\rm DM} - E_0)$, where E_0 is the energy immediately following the annihilation. We are interested in models where the DM particles initially annihilate into two hidden sector gauge or Higgs bosons, each of which subsequently decays into e^+e^- [49]. The four-body phase space would thus be a more exact expression for dN/dE, but the step function has the correct qualitative shape and is simpler to implement in GALPROP.

The energy of the electron at the edge of the galaxy is reduced from its initial value E_0 by scattering with CMB photons before reaching the galaxy (starlight, infrared radiation and synchrotron radiation are only important in the inner galaxy [123]), according to the loss equation $dE/d\ell = -\kappa E^2$ [64] where $\kappa = (4\sigma_T/3m_e^2)\, u_{\rm CMB} = 6.31 \times 10^{-7}$ kpc GeV^{-1}, $\sigma_T = \frac{8\pi}{3}(\alpha_{EM}\hbar/m_e c)^2$ is the Thomson cross-section and $u_{\rm CMB} = 0.062$ eV/cm^3 is the present energy density of the CMB. It is convenient to write the solution in the inverted form: $E_0 = (-\kappa\ell + 1/E(\ell))^{-1}$ for substitution into dN/dE. Numerically, we find that the losses outside the diffusion zone make a small correction, and that the distinction between E_0 and $E(\ell)$ is not important here.

Each subhalo is characterized by a density profile that has been fit to the Einasto form

$$\rho_i = \rho_{s,i} \exp\left[-\frac{2}{\alpha}\left(\left(\frac{r}{r_{s,i}}\right)^{\alpha} - 1\right)\right] \tag{3.4}$$

with $\alpha = 0.17$ [4]. The scale radius is found to be proportional to the radius $r_{v_{\rm max}}$ at which the velocity dispersion is at a maximum, through the relation $r_s \cong r_{v_{\rm max}}/2.212$, while the prefactor scales with the maximum velocity $v_{\rm max}$ as $\rho_s \cong v_{\rm max}^2/(0.897 \cdot 4\pi r_s^2 G)$.

To incorporate the contribution (3.3) to the lepton flux from the subhalos in GALPROP, we add delta function source terms to $q(r,z,p)$ for the cylindrical surface bounding the diffusion zone, as illustrated in fig. 3.1:

$$\begin{aligned} q_{\rm disk} &= 2\delta(z \pm h/2)\sum_i \frac{d\Phi_i}{dE}\cos\theta_i \\ q_{\rm band} &= 2\delta(r-R)\sum_i \frac{d\Phi_i}{dE}\sin\theta_i \end{aligned} \tag{3.5}$$

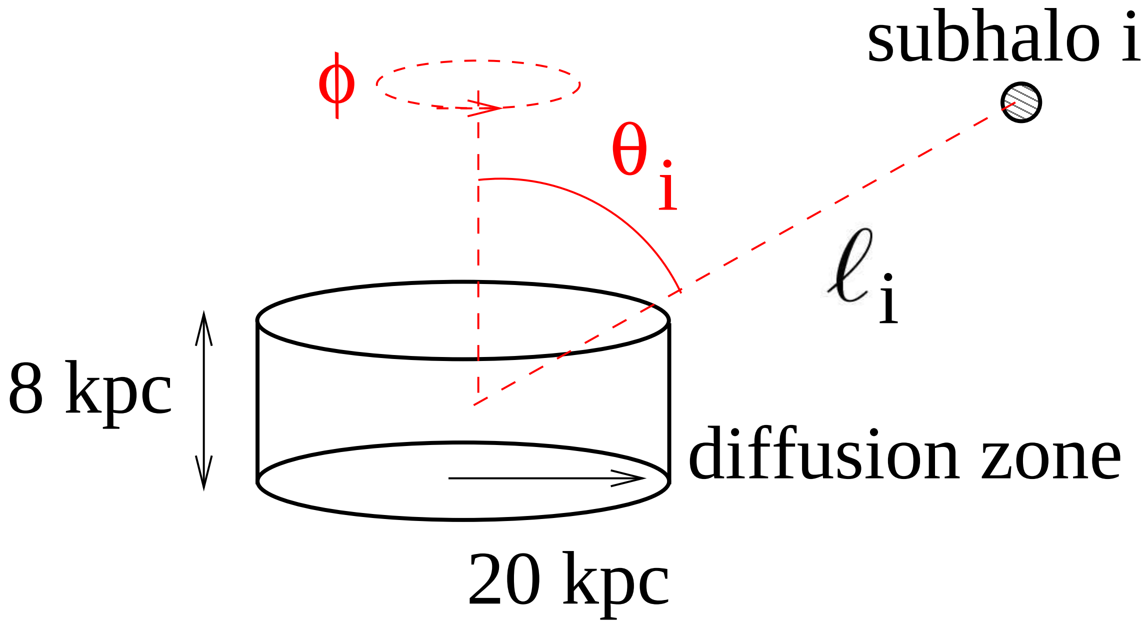

Figure 3.1: Geometry of a subhalo shining leptons on the boundary of diffusion zone of the galaxy.

where h and R are respectively the height and radius of the cylinder. The factor of 2 corrects for the fact that sources in GALPROP have no directionality, whereas the flux impinging on the surface is inward. The sum is over the 20,048 resolved subhalos in the *Via Lactea II* simulation, whose distribution is illustrated in figure 3.2. In addition, the sources were averaged over the azimuthal angle ϕ because GALPROP assumes cylindrical symmetry in its 2D mode (and the 3D mode runs too slowly for our purposes). Finally, the distance ℓ_i must be corrected for subhalos that are close to the diffusion zone; rather than the distance to the center of the galaxy, it should be the distance to the cylindrical boundary. On average, this is a reduction by 17 kpc compared to the distance to the galactic center.

Although most subhalos were located outside of the diffusion zone, there are 143 lying inside, whose contribution required special treatment. Assuming approximate isotropy, we took their entire flux of $e^+ + e^-$ to be pumped into the diffusion zone from the boundary rather than from their individual positions. Treating them in this manner allowed us to group their contribution with that of the other subhalos and

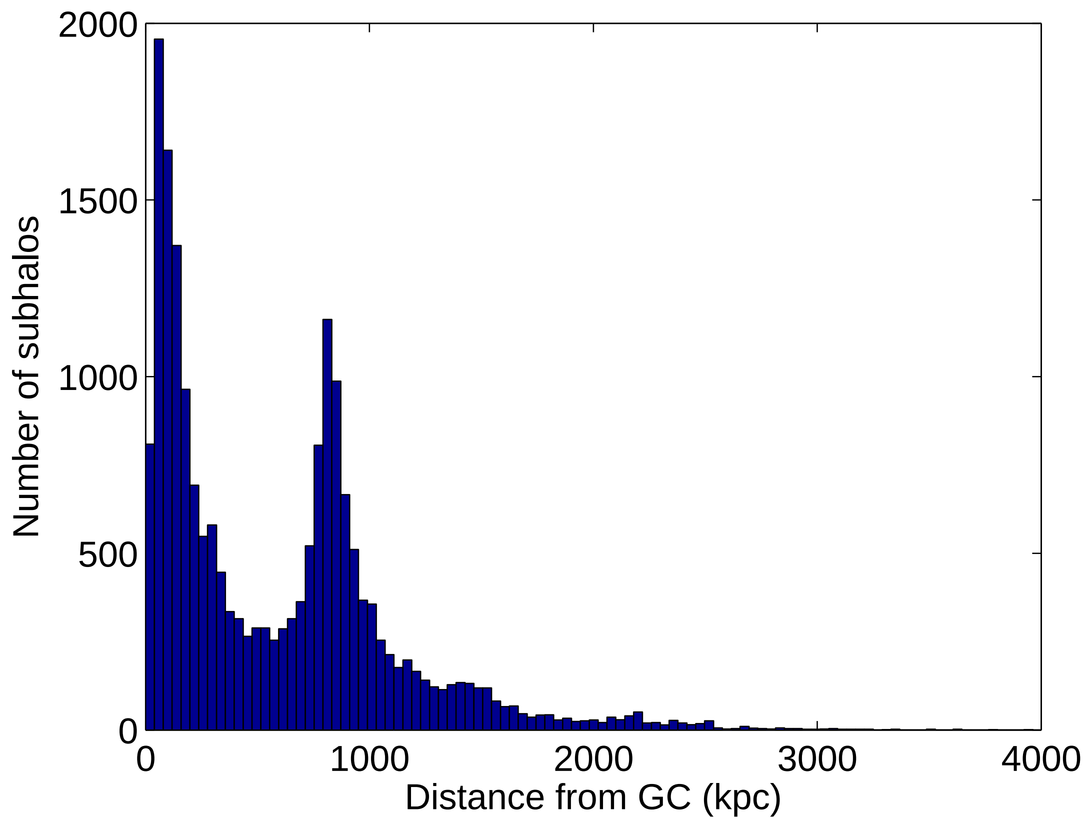

[t]

Figure 3.2: Histogram the distribution of *Via Lactea II* subhalos as a function of their distance from the galactic centre (GC). The first peak occurs at 70 kpc, and the second around 800 kpc. The trough is due to tidal disruption.

thus consider a single average boost factor for all subhalos. This approximation would break down if one subhalo happened to be very close to our position in the galaxy, but treating such a case would anyway require going beyond the standard cylindrical symmetry (2D) mode of GALPROP and using the much slower 3D mode. We believe this treatment is conservative in the sense that it should only underestimate the contributions of the nearby subhalos.

3.4 Numerical Results

We compared the observed flux of positrons and electrons generated by dark matter annihilation within the main halo (MH) to a scenario in which both main halo and subhalo (MH+SH) DM annihilation occurs. We restricted our analysis to the $DMDM \to 4e$ channel. This channel is simpler to analyze, and is somewhat less constrained by inverse Compton gamma ray constraints than the other 4-lepton final-state models, or those with only two leptons [64].

For the MH only scenario, the annihilation cross-section was augmented by a constant boost factor $B_{\rm MH}$, representing the effect of Sommerfeld or some other kind of enhancement [124, 125, 49, 61]. This was varied in order to find a best fit to each data set. A similar approach was used in the case of MH+SH, where we varied the MH and SH boost factors independently. This is justified by the expectation that Sommerfeld enhancement should be significantly larger in the subhalos due to their lower velocity dispersions [49]. The subhalo boost factor $B_{\rm SH}$ might also have further contributions besides Sommerfeld enhancement, such as the presence of unresolved subhalos that we do not take into account [4], as well as substructure within the subhalos themselves [85].

We minimized the chi squared coefficient

$$\chi^2 = \sum_i \frac{\left(\xi_{i,\,\rm exp} - \xi_{i,\,\rm model}\right)^2}{\sigma_{i,\,\rm exp}^2}, \tag{3.6}$$

where the sum runs over the measured or predicted values of ξ, which stands for either $E^3 d(\psi_{e^+} + \psi_{e^-})/dE$ in the case of the 25 Fermi data points, or $\psi_{e^+}/(\psi_{e^+} + \psi_{e^-})$ in the case of the PAMELA data, and $\psi_{e^\pm}$ is the flux of electrons or positrons. When fitting to PAMELA we excluded the first 8 of 16 data points, following the usual assumption that the dip relative to the background is accounted for by modulation effects on low-energy cosmic rays from solar wind [66].

3.4.1 Freely-varying background

Our best fits to the PAMELA and Fermi data were obtained by letting the astrophysical background electrons and positrons be rescaled by overall normalization factors, which was also the approach taken in references [64, 115, 114]. Adding subhalo contributions significantly improved the fits to both the Fermi and the PAMELA data. While the best overall fit with only MH electrons was for $M_{\rm DM} = 850$ GeV ($\chi^2_{\rm total} = 34.3$), the MH+SH scenario gave a best fit at $M_{\rm DM} = 1.2$ TeV ($\chi^2_{\rm total} = 16.5$). In this case $\sim 30\%$ of the DM electron + positron flux at the sun's location originated from subhalos.

A summary of these results is presented in the top portion of Table 3.1. The predictions for MH and MH+SH scenarios are shown for the total $e^+ + e^-$ flux in figures 3.3 and 3.4 and for the positron fraction in figures 3.5 and 3.6. The value of χ^2 versus $M_{\rm DM}$ is shown in fig. 3.7, marginalizing over the background normalizations. For the minimum χ^2 point of the MH+SH model, the background electrons had to be reduced to 97% of their predicted values, while background positrons were rescaled to 137% of the GALPROP output.

The optimal boost factors of 90 for the main halo and 3800 for the subhalos are quite reasonable from the point of view of DM models that give Sommerfeld-enhanced cross sections [49]. We leave for future work the issue of detailed particle physics model building to match these and other features of the best-fitting models.

3.4.2 Constrained background

We performed a second analysis by taking the electron and positron backgrounds to be those predicted by GALPROP. In this case, although there is no good simultaneous fit to the combined PAMELA and Fermi data, we nevertheless find that SH contributions improve the fit. In rough agreement with ref. [62], we find that the

Table 3.1: Best fit scenarios. Top: when the background positron and electron spectra were allowed to vary by an overall factor; this corresponds to the best overall fit to the data. Bottom: using background that was fixed at GALPROP's normalization. In this case we used the best fit to Fermi, since the best overall fit gave values of electron + positron flux that were ruled out by the Fermi data. MH: main halo DM annihilation only. MH+SH: subhalo annihilation included. m_{DM} is the DM mass that gives the best fit and χ_i^2 are the chi squared fits to the respective experiments as described in eq. (3.6). $B_{\rm MH}$ and $B_{\rm SH}$ are the boost factors necessary for MH and SH annihilation cross sections, respectively. Note that the addition of a subhalo contribution greatly improves the best fit for both Fermi and PAMELA. The required DM mass is larger because of the energy loss suffered by electrons propagating to us from the galactic edge.

Freely-varying background						
	$M_{\rm DM}$	$\chi^2_{\rm Fermi}$	$\chi^2_{\rm PAMELA}$	$\chi^2_{\rm total}$	$B_{\rm MH}$	$B_{\rm SH}$
MH	0.85 TeV	15.5	18.7	34.3	90.3	–
MH+SH	1.2 TeV	2.3	14.2	16.5	92.8	3774
Fixed GALPROP background						
MH	1.0 TeV	8.2	144	152.2	110	–
MH+SH	2.2 TeV	2.1	175	177.1	146	1946

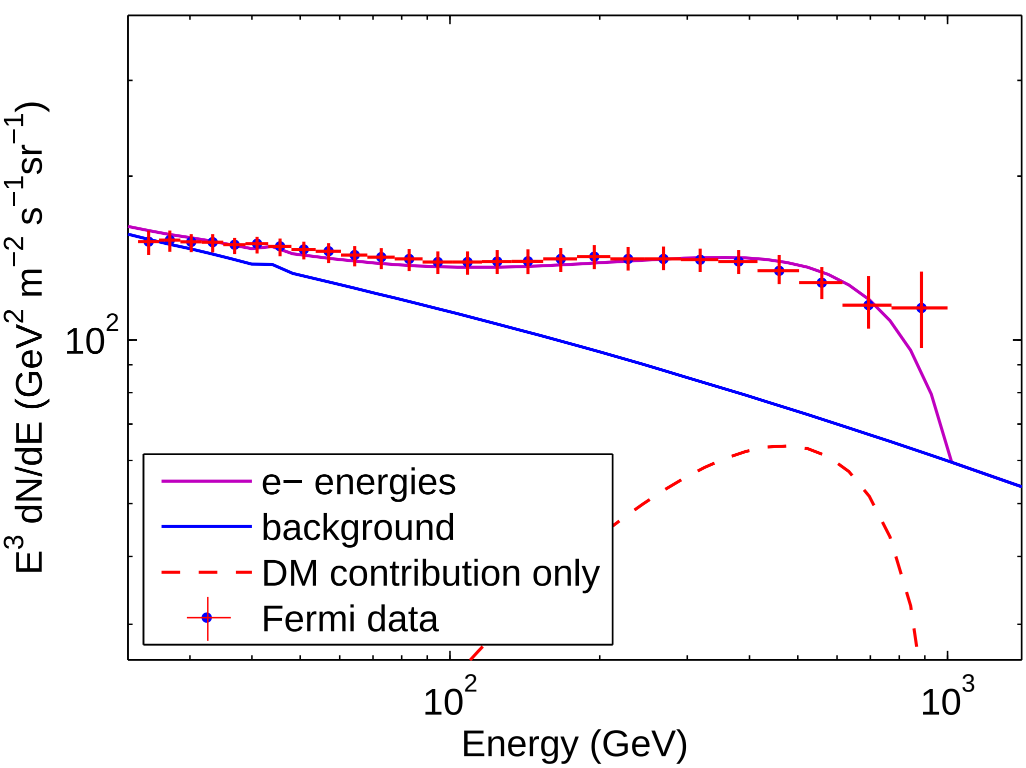

Figure 3.3: Fermi data and prediction for $e^+ + e^-$ flux of the best main-halo-only fit to Fermi and PAMELA data, with an unconstrained background.

PAMELA data require a boost factor several times higher than that needed to fit the Fermi data.

The plots of χ^2 versus $M_{\rm DM}$, for both the MH-only and MH+SH models, are shown respectively for the Fermi and PAMELA data in figures 3.8 and 3.9. It is striking that the best-fit DM mass becomes significantly larger and less constrained in the fit to the Fermi data including subhalos, fig. 3.9. The increase in the required DM mass is due to the energy lost by electrons and positrons during propagation from the edge of the diffusion zone to our position. The best fit to the Fermi data has $M_{\rm DM} = 2.2$ TeV ($\chi^2 = 2.05$) with SH+MH, compared with $M_{\rm DM} = 1$ TeV ($\chi^2 = 8.15$) in the MH only case. The required boost factors for these fits are $B_{\rm MH} = 146$ and $B_{\rm SH} = 1946$ for SH+MH, in contrast with $B_{\rm MH} = 110$ for MH only. The best fit cases for the $e^+ + e^-$ spectrum are shown in Figure 3.10 and the results are summarized in the bottom part

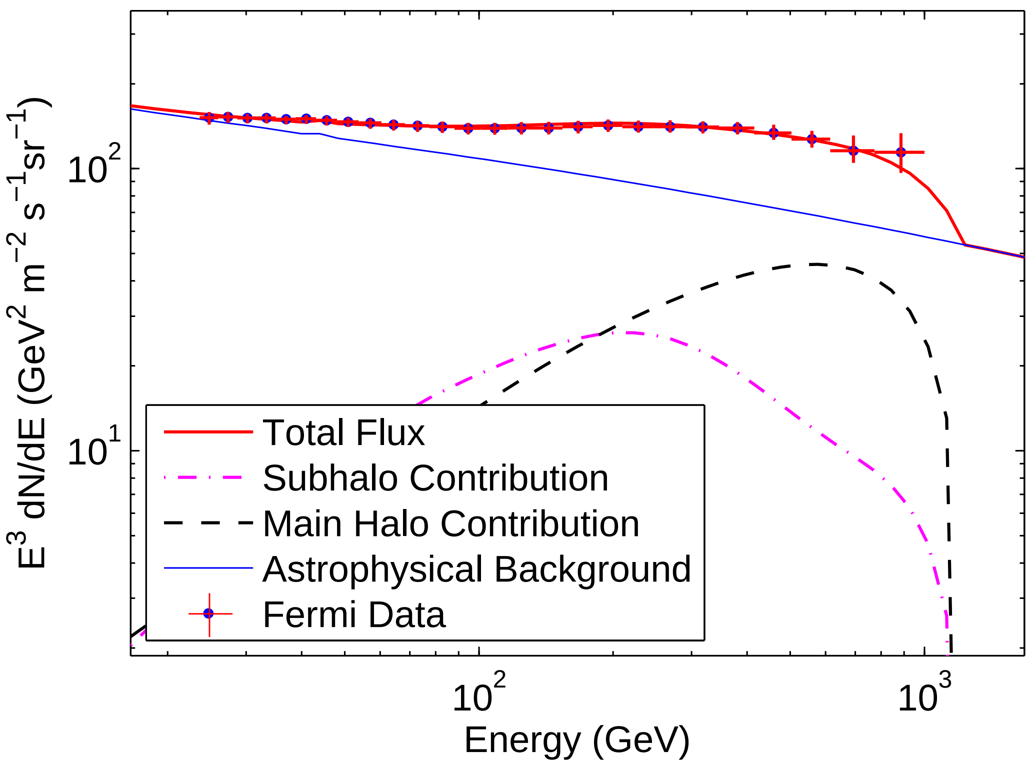

Figure 3.4: Same as fig. 3.3, but now including subhalo contributions to the lepton fluxes.

of Table 3.1. The corresponding positron fraction in each of these scenarios is shown in Figure 3.11.

The fit to PAMELA is also improved by the addition of SH positrons, but only at low DM mass, $M_{\rm DM} < 500$ GeV. However the best fit parameters for the PAMELA data by themselves lead to a prediction of the $e^+ + e^-$ $E^3 dN/dE$ spectrum that exceeds the Fermi data by more than 3σ, resulting in a $\chi^2 = 460$ fit to Fermi. The poor quality of this fit is evident in fig. 3.12.

3.4.3 Relative contributions of subhalos

It is interesting to quantify how much of the signal can be contributed by the subhalos relative to that coming from the main halo. We show the fraction of $e^+ + e^-$ pairs due to the subhalos, as a function of the DM mass, in fig. 3.13. For the best-fit

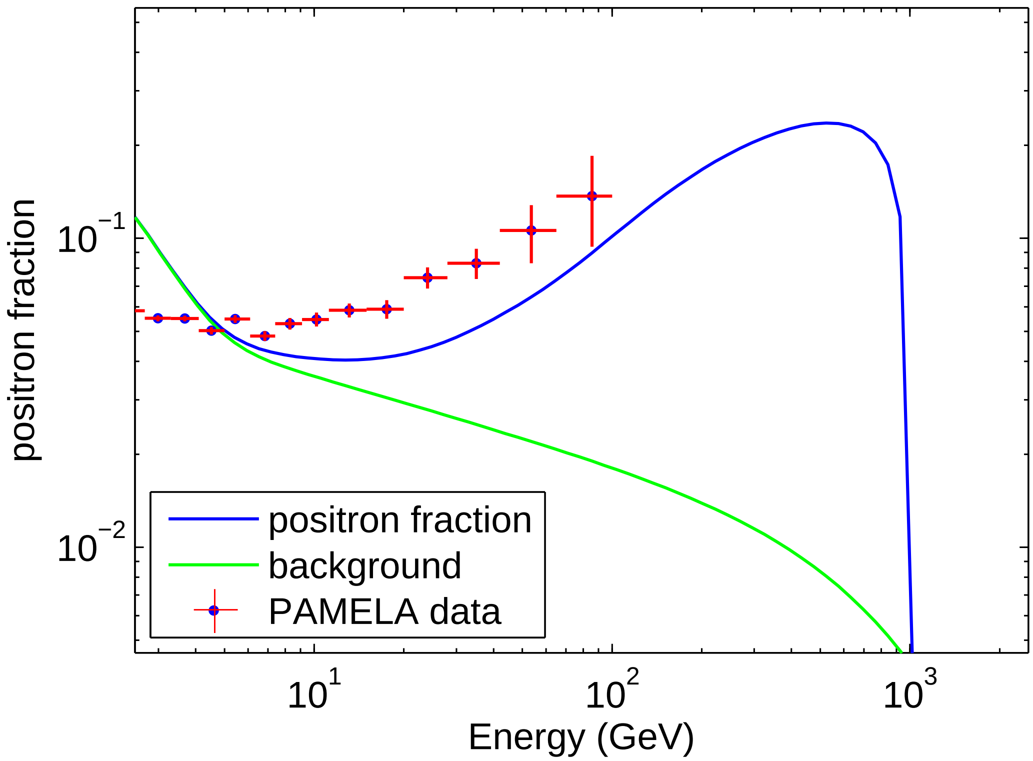

Figure 3.5: PAMELA data and predicted positron fraction of the best main-halo-only fit to Fermi and PAMELA data, with an unconstrained background.

values of the mass, this fraction is around 30%, but for larger values of $M_{\rm DM}$ (yet still giving reasonable fits) it rises to 60% or more. This may be helpful for weakening the constraints on the model from production of gamma rays by inverse Compton scattering [114, 115]. We hope to investigate this issue in the near future.

Another relevant issue is the hierarchy of contributions of subhalos relative to each other. One would like to know whether it was really necessary to add the contributions of all 20,000 subhalos, or if perhaps only the few closest ones dominate. Fig. 3.14 shows the distribution of subhalos contributing a given flux Φ (normalized to the contribution of the subhalo that gives the largest value $\Phi_{\rm max}$), weighted by the flux, and also the integral of this quantity. From the integral, we see that 50% of the total signal comes from subhalos whose individual intensities are less than 5% of the strongest one. Thus to get a quantitatively accurate estimate, it is necessary to

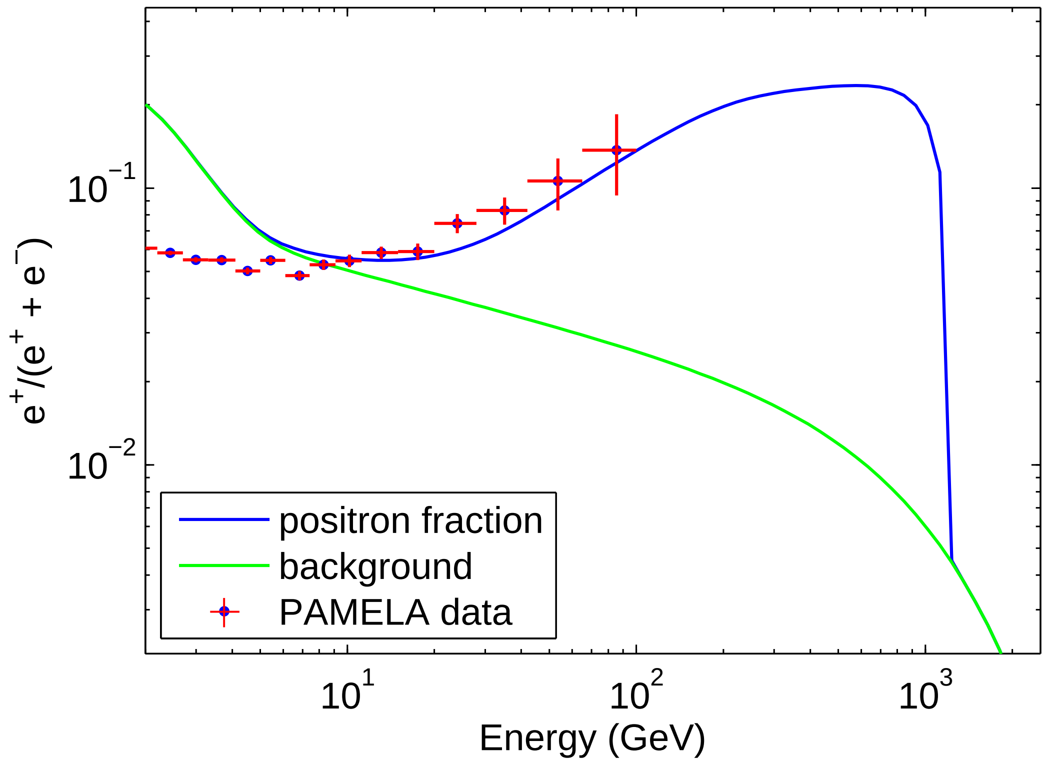

Figure 3.6: Same as fig. 3.5, but now including subhalo contributions to the lepton fluxes.

include the very numerous subhalos whose intensity is low. This also suggests that our computation is an underestimate, since we do not count the subhalos that are not resolved by the *Via Lactea II* simulation.

3.5 Conclusions

We have shown that the inclusion of electrons and positrons from the galactic subhalos can significantly alter the predictions from annihilating dark matter models. Using the *Via Lactea II* simulated data of the subhalo distribution around a Milky Way-like galaxy, we found that the contributions from substructure can give improved fits to the PAMELA and Fermi excess lepton data, and increase the value of the expected mass of the dark matter particle. A strong Sommerfeld boost coming from the low velocity dispersions of the subhalos, as well as the uncounted contributions

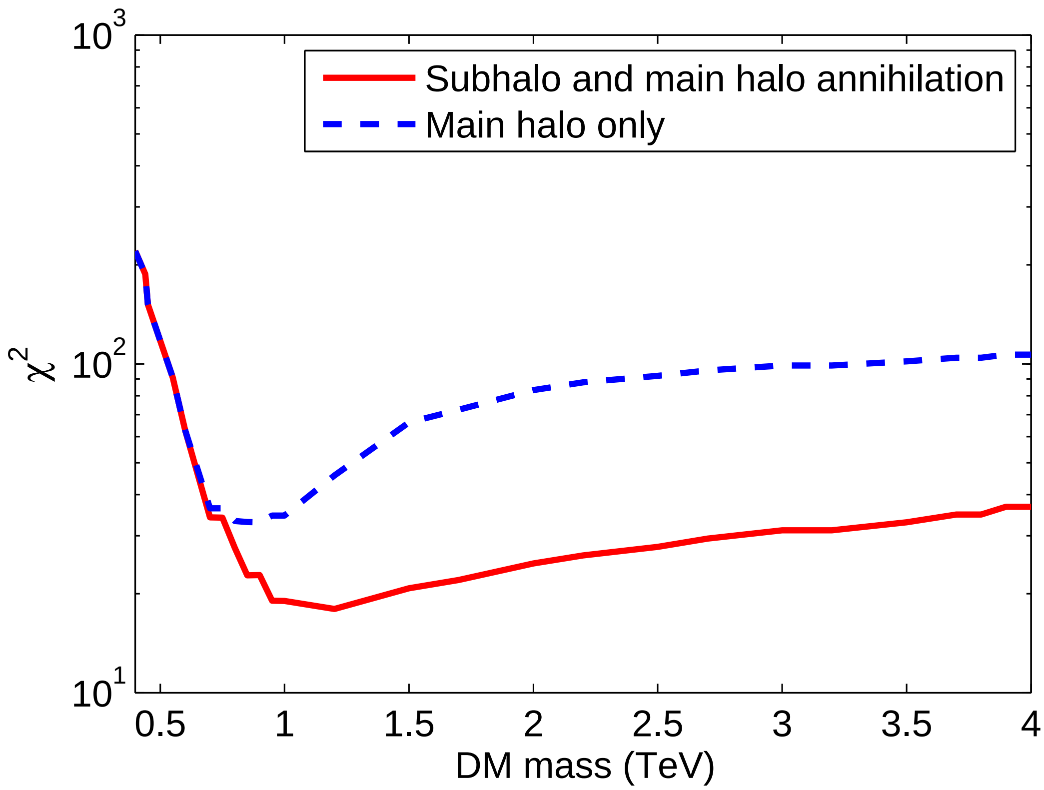

Figure 3.7: Combined χ^2 for the Fermi and PAMELA data as a function of the dark matter mass, for the unconstrained background. Dashed (blue) line: main halo DM annihilation only. Solid (red) line: subhalo and main halo contributions combined.

of subhalos unresolved by the *Via Lactea II* simulations, are possible sources for the boost factor necessary to obtain our best fits to the data. According to these fits a third or more of the electron cosmic rays from DM annihilation could come from subhalos outside of the visible Milky Way.

The next step for future work will be to see whether the reduction of the flux from the main halo can weaken Fermi constraints on annihilating DM models due to the inverse Compton gamma rays produced by the high-energy leptons [114, 115]. These constraints are sufficiently strong to rule out the DM interpretation of the Fermi lepton excess, under the usual assumption that all the e^+e^- pairs are produced in the main halo. The constraints are strongest from data near the galactic center. By shifting the production away from the center to the subhalos, the constraints should

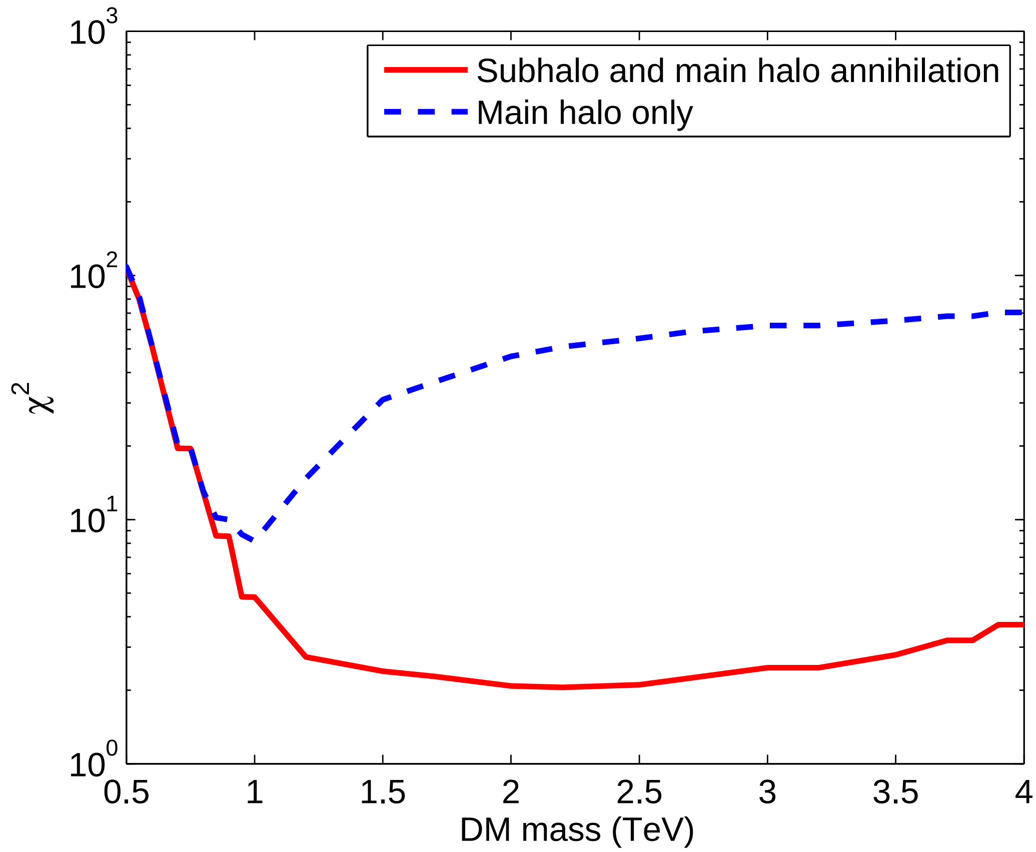

Figure 3.8: χ^2 versus M_{DM} for the Fermi $e^+{+}e^-$ data using the GALPROP constrained background. Dashed (blue) line: main halo only. Solid (red) line: subhalos plus main halo.

be weakened, but whether the effect is large enough to reinstate the DM interpretation of the Fermi lepton observations is a quantitative question. In addition, one should satisfy other protohalo constraints [126], extragalactic gamma background [127] and last scattering surface CMB constraints [128].

If it is possible for the scenario to pass these tests, it will be interesting to check whether specific particle physics models are able to give the average boost factors that we have treated as free parameters in this preliminary study.

As we were completing this work, ref. [129] appeared, which presents an analytical method for taking into account the effect of substructure on dark matter annihilation.

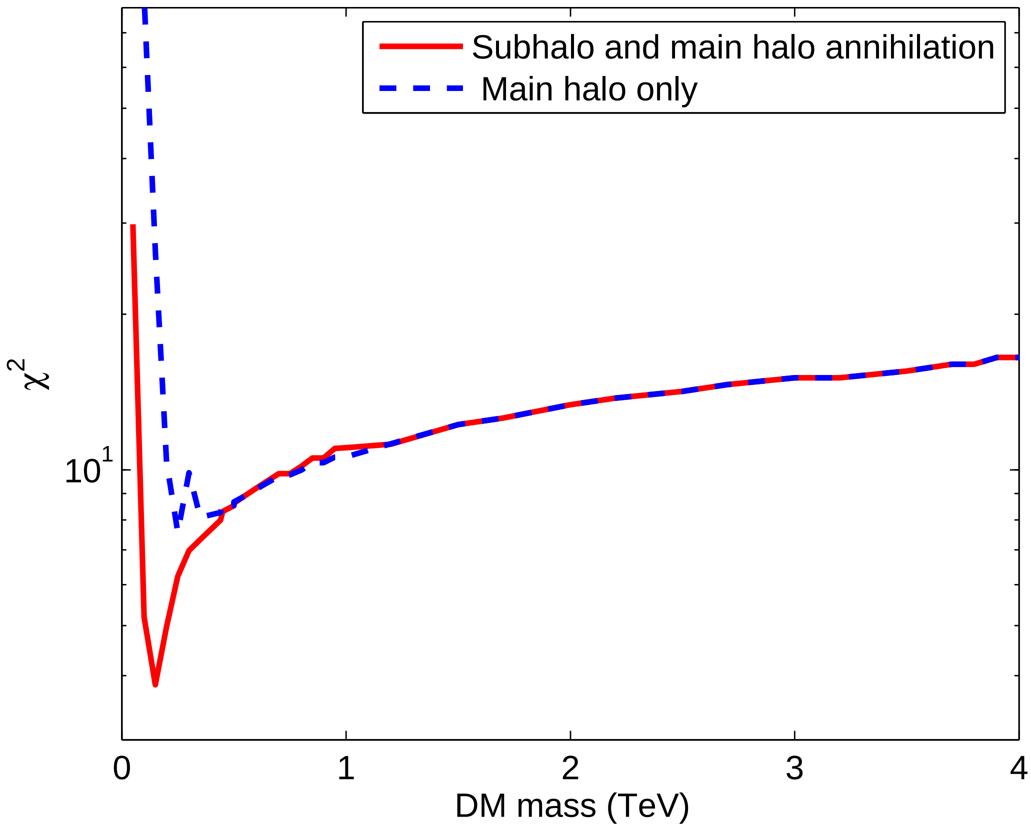

Figure 3.9: χ^2 versus $M_{\rm DM}$ for the Pamela positron fraction data, using the GALPROP constrained background. Dashed (blue) line: main halo only. Solid (red) line: subhalos plus main halo.

Their results were not directly compared with data, although they should provide similar results to our own given that their parametrization derives from results of N-body simulations.

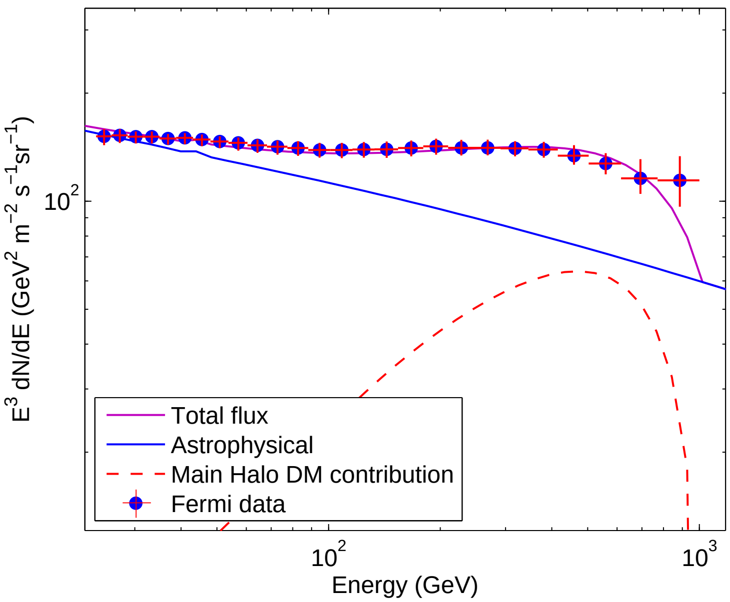

(a)

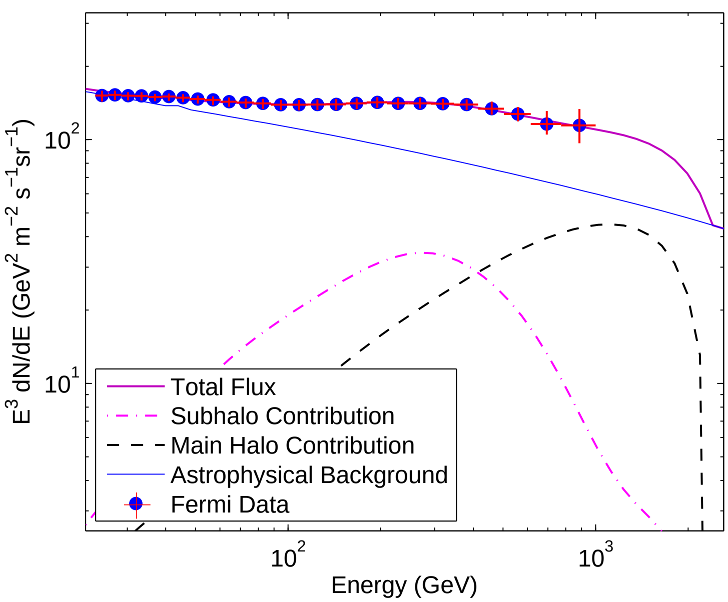

(b)

Figure 3.10: Best fits to Fermi data. a) Main halo only, $M_{\mathrm{DM}} = 1$ TeV, with a boost factor $B_{\mathrm{MH}} = 110$. b) Subhalos plus main halo, $M_{\mathrm{DM}} = 2.2$ TeV and $B_{\mathrm{MH}} = 146$, $B_{\mathrm{SH}} = 4825$.

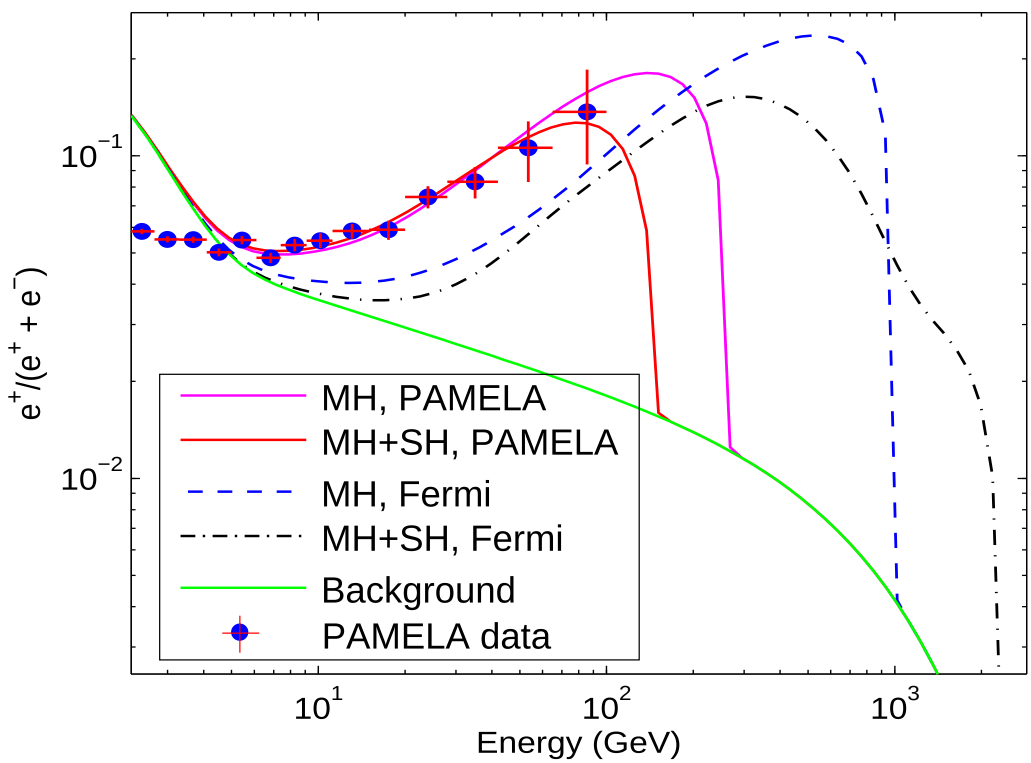

Figure 3.11: Positron fraction for four of the best fit scenarios with constrained backgrounds. Top (solid) lines correspond to fits to PAMELA data only. Uppermost (magenta): MH only; m_{DM} = 250 GeV, S_{MH} = 225. Lower (red): MH+SH; m_{DM} = 150 GeV, S_{MH} = 9.3, S_{SH} = 509. Bottom (dashed) lines correspond to the best fits of these scenarios to the Fermi data. Upper dashed (blue): MH only; m_{DM} = 1 TeV, S_{MH} = 110. Lower dot-dashed (black): MH+SH; m_{DM} = 2.2 TeV, S_{MH} = 146, S_{SH} = 4825. Although the former set provide a better χ^2, they predict a total $e^+ + e^-$ flux that conflicts with the Fermi data by at least 3σ (see figure 3.12).

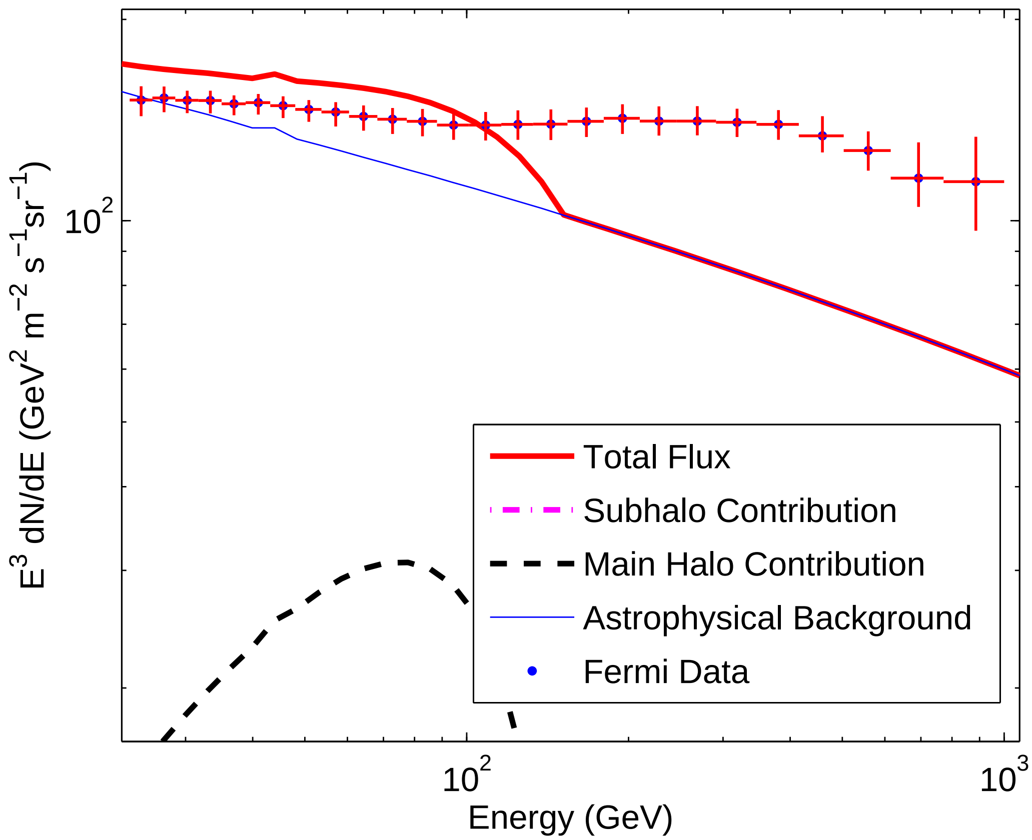

Figure 3.12: e^+e^- curve for best fit to PAMELA data only. $m_{DM} = 150$ GeV, $S_{MH} = 9.3$, $S_{SH} = 509$. Although the high energy tail could be compensated by other sources (*e.g.*, pulsars), the fact that the model exceeds the data points at low energy leads us to disfavour this model. Note that the subhalo contribution is too small to be seen in this figure.

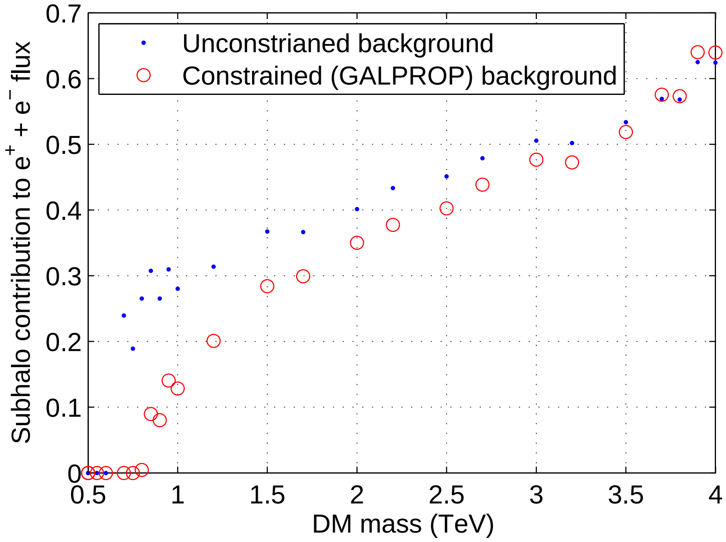

Figure 3.13: Proportion of the total flux of $e^+ + e^-$ originating from subhalos as opposed to the main halo, as observed 8.5 kpc from the galactic center (the position of the solar system) in order to obtain a best fit to the Fermi data. Each point represents an individual simulation.

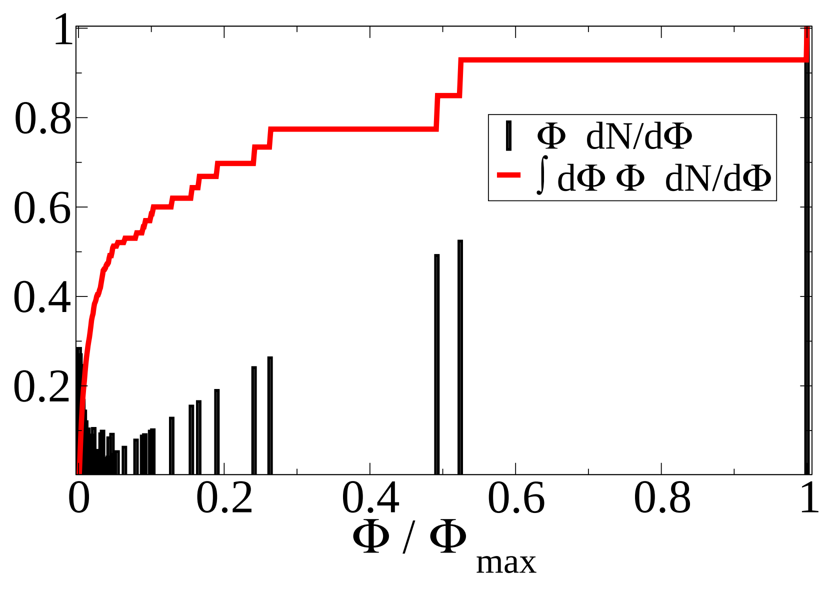

Figure 3.14: Vertical bars (black): $\Phi \, dN/\mathrm{d}\Phi$, the distribution of subhalos contributing a given flux at the edge of the diffusion zone, weighted by the flux. Continuous curve (red): integral of $\Phi \, dN/\mathrm{d}\Phi$.

Bridge

We have shown that including the subhalo contribution to the positron flux of cosmic rays due to dark matter annihilation can give a better fit to the PAMELA and Fermi $e^{\pm}$ data. However, the key constraints come from different observations: the gamma ray sky observed by the Fermi-LAT experiment. In the following chapter, our aim will be to construct models of the gamma ray sky that would be observed in the dark matter halo + subhalos scenario of the previous chapter, and to confront these models with the Fermi-LAT diffuse gamma ray data.

Chapter 4

Overcoming Gamma Ray Constraints with Annihilating Dark Matter in Milky Way Subhalos

Work published with Wei Xue and James M. Cline
in Physical Review D82 (2010) 123519

Abstract

We reconsider Sommerfeld-enhanced annihilation of dark matter (DM) into leptons to explain PAMELA and Fermi electron and positron observations, in light of possible new effects from substructure. There is strong tension between getting a large enough lepton signal while respecting constraints on the fluxes of associated gamma rays; we show how DM annihilations within subhalos can get around these constraints. Specifically, if most of the observed lepton excess comes from annihilations in a nearby (within 2 kpc) subhalo along a line of sight toward the galactic center, it is possible to match both the lepton and gamma ray observations. We demonstrate that this can be achieved in a simple class of particle physics models in which the DM annihilates via a hidden leptophilic U(1) vector boson, with explicitly computed Sommerfeld enhancement factors. Gamma ray constraints on the main halo annihilations (and CMB constraints from the era of decoupling) require the annihilating component of the DM to be subdominant, of order $10^{-2} - 10^{-3}$ of the total DM density.

4.1 Introduction

Nongravitational signals of Dark Matter (DM) have been sought after for some time now by the astrophysical and particle physics communities. At the same time results from the Payload for Antimatter Matter Exploration and Light-nuclei Astrophysics (PAMELA) experiment and from the Fermi space telescope suggest a local excess positron fraction $e^+/(e^+ + e^-)$ at energies above 10 GeV as well as an excess of $e^+ + e^-$ peaking around 500 GeV. Standard cosmic ray propagation models do not account for these excesses. An attractive explanation is that a DM WIMP (weakly interacting massive particle) is present in our galaxy at large enough concentrations to self-annihilate into standard model leptons. A TeV-scale WIMP annihilating to electron-positron pairs could produce such signals. In order to be consistent with the observed relic abundance of DM, the annihilation cross-section $\langle \sigma v \rangle_0 \sim 3 \times 10^{-26}$ cm^3 s^{-1} would have to be enhanced by a factor of order 100, for example by a velocity-dependent Sommerfeld enhancement.

Many authors [60, 49, 61, 62, 63, 64, 65, 66, 67, 68] have explored this possibility, and have constrained the allowable mass versus boost factor parameter space. However these papers assume that the dominant source of indirect signals is from annihilations in the main DM halo. In a previous work [2] we considered the possibility of adding the effects of dark matter substructure to the theoretical model and we found examples where annihilations in subhalos could provide a significant fraction of the observed lepton excesses. We showed that one could find a better overall fit to the electron-positron data from the Fermi and PAMELA experiments, and we suggested that gamma ray constraints which are now putting considerable pressure on these models could be alleviated. Our purpose in the present work was to ascertain whether this is indeed the case.

The constraints mentioned come from recent gamma ray observations of the galaxy and from Cosmic Microwave Background (CMB) measurements. As high energy electron-positron pairs are produced and diffuse throughout the galaxy, they will emit final-state radiation as well as scatter on the ambient photon field, giving rise to $\sim$ 1-100 GeV gamma rays that should be detectable. Given the large expected concentrations of both DM and radiation near the galactic center (GC), gamma rays from inverse Compton scattering (ICS) near the GC are particularly constraining. The Fermi Large Area Telescope (LAT) is specifically designed to detect gamma rays in this range, and its latest results have been used to rule out large regions of parameter space for annihilating WIMP models [64, 114, 130, 131].

However in this chapter we will show that if a sizeable proportion of the leptons from DM annihilation originate from nearby subhalos, the constraints from GC gamma rays can be relieved. Final-state (bremsstrahlung) radiation from subhalos has been examined by other authors [85, 86, 87, 88, 4, 67, 132], and ref. [90] has studied the $e^+ + e^-$ spectrum from a nearby subhalo. In this follow-up work we extend our previous findings to a prediction of the gamma ray spectrum including a full calculation of ICS radiation in the galaxy, which we compare to the full-sky data from the Fermi LAT. We include the expected contribution to the gamma ray background coming from background electrons and positrons. Using a fully-numerical approach, we find that there is less room for new contributions from the annihilation products of the DM, making the constraints on the DM models more severe. This is a serious issue even for less cuspy and cored DM profiles, that have been shown to satisfy the constraints in previous semi-analytic treatments which ignored the background gamma ray fluxes.

In the previous chapters we focused on the contributions of distant subhalos to the flux of leptons at Earth. Even though these new contributions can improve the fit to the lepton data alone, here we show that they do not soften the gamma ray constraints sufficiently to be viable. Instead, we focus on the possibility that an accidentally nearby subhalo could provide the bulk of the leptonic flux. The associated gamma rays would be sufficiently hidden by strong backgrounds if this subhalo happened to lie between us and the galactic center. The effects of nearby subhalos have been previously considered by ref. [89], but only allowing for purely astrophysical boost factors, due to the density of the subhalos. Here we find that velocity-dependent Sommerfeld enhancement is crucial for obtaining a positive outcome. It is precisely because of the larger boost factor available within subhalos (which have orders of magnitude smaller velocity dispersion) relative to the main halo that we are able to soften the gamma ray constraint due to the main halo near the GC, yet have a large enough lepton signal from a nearby subhalo. In addition, we must assume that the leptophilic component of the DM responsible for these processes is subdominant to the main inert (for our purposes) component, in order to sufficiently reduce the effective boost factor for annihilations in the main halo [131]. This gives rise to the interesting possibility that different kinds of DM are responsible for the cosmic ray anomalies than those which might manifest themselves in direct detection experiments.

Using a modified version of the cosmic ray propagation code GALPROP and the data from the recent *Via Lactea II* simulation of dark matter evolution and collapse in a Milky Way-sized galaxy, we modelled the two-dimensional axisymmetric distribution of electrons and positrons in the galaxy. These results were combined with simulated interstellar radiation field (ISRF) data in order to compute a realistic skymap of the gamma ray spectrum expected from DM annihilation in the Galaxy, which was in turn compared with a year's worth of diffuse gamma ray observation from the Fermi LAT.

We start with a summary of the cosmic ray model and results of our previous work in Section 4.2, before discussing the relevant ICS and gamma ray physics in Section 4.3. In Section 4.4 we describe our methodology, and present model-independent fits to the data in several scenarios for the distribution of subhalos and the halo profiles. In particular, we show that an accidentally nearby subhalo can provide a promising loophole to the gamma ray constraints on cuspy profiles. We also predict the gamma ray flux from the subhalo, which could provide a test of the model if future measurements and understanding of backgrounds are improved. In section 4.5 we then demonstrate that the boost factors required for this scenario can be explicitly realized in a simple class of hidden sector particle physics models. We conclude with a discussion of the overall viability of this picture in section 4.6.

4.2 Cosmic Ray Propagation

Inside the galactic diffusion zone, particles and nuclei propagate according to the diffusion-loss equation [116], which applies to electrons and positrons as follows:[1]

$$\begin{aligned}\frac{\mathrm{d}}{\mathrm{d}t}\psi_{e^\pm}(\mathbf{x},\mathbf{p},t) &= Q_{e^\pm}(\mathbf{x},E) + \nabla\cdot\left(D(E)\nabla\psi_{e^\pm}(\mathbf{x},\mathbf{p},t)\right)\\ &+ \frac{\partial}{\partial E}\left[b(\mathbf{x},E)\psi_{\pm}(\mathbf{x},\mathbf{p},t)\right] \ .\end{aligned} \tag{4.1}$$

$\psi_{e^\pm}(\mathbf{x},\mathbf{p},t)$ denotes the particle number density per unit momentum $|\mathbf{p}|$, Q represents the source function, $D(E)$ is the spatial diffusion coefficient and $b(\mathbf{x},E)$ is the energy loss coefficient. We seek the steady-state solution of equation (4.1): $\mathrm{d}\psi_{e^\pm}(\mathbf{x},\mathbf{p},t)/\mathrm{d}t = 0$.

Since (4.1) is linear, the leptons from DM annihilation travel independently in the astrophysical background. The source $Q_{e^\pm}$ comes from DM annihilation which depends on the particle physics and the local density of the dark matter:

$$Q_{e^\pm} = \frac{1}{2}\left(\frac{\rho(\mathbf{x})}{M}\right)^2\langle\sigma v\rangle\frac{\mathrm{d}N_{e^\pm}}{\mathrm{d}E} = \frac{n_{DM}^2}{2}BF\langle\sigma v\rangle_0\frac{\mathrm{d}N_{e^\pm}}{\mathrm{d}E}. \ , \tag{4.2}$$

where the prefactor 1/2 is a symmetry factor for self-annihilation, $n_{DM}(\mathbf{x},E)$ is the DM energy density, $\langle\sigma v\rangle_0 = 3\times10^{-26}$ cm^3 s^{-1} is the benchmark value for standard cosmology to explain the relic density of DM, and $\mathrm{d}N_{e^\pm}/\mathrm{d}E$ is the energy spectrum of the annihilation products. Neglecting the effect of soft photons, the spectrum can be approximated by the simple form $\mathrm{d}N_{e^\pm}/\mathrm{d}E = 2M_{DM}^{-1}\Theta(M_{DM}-E)$, where $\Theta(x)$ is the usual Heaviside step function, and the factor 2 arises because the final state has two electrons or two positrons. The latter has the correct qualitative shape, and is

[1] The full transport equation also includes the effects of convection and diffusive reacceleration, which are mainly important for the propagation of heavier species. Here we leave these terms out for clarity, although they were included in our full calculations with GALPROP. These are important for determining the abundance of secondary electrons and positrons, which come from spallation and decay of various species.

easier to implement in GALPROP than would be a more exact spectrum. BF denotes the boost factor due to Sommerfeld enhancement, originating from a nonperturbative $\sim 1/v$ correction due to the slow ($v/c < \alpha$) motion of the DM particles.

To simplify our analysis, we take the boost factor BF to be constant throughout the main halo, and tune it to provide the best possible fit to available electron and positron data. Since the Sommerfeld effect depends strongly on velocity, typical subhalos, which have a much smaller velocity dispersion, have a much higher BF, and we treat it as an additional free parameter. Although each subhalo has different values of BF, we represent the subhalo BF by a single average value in this first part of our analysis, where the BFs are treated as being uncorrelated and best fit values are sought. This is not a limitation in the case we will eventually focus upon, namely domination of the excess lepton signal by a single nearby subhalo. A further complication is that in fact BF has a radial dependence within each halo, because the velocity dispersion is a function of r, which has been fitted by many-body simulations such as *Via Lactea II* [4]. We will take this into account in section 4.5.1 by averaging BF over the phase space of DM in the halos, in order to make contact with the results obtained in this model-independent part of our analysis.

The spatial diffusion coefficient can be parametrized as follows [117]:

$$D(E) = D_0 \left(\frac{E}{4 \text{ GeV}} \right)^{\delta} \tag{4.3}$$

Two widely-used approaches exist for solving the diffusion equation in the Galaxy: semianalytic and fully numerical. We chose the latter for Galaxy-scale propagation, in part because a numerical approach allows for better control over the spatial dependence of the astrophysical input, such as energy loss due to inverse Compton scattering. GALPROP 50.1p [73] is a publicly available software package that solves Eq. (4.1) with an implicit-in-time 2D or 3D Crank-Nicholson scheme. In 2D mode, it provides a (r, z) map in cylindrical coordinates of the number density of each species within the Galactic diffusion zone. To constrain the diffusion parameters, the ratio of measured secondary-to-primary species such as B/C or sub-Fe/Fe can be simulated and fit to observations. This was done to a very high degree of accuracy in Ref. [117]. We used results from their best fits: $D_0 = 6.04 \times 10^{28}\,\mathrm{cm^2 s^{-1}} (0.19\,\mathrm{kpc^2/Myr})$, and $\delta = 0.41$.

The full energy loss rate is due to synchrotron radiation and inverse Compton scattering:

$$b(x,E) = -\frac{\mathrm{d}E_e}{\mathrm{d}t} = \frac{32\pi\alpha_{em}}{3m_e^4} E_e^2 \left[u_B + \sum_{i=1}^{3} u_{\gamma i} \cdot R_i(E_e) \right] . \tag{4.4}$$

α_{em} is the fine structure constant and $u_B = B^2/2$ is the energy density of the galactic magnetic field, for which we used the standard parametrization:

$$B(r,z) \simeq 11\mu G \cdot \exp\left(-\frac{r}{10\,\mathrm{kpc}} - \frac{|z|}{2\,\mathrm{kpc}} \right) . \tag{4.5}$$

$u_{\gamma i}$ are the energy densities of the three main components of the interstellar radiation field (ISRF): CMB radiation, thermal radiation from dust and starlight, which lie mainly in the microwave, infrared and optical regions of the electromagnetic spectrum, respectively. GALPROP uses position-dependent maps of ISRF compiled by [123], rather than using a constant energy-loss coefficient computed from a local average. The latter approach (explained in section 3 of [133]) is commonly used in the semi-analytic model. While it is indeed quite accurate when dealing with electrons from a smooth Galaxy-wide distribution of dark matter, it is an approximation that is less precise when considering the propagation into the Galaxy of electrons from DM subhalos outside of the diffusion zone. We will nonetheless make use of the semi-analytic method in Section 4.4.2, when only local propagation will be relevant. The position dependence of the ISRF in the Galaxy is presented in Figure 4.1. Further details will be discussed in section 4.3.2.

4.2.1 Via Lactea II and GALPROP

We assumed that the DM was composed of a single Dirac fermion χ of mass M_{DM} annihilating through the channel $\chi\chi \to BB$, followed by the decay $B \to e^+e^-$, where B is some dark sector gauge boson which could also be responsible for the Sommerfeld enhancement. We considered two astrophysical models for the DM distribution: a

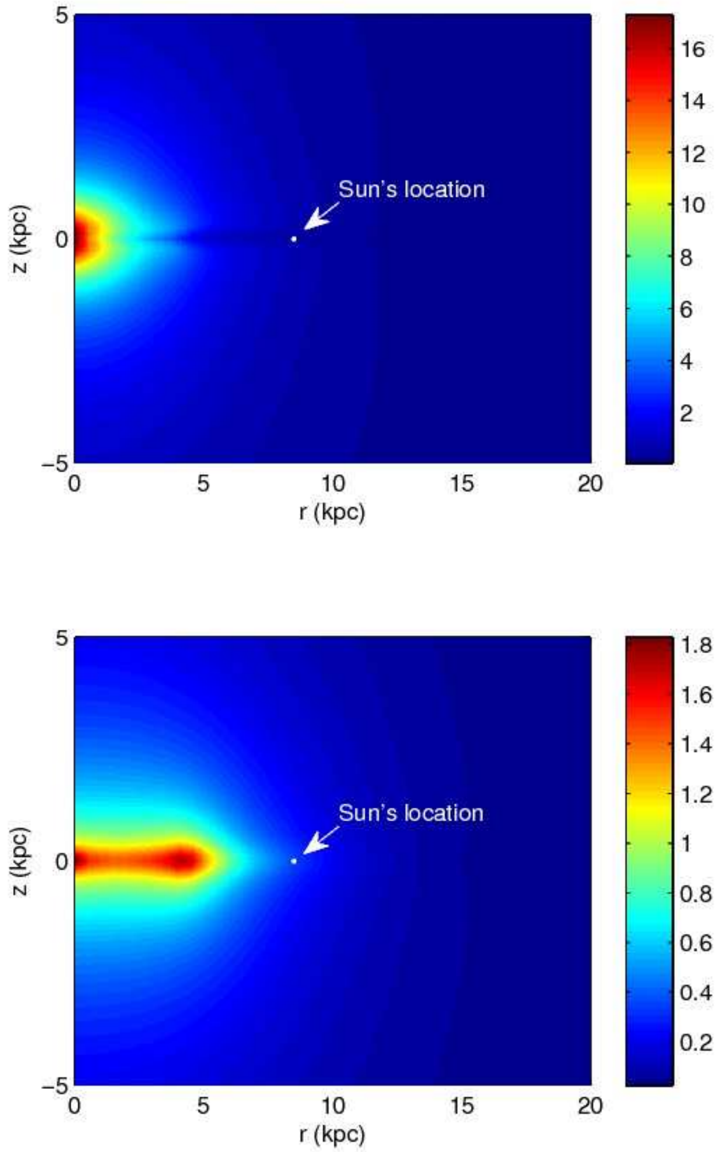

Figure 4.1: Simulated energy density distribution of the interstellar radiation field (ISRF) within the Milky Way by [123], integrated over energies. Top: starlight component. Bottom: IR component, from dust. The CMB component is of course uniform throughout the galaxy. Color scale is $log(density)$ in arbitrary units.

main halo-only (MH) scenario, in which only a large, spherical halo contributed annihilation products; and a subhalo (MH+SH) scenario, where the overdensities formed by DM substructure were responsible for extra annihilation of DM into electrons and positrons. In both cases, we used a spherically symmetric Einasto profile for the DM density distribution:

$$\rho_{\rm Ein}(r) = \rho_s \exp\left\{-\frac{2}{\alpha}\left[\left(\frac{r}{r_s}\right)^{\alpha} - 1\right]\right\} \ . \tag{4.6}$$

r is the radial coordinate from the center of the halo, ρ_s is the density at $r = r_s$, the distance at which the slope $\rho'/\rho = -2$. These parameters are simply related to the radius and rotational velocity of a given subhalo as explained in Ref. [4]. The shape parameter α can be read off from curve-fitting the distributions from N-body simulations such as [18, 17]. It is generally taken to be around $\alpha \simeq 0.17$. We took $r_s = 25$ kpc for the main galactic halo, with a local dark matter density $\rho_\odot = 0.37$ GeV cm^{-3} in agreement with *Via Lactea II* and with other recent estimates, *e.g.,* [134]. It should be noted that many authors use the convention $\rho_\odot = 0.3$ GeV cm^{-3}. This leads to a factor of $(0.3/0.37)^2 = 0.66$ difference in the constraints on the annihilation cross sections, but it is of no consequence when it comes to excluding models, since constraints come from the ratio of gamma rays-to-lepton fluxes, which both scale linearly with $\rho_\odot^2\langle\sigma v\rangle$.

It has been argued that direct observations of rotation velocities in the Milky Way are consistent with cored DM profiles (see for example ref. [19]). Two such examples are the isothermal and Burkert [135] ansatzes. The Burkert profile has been fitted to the rotation curves of galaxies other than our own, but we are not aware of references which attempt to fit the Milky Way. To allow for the alternative possibility of a cored main halo, we will therefore restrict our attention to the isothermal profile

$$\rho_{\rm iso}(r) = \frac{\rho_s}{1 + (r/r_s)^2} \tag{4.7}$$

adopting the values $r_s = 3.2$ kpc and $\rho_s = 3.0$ GeV/cm^3 similar to those used by ref. [114]. These values are motivated by the constraint on the observed solar density $\rho_\odot$

(which we take to be somewhat higher than in [114]) and on the mass of the Galaxy with 50 kpc as determined from circular velocity measurements. However for the subhalos we will in all cases assume the Einasto form that is suggested by *Via Lactea II*.

Via Lactea II [18] was a billion-particle simulation that tracked the evolution and collapse of 10^9 particles over the history of a Milky Way-sized structure. Data about the main galactic halo and the 20,047 largest subhalos that the particles (each taken to have mass 4,100 $M_\odot$) merged into over the course of the simulation are available to the public. While the visible galaxy is only 40 kpc across, these subhalos extend as far out as 4000 kpc from the GC. We used the *Via Lactea II* subhalo data as a model for substructure sourcing electrons and positrons (from DM annihilation) at the boundary of the GALPROP diffusion zone, with an overall tunable boost factor for the subhalo annihilation rate. In addition to a larger Sommerfeld enhancement from smaller velocity dispersions within each subhalo, we expect sub-substructure unresolvable from numerical simulations to give rise to further enhancement of the annihilation cross-section. Recent estimates [67] show that such sub-subhalos alone could increase annihilation rates by as much as a factor of 10.

Electrons from an extragalactic source have a very particular density profile. While the annihilation products from the main halo follow a roughly symmetric distribution about the GC, SH electrons sourced from the diffusion zone boundary tend to form a diffuse "shell" near the edge of the diffusion zone, as illustrated in Fig. 4.2. Ambient radiation prevents high-energy particles from reaching the GC, trapping them near the edge of the Galaxy. The large number of subhalos combined with a large boost factor can allow some particles to make their way to earth, albeit with a fraction of their initial energy.

We compared the best-fit combination of DM mass and boost factor for the MH scenario with the best fits for the MH+SH scenario in [2]. The results are summarized in table 4.1: a much better fit could be obtained by including subhalos and a dark matter particle with $M_{DM} = 2.2$ TeV, rather than the standard MH-only $M_{DM} = 1$ TeV. Of course, the fits are further improved by allowing the normalizations of the background electrons and positrons to be additional free parameters, denoted as the "freely varying background," as opposed to the standard backgrounds resulting from GALPROP simulations which include the effects of heavier nuclear species. Assuming this extra freedom has been advocated or used by numerous authors [64, 114, 63, 115]. In table 4.1 we also show the fit we obtain in the present analysis for the main-halo-only case with an isothermal profile and fixed background. It is significantly worse than the corresponding one for an Einasto profile.

4.2.2 Annihilation channels

While we have mostly focused on the 4e final state, there is no reason for other, heavier particles not to be produced if the mass of the intermediate gauge boson is large enough. Since the amount of Sommerfeld enhancement ultimately depends on this mass, it is important to include the decays to muons and pions. The possible final states are all the four-particle combinations of $2e$, 2μ and 2π. The muon and pion spectra are given by Ref. [136], whose authors were kind enough to provide us with the appropriate GALPROP implementation.

The branching ratios are given by $r_i = f_i / \sum f_i$, where the f_i are given at low energies by

$$f_i = \sqrt{\mu^2 - 4m_i^2} \begin{cases} 4(\mu^2 + 2m_i^2), & i = e, \mu \\ (\mu^2 - 4m_i^2), & i = \pi \end{cases} \tag{4.8}$$

In each f_i, the square root factor comes from the phase space, while the rest is from the squared matrix element for the decay. Below threshold, f_i is defined to be zero. The scalar treatment for the pion breaks down at a few hundred GeV, as μ approaches the ρ meson mass. Above this, collider data must be used. The electrons produced from the final decay of the μ's and π's peak at a lower energy than in the pure $4e$ final state, thus requiring a slightly higher mass of $M_{DM} = 1.2$ TeV in order to fit the Fermi and PAMELA data. This is much smaller than the well-known $M_{DM} \simeq 2.2$ TeV best fit in the pure-muon final state [64, 115, 63] because of the large fraction of gauge bosons still decaying directly to high-energy electrons. These results are also shown in Table 4.1.

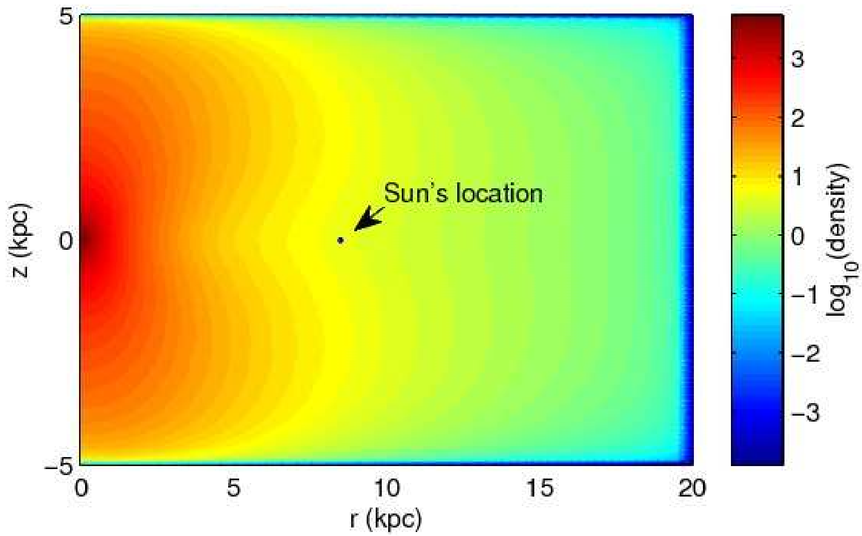

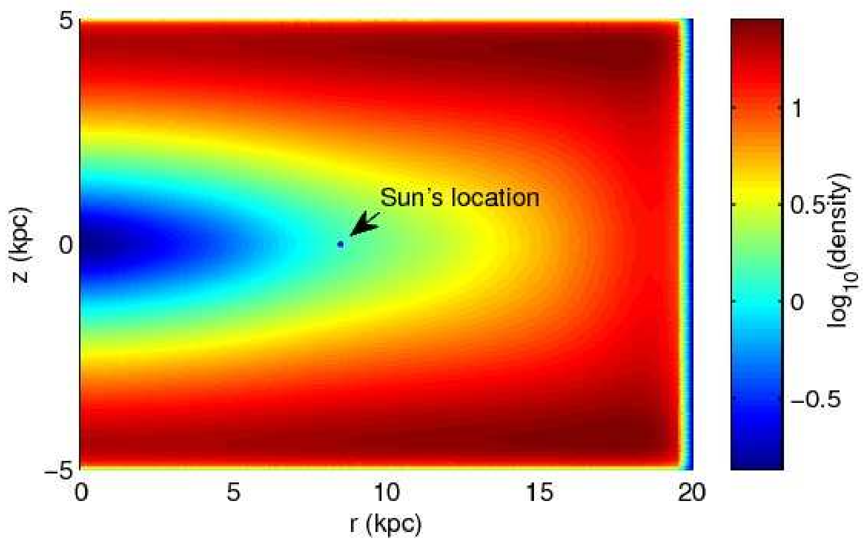

Figure 4.2: Simulated steady-state distribution of electrons and positrons from DM annihilation within the Milky Way diffusion zone. The galactic center is located at $z = 0$, $r = 0$; red corresponds to high densities, blue to low densities. Top: leptons from the main halo only. Bottom: leptons from the subhalos only, sourced from the diffusion zone boundary. Note that the scales are different: the peak main halo density (at the GC) is about 200 times larger than the peak subhalo density (near the edge of the diffusion zone)

Freely-varying background (Einasto)						
	$M_{\rm DM}$ (TeV)	$\chi^2_{\rm Fermi}$	$\chi^2_{\rm PAMELA}$	$\chi^2_{\rm total}$	$B_{\rm MH}$	$B_{\rm SH}$
MH ($4e$)	0.85	15.5	18.7	34.3	90.3	–
MH+SH	1.2	2.3	14.2	16.5	92.8	3774
Fixed GALPROP background (Einasto)						
MH ($4e$)	1.0	8.2	144	152	110	–
MH+SH	2.2	2.1	175	177	146	1946
MH (e, μ, π)	1.2	3.8	109	112	118	–
Isothermal profile (fixed background)						
MH ($4e$)	1.0	9.1	186	195	113	–
MH (e, μ, π)	1.2	3.0	151	154	119	–

Table 4.1: First four rows: best fit results from [2], assuming Einasto profile. By varying the boost factors of the main halo and faraway subhalos separately, we found that the fit to the PAMELA and Fermi data from MH annihilations alone could be improved by inclusion of SH annihilations as shown. Last two rows: new fit for isothermal profile ($r_s = 3.2$ kpc, $\rho_s = 3.0$ GeV/cm^3), main-halo-only scenario from this work, using the fixed GALPROP background, and same parameters as in [2]. We assume the annilation to the 4e final state, except in the cases "MH (e, μ, π)" which indicates the the process $\chi\chi \to BB \to 4\ell$, where ℓ stands for $e^\pm$, $\mu^\pm$ or $\pi^\pm$, with branching ratios $r_e = r_\mu = 0.45$ and $r_\pi = 0.1$ as explained in Section 4.2.2.

4.3 Gamma Ray Computation from Inverse Compton Scattering and Bremsstrahlung

4.3.1 "Prompt" gamma ray emission (bremsstrahlung)

Prompt gamma ray emission appears in the final stage of DM annihilation, softening the lepton spectrum. The flux can be divided into main halo and subhalo parts:

$$\frac{\mathrm{d}\Phi}{\mathrm{d}E_\gamma \mathrm{d}\Omega} = \frac{\mathrm{d}\Phi_{\rm main}}{\mathrm{d}E_\gamma \mathrm{d}\Omega} + \frac{\mathrm{d}\Phi_{\rm sub}}{\mathrm{d}E_\gamma \mathrm{d}\Omega} \ . \tag{4.9}$$

The astrophysical and particle physics dependences of each flux can be factorized as

$$\frac{\mathrm{d}\Phi_{\rm main}}{\mathrm{d}E_\gamma \mathrm{d}\Omega} = \frac{1}{2}\frac{\langle\sigma v\rangle}{4\pi} r_\odot \frac{\rho_\odot^2}{m_\chi^2}\frac{\mathrm{d}N}{\mathrm{d}E_\gamma}\bar{J}_{main} \tag{4.10}$$

and

$$\frac{\mathrm{d}\Phi_{\rm sub}}{\mathrm{d}E_\gamma \mathrm{d}\Omega} = \frac{1}{2}\langle\sigma v\rangle \frac{\mathrm{d}N}{\mathrm{d}E_\gamma}\bar{J}_{sub}. \tag{4.11}$$

In each case, the $\bar{J}_i$ factor depends only upon astrophysical inputs. The main halo J factor is defined as a line of sight (l.o.s.) integral of flux at each pixel:

$$\bar{J}_{\text{main}} = \frac{1}{\Delta\Omega} \int_{\Delta\Omega} \mathrm{d}\Omega \int_{\text{l.o.s.}} \frac{\mathrm{d}s}{r_\odot} \left(\frac{\rho_{\text{main}}[r(s,\psi)]}{\rho_\odot} \right)^2 . \tag{4.12}$$

In the case of flux originating from many distant subhalos, we may treat each one as a point source of radiation. In this case, the diffuse flux per solid angle requires a sum over each contributing source with density ρ_i and distance d_i within the observed solid angular region $\Delta\Omega$:

$$\bar{J}_{\text{sub}} = \frac{1}{\Delta\Omega} \sum_{\Delta\Omega} \left(\frac{1}{4\pi d_i^2} \int \mathrm{d}V \frac{\rho_i^2}{m_\chi^2} \right) . \tag{4.13}$$

This clearly depends not only on the density profiles, but also on the distribution of subhalos in the Galaxy. We will not present the results of the distant subhalo calculation of final-state radiation here, since it has been thoroughly explored by other authors in similar contexts. We direct the interested reader to references [67, 4, 137].

Finally, if a particular subhalo is close enough to subtend an angle larger than the detector's pixel size, it can no longer be treated as a point source: eq. (4.12) must be used, including the angular dependence of the projected density profile of the given subhalo, $\rho_{SH}(R, \theta, \phi)$. We will return to this case in Section 4.4.2.

The particle physics contribution to (4.10) and (4.11) comes from the photon spectrum, defined as:

$$\frac{\mathrm{d}N}{\mathrm{d}E_\gamma} = \frac{1}{\langle\sigma v\rangle_{\text{total}}} \frac{\mathrm{d}\langle\sigma v\rangle}{\mathrm{d}E_\gamma} \tag{4.14}$$

In the case of a two-lepton final state [138]:

$$\frac{\mathrm{d}N}{\mathrm{d}x} = \frac{\alpha}{\pi} \frac{1+(1-x)^2}{x} \log \left(\frac{s(1-x)}{m_e^2} \right) \tag{4.15}$$

where $x = 2E_\gamma/\sqrt{s}$ and s is the standard Mandelstam variable. We are interested in the case of TeV dark matter χ annihilating to a four-lepton final state, with a $\mathcal{O}(1)$ GeV leptophilic gauge boson B as the messenger. The annihilation is dominated by $\chi\chi \to BB$, where the B's are on shell. The cross section can be obtained by first

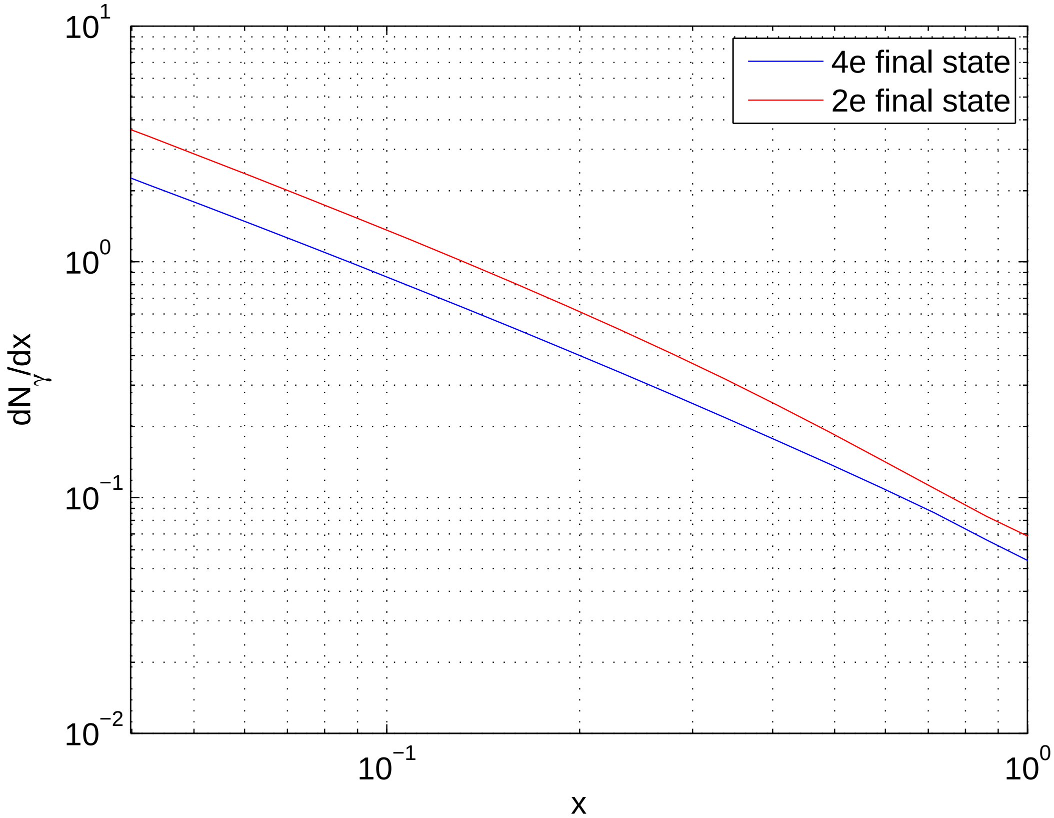

Figure 4.3: Spectrum of prompt gamma rays (brehmsstrahlung) from leptons produced by DM annihilation, as a function of $x = 2E_\gamma/\sqrt{s} \cong E_\gamma/M_{DM}$. The red line (upper) represents the result of the $2e$ final state, and the blue line (lower) corresponds to $4e$ final states.

computing in the rest frame of the B using the decay $B \to e^+ + e^-$ and then boosting to the lab frame, in which the slowly moving DM particles are approximately at rest. This can easily be done numerically. We present the resulting spectrum in fig. 4.3. Since we will not make use of the final-state bremsstrahlung for other annihilation channels (4μ or 4π) we will not discuss their spectra.

4.3.2 Inverse Compton Scattering

Charged particles travelling through the interstellar medium scatter off ambient photons of the interstellar radiation field (ISRF), which is composed of microwave ($\sim 10^{-3}$ eV) radiation from the cosmic microwave background (CMB), infrared ($\sim$

10^{-2} eV) radiation from dust, and optical ($\sim$ eV) photons from starlight. Along with the galactic magnetic fields, this is the main source of energy loss for electrons diffusing within the Galaxy. We will show that ISRF photons that have scattered with TeV-scale electrons have spectra that peak at several hundred GeV, which should fall squarely within the measurement window of diffuse gamma rays by the Fermi Large Area Telescope (LAT).

Once integrated over scattering angles, the well-known Klein-Nishina formula for the Compton scattering process $e^{\pm}\gamma \to e^{\pm}\gamma'$ can be integrated along the line of sight to give the total flux of scattered photons per solid angle arriving on a detector [139, 64]:

$$\frac{d\Phi_{\gamma'}}{dE_{\gamma'}d\Omega} = \frac{1}{2}\hbar^2 c^3 \alpha_{EM}^2 \int_{\text{l.o.s.}} ds \int\int \frac{dn_e}{dE_e}\frac{du_\gamma}{dE_\gamma}\frac{dE_\gamma}{E_\gamma^2}\frac{dE_e}{E_e^2} f_{IC} \tag{4.16}$$

$\int_{\text{l.o.s.}} ds$ represents the line-of-sight integral from the observer's position to infinity (practically speaking, to the edge of the diffusion zone). We have used the definitions:

$$f_{IC} = 2q\log q + (1+2q)(1-q) + \frac{1}{2}\frac{(\epsilon q)^2}{1+\epsilon q}(1-q) \tag{4.17}$$

and

$$\epsilon = \frac{E_{\gamma'}}{E_e}, \quad \Gamma = \frac{4E_\gamma E_e}{m_e^2}, \quad q = \frac{\epsilon}{\Gamma(1-\epsilon)}. \tag{4.18}$$

We numerically integrated eq. (4.16) along the line of sight, as well as over the incoming particle energies. All the quantities in the integrand are known: we used the two-dimensional (r,z) distribution of electrons and positrons dn_e/dE_e from DM annihilations produced with GALPROP, as discussed in Section 4.2. For the ISRF, we used a realistic two-dimensional photon energy density distribution du_γ/dE from [123], which is publicly available on the GALPROP website. Both distributions assumed cylindrical symmetry around the Galactic axis. For each galactic latitude-longitude pair, the line of sight integration was performed in a three-dimensional sky from the Sun's position to the edge of the diffusion zone which was taken to extend to a radius $r_{max} = 20$ kpc and to a height $|z|_{max} = 5$ kpc above and below the galactic plane. A trapezoidal integration step size of 0.1 kpc was found to be numerically converged.

The values of dn_e/dE_e and du_γ/dE at each step were found in the heliocentric coordinate system by using a bilinear interpolation scheme. On top of the DM annihilation products, we used the densities of primary and secondary electrons as well as secondary positrons to compute the ICS contribution of the background lepton field. This had the effect of further constraining the gamma ray background.

We performed the integration once per grid point on an equally-spaced $20° \times 20°$ latitude-longitude grid of the quarter-sky in the ranges $\theta = [0, \pi/2]$, $\phi = [0, \pi]$. This was sufficient to reconstruct the entire sky, given the symmetry of the data input.

4.3.3 Fermi all-sky diffuse gamma ray measurements

The Fermi Large Area Telescope (LAT) is a high-sensitivity gamma ray instrument capable of detecting photons in the $\sim$ 30 MeV to $>$ 300 GeV range. It has an effective detector area of $\sim$ 8000 cm^2, a 2.4 sr field of view and can resolve the angle of an incident photon to 0.15° at energies above 10 GeV. Data from the first year of observation are publicly available from the Fermi collaboration.

We used the all-sky diffuse photon file from the Fermi weekly LAT event data webpage [77]. This covered observations from mission elapsed time (MET) 239557417 to MET 272868753 (seconds), corresponding to 55 weeks of observation between August 8 2008 and August 25 2009. We processed the photon data with the Fermi LAT science tool software, available from the Fermi Science Support Center (FSSC) website. We first removed all events with a zenith angle greater than 105° to eliminate Earth albedo. The data were further trimmed to keep only the photons measured during "good" time intervals. We then created an exposure cube from the spacecraft data for the corresponding period, to account for effective instrument exposure. The data were separated into $0.25° \times 0.25°$ latitude and longitude bins spanning the entire sky, and into 16 logarithmically separated bins from 100 MeV to 200 GeV. Uncertainties were assigned according to Ref. [140]. We compared our results to the August-December 2008 $10^0 \leq |b| \leq 20°$ spectrum presented by the Fermi collaboration [140]. The half-year data agreed exactly, while adding the extra 8 months to the full 55-week dataset changed the picture only very slightly. We rebinned the data into a 40×40 grid, in correspondance with the ICS computation.

Before proceeding to the results of our numerical analyses, we should note that many factors contribute to the theoretical uncertainty. While we were able to reproduce the results of Simet et al. [117] quite closely, there are substantial discrepancies between the results of GALPROP and other methods of solving the transport equation. This lack of agreement is further discussed in [2]. There is an additional uncertainty in the injection spectrum of primary electrons, which serve, along with secondary electrons and positrons from spallation, as the astrophysical background to our results.

4.4 Empirical fits

As expected, we found that allowing subhalos to contribute to the overall flux of DM annihilation products reduced the flux of expected gamma rays from the galactic center, while increasing fluxes at higher galactic latitudes. The most stringent constraints were from the low-longitude regions just above and just below the galactic plane, where astrophysical sources of gamma rays are less prominent, but the DM distribution is still quite dense. Specifically, we used the lower right-hand region ($-9° < b < -4.5°$, $0° < \ell < 9°$ in Galactic coordinates) which was found to be the most constraining, in agreement with Ref. [115].

After including the ICS from background electrons and positrons, we found that the boost factor of a main halo 1 TeV DM annihilation process cannot violate the bound $BF \leq 25$ if the signal is to remain below the top Fermi LAT error bars. If we extend the constraint to $\Phi_\gamma <$ Fermi $+2\sigma$, this condition is only slightly relaxed to $BF \leq 30$. In the case of a 2.2 TeV DM candidate, these bounds become $BF \leq 42$ and $BF \leq 52$ at 1σ and 2σ, respectively. While this agrees qualitatively with other works [64, 115], we attribute our more stringent upper bounds mainly to our higher $\rho_\odot$, as discussed in section 4.2.1, to our inclusion of the ICS contribution from background electrons and positrons,but mainly to the different method used to solve the diffusion equation (4.1).

Using the best fit scenario of Ref. [2], the reduction of flux was however not enough to overcome the constraints from the Fermi observations. This is illustrated in figure 4.4, which shows that the MH+SH scenario still violates constraints from the data by as much as 4σ. On its own, the predicted flux exceeded the data at energies above 100 GeV by at least 2σ, while we expect that additional constraints from $\pi^0 \to 2\gamma$ decays should also be large in this energy range [141] and push predictions from this model even farther outside of the observationally allowed region. Allowing the background to freely vary (top section of Table 4.1) made no appreciable difference with respect to gamma rays, and was not enough to satisfy the observational constraints.

Figure 4.5 illustrates how the ICS gamma ray flux is increased at higher galactic latitudes when subhalos are included. It should however be emphasized that the predicted fluxes in this region of the sky are still well below the level of Fermi observations.

4.4.1 Less cuspy dark matter profiles

In section 4.2.1 we mentioned the motivations for considering less cuspy DM profiles. Many previous works studying the ICS constraints have compared the effects of cored versus cuspy DM profiles, noting that the constraints are weaker for cored profiles. To better quantify exactly how much cuspiness can be tolerated, it is interesting to vary the parameters of the Einasto profile that control this [142, 131]. In particular, larger values of α and r_s correspond to less concentrated halos. We ran simulations of the lepton distribution and gamma ray fluxes with slightly different parameters for equation (4.6) while keeping the local density constant at $\rho_\odot = 0.37$ GeV cm^{-3}. This is illustrated in fig. 4.6. Flatter profiles with $\alpha = 0.20$ or 0.25, $r_s = 30$ kpc reduce the gamma ray fluxes somewhat, but not enough to bring the predicted flux to within the observations in the offending energy bins between 10 and 100 GeV. The same is true for the isothermal profile, whose corresponding results are shown in fig. 4.7. For both cases, the problem arises because the predicted background gamma flux is not far below the observed flux in the most constraining bins. This leaves very little room for the additional contribution from the DM decay products ICS signal.

Increasing the intermediate gauge boson mass to 1 GeV, and thus allowing a decay to muons and pions according to the branching ratios described in Section 4.2.2 does not alleviate the problem. Indeed, the 1σ (2σ) bounds become BF < 23 (< 28) for an Einasto profile, and BF < 63 (< 72) in the isothermal case. These fall well short of the required BF $= 118$ to explain the Fermi and PAMELA excesses, as long as the DM mass is increased to $M_{DM} = 1.2$ TeV. These results are summarized in the bottom of Table 4.2. The reason ICS constraints are stronger when muons are included is due to the nature of the data. Indeed, the peak of the ICS spectrum lines up with the most constraining data point when $M_{DM} = 1.2$ TeV. This provides a stronger than expected constraint, relative to the 4e final state at $M_{DM} = 1$ TeV.

4.4.2 Close subhalo

The above analyses implicitly assume that no single subhalo dominates the lepton signal. But if a subhalo happens to be very close (within a kpc) to the solar system, the picture changes significantly, since the electrons and positrons from the close subhalo can dominate the observed flux, and its gamma ray emissions can come from a sizable solid angle in the sky. We treat this case separately from the previous subhalo scenario, since a larger DM mass is no longer required to produce the observed lepton signal; rather, the small amount of ICS energy loss during propagation from a local subhalo means that a 1 TeV-scale DM particle appropriately conforms to the Fermi $e^+ + e^-$ measurements. We concentrate on the 4e final state channel, although previous results allow this to be generalized. The solution depends linearly on the spectrum dN_e/dE, so that the boost factor required to explain the observed lepton excess should scale in the same way that it does in the main halo scenario: $BF_{(e,\mu,\pi)}/BF_{4e} \simeq 118/110$, as read from Table 4.1.

Since GALPROP is not easily adapted in its 2D mode to include the effects of a highly localized additional source term, we adopt a semi-analytic approach to solve the diffusion equation (4.1) for leptons produced in the nearby subhalo. Given that the leptons and gamma rays in this scenario would be from a local origin, the spatial

Subhalo	r_s (kpc)	ρ_s	$\log BF$	$d_{\rm min}$ (pc)	$V_{\rm max}$ (km/s)
1	0.01	69	4.74	33.9	2.9
2	0.1	3.46	4.34	95.5	6.7
3	3.2	0.04	3.76	178	22
4	0.9	1.27	2.35	165	36
5	1.1	2.0	1.70	170	55
Main halo, 4e channel					
Einasto	25	0.048	$< \substack{1.40 \\ 1.48}$	–	$201 - 277$
Isothermal	3.2	2.32	$< \substack{1.81 \\ 1.88}$	–	$201 - 277$
Main halo, 4e + 4μ + 4π channel					
Einasto	25	0.048	$< \substack{1.36 \\ 1.45}$	–	$201 - 277$
Isothermal	3.2	2.32	$< \substack{1.80 \\ 1.86}$	–	$201 - 277$

Table 4.2: Upper rows: parameters of each subhalo we examined. r_s and ρ_s (in units GeV cm^{-3}) characterize the halo's Einasto profile (with $\alpha = 0.17$), $\log BF$ is the logarithm of the necessary boost factor in order to obtain the Fermi lepton data entirely from the given subhalo and $d_{\rm min}$ is the minimum distance (in pc) from our position to such a subhalo along the sun-GC axis, with the given boost factor, that would not exceed the gamma ray observations. $V_{\rm max}$ is the maximum circular velocity, which appears in the radial velocity dispersion, fig. 1.3. Lower rows: similar data for the main halo using Einasto or isothermal profiles, but $\log BF$ denotes the 1 and 2σ upper limits to satisfy gamma ray constraints.

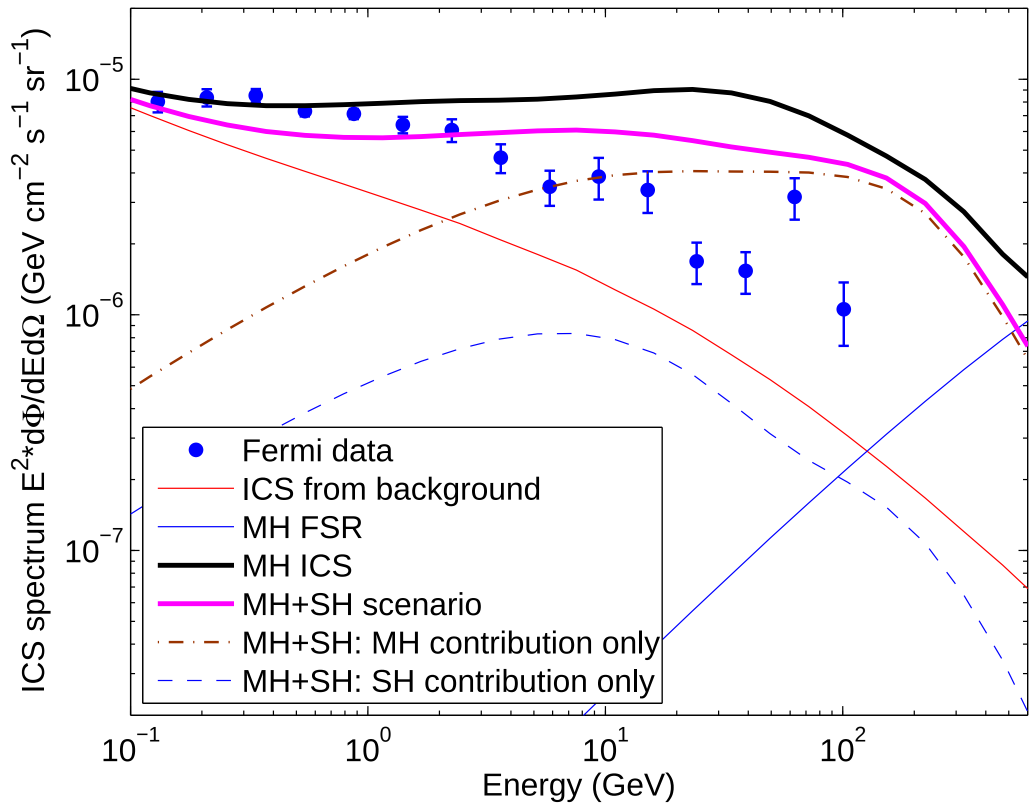

Figure 4.4: Galactic-center ICS gamma ray flux from the region $-9° < b < -4.5°$, $0° < \ell < 9°$ for the MH scenario ($M_{DM} = 1$ TeV), top black solid line, are reduced in the MH+SH scenario ($M_{DM} = 2.2$ TeV), middle magenta solid line, but not enough to overcome constraints from Fermi LAT observations, which are violated by as much as 4σ. The parameters for the Einasto profile are $\alpha = 0.17$, $r_s = 25$ kpc. The background gamma rays (red solid line) include only ICS from background electrons and positrons, but clearly constrain the model even more. Further contributions are expected from bremsstrahlung, extragalactic gamma rays and π^0 decays. The latter may dominate the spectrum at these energies and are responsible for the hump shape around 1 GeV [141].

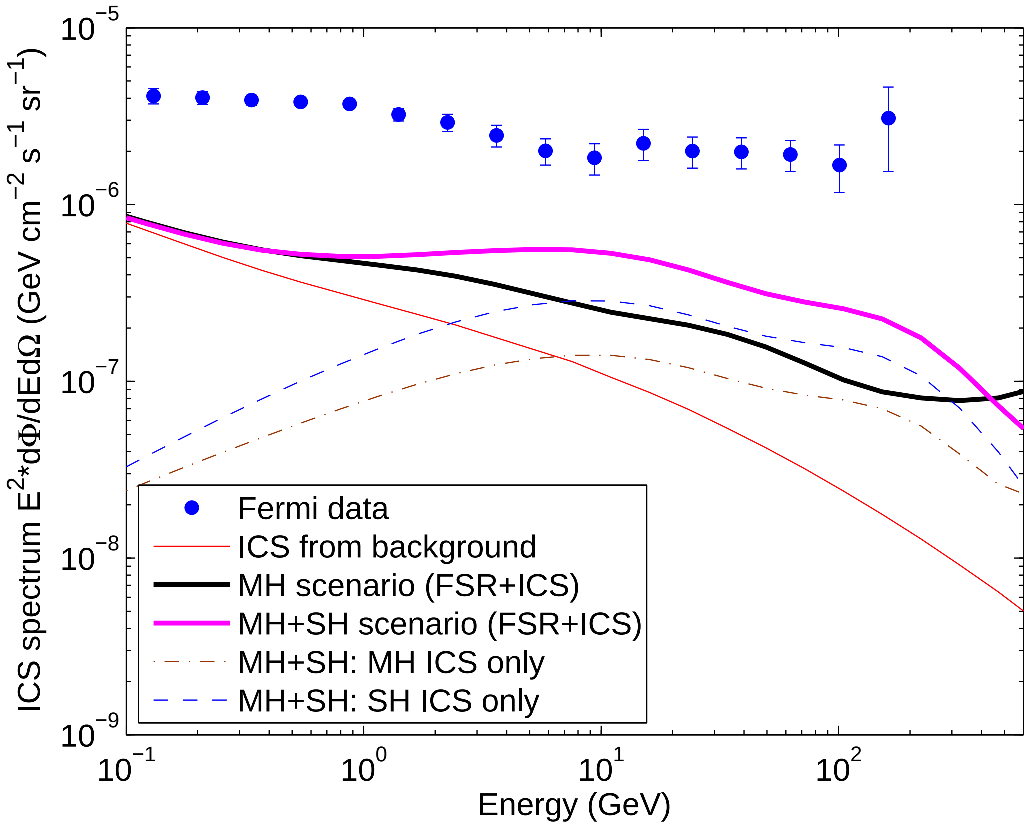

Figure 4.5: Mid-latitude ICS gamma rays from the region $42° < |b| < 47°$, $9° < |\ell| < 18°$. In this case the MH scenario ($M_{DM} = 1$ TeV), black solid line, predicts fewer ICS gamma rays than the MH+SH scenario ($M_{DM} = 2.2$ TeV, magenta solid line). At these latitudes constraints are much weaker, and neither model is ruled out by the observations.

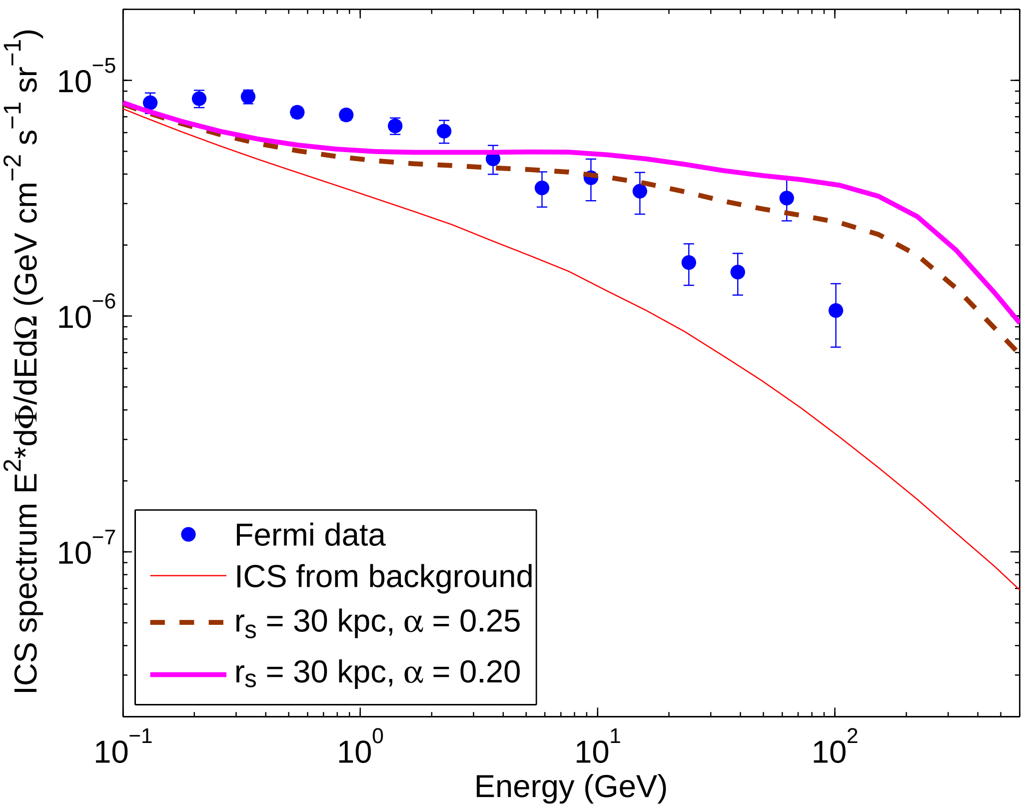

Figure 4.6: $-9^\circ < b < -4.5^\circ$, $0^\circ < \ell < 9^\circ$ region. Similar to previous figures, showing how reducing the cuspiness of the Einasto profile (eq. (4.6)) reduces predicted total gamma ray signal (magenta line). Here $\alpha = 0.20, 0.25$ respectively and $r_s = 30$ kpc.

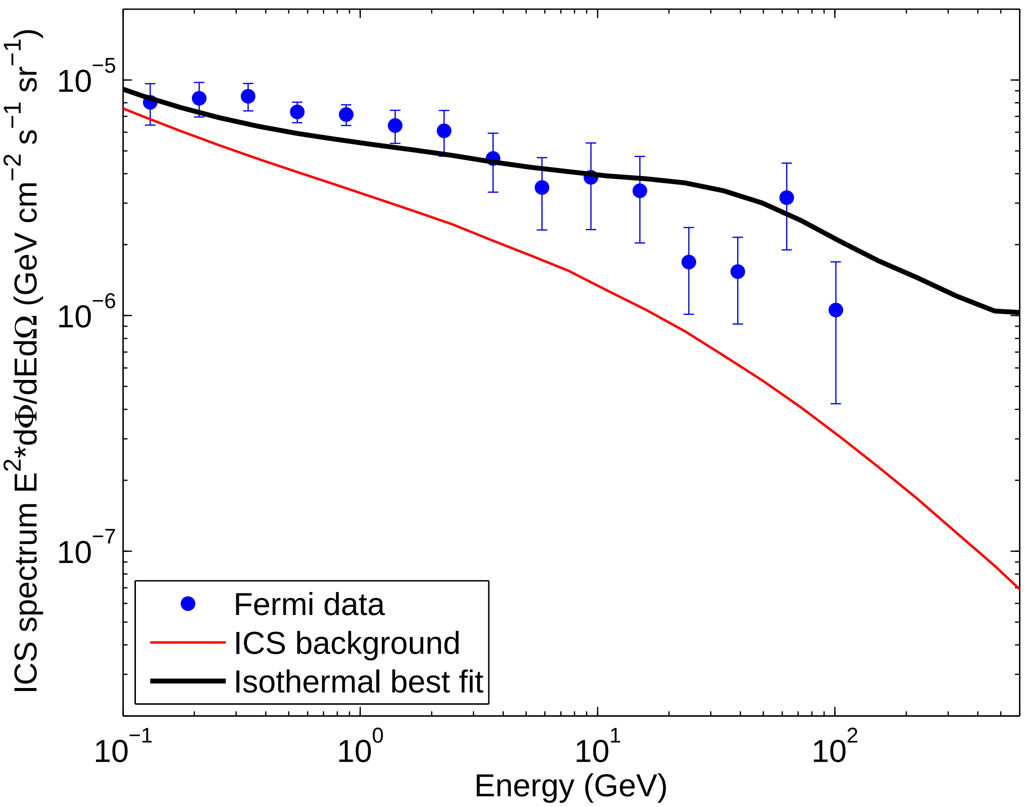

Figure 4.7: $-9^\circ < b < -4.5^\circ$, $0^\circ < \ell < 9^\circ$ region. Similar to previous figures, using the cored isothermal profile with $r_s = 3.2$ kpc and $\rho_s = 3.0$ GeV/cm^3.

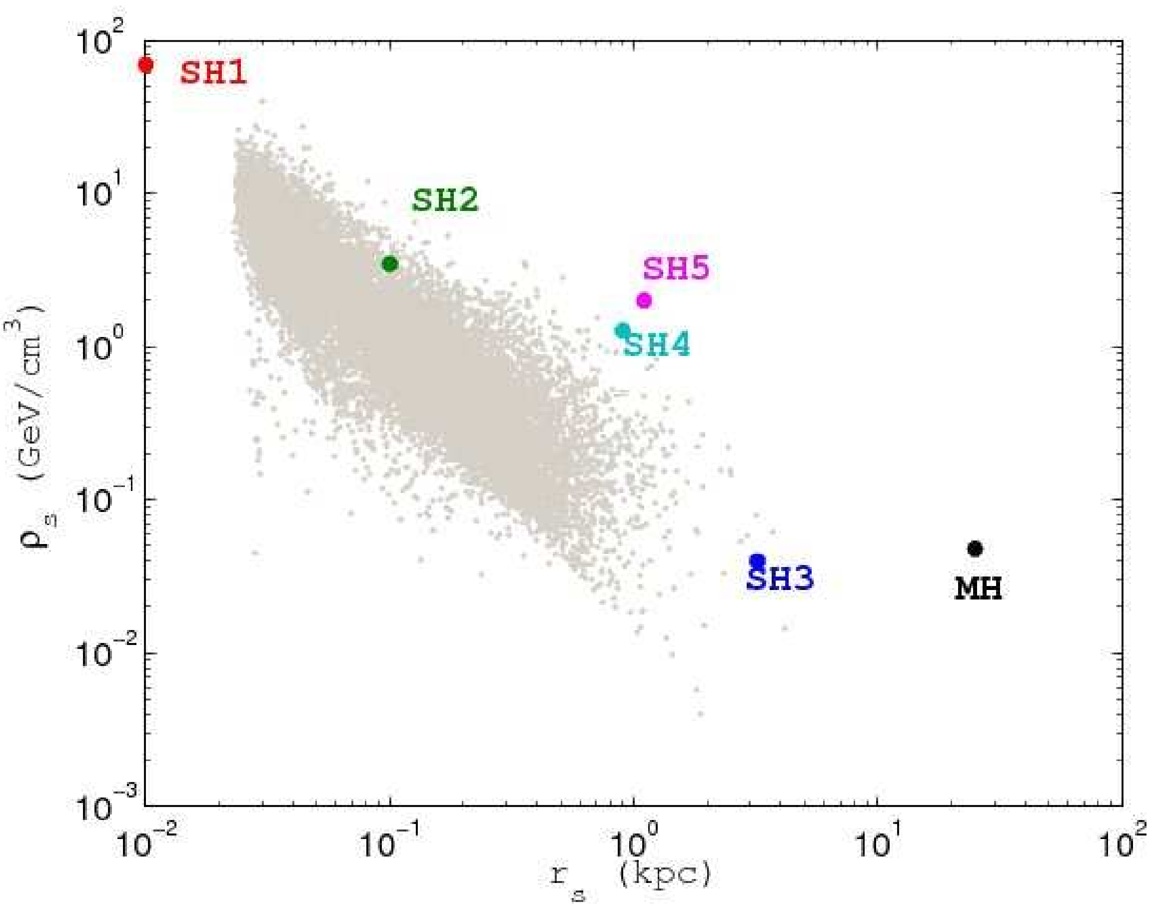

Figure 4.8: Grey regions: scatter plot of ρ_s versus r_s for subhalos in the *Via Lactea II* simulation. Dots represent the main halo (MH) and subhalos given in table 4.2.

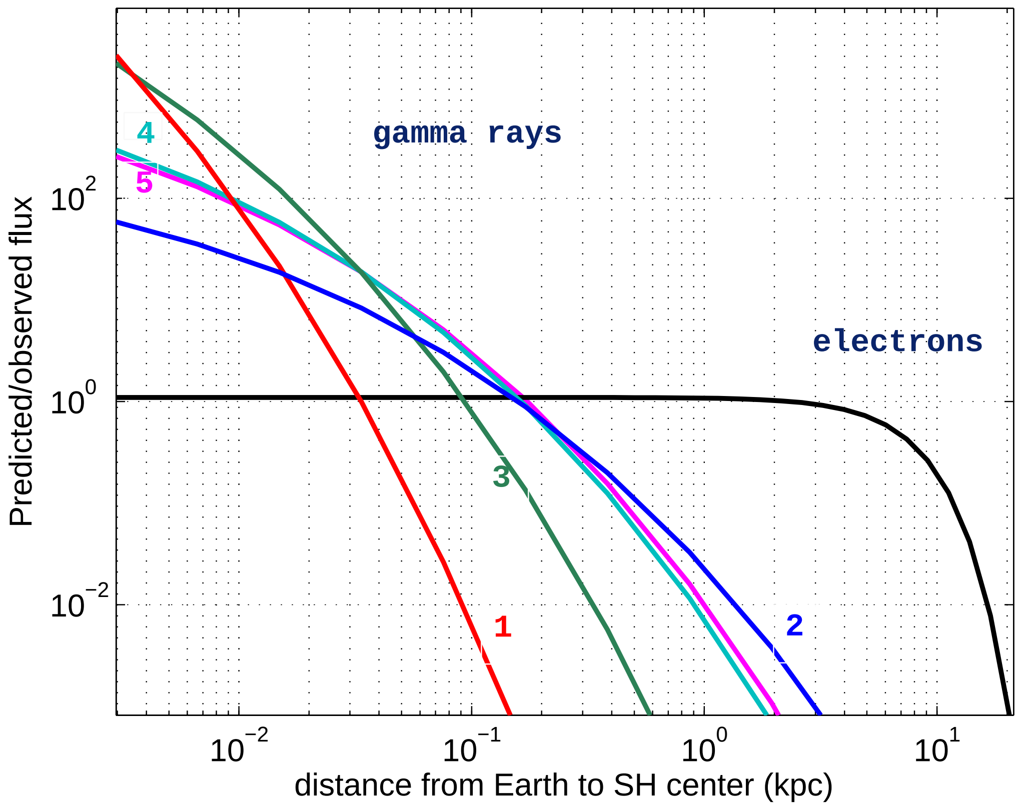

Figure 4.9: Fluxes of gamma rays and $e^{+}+e^{-}$ from the five subhalos presented in Table 4.2. The gamma ray fluxes (curve labeled by the number of the corresponding subhalo) are at $E_{\gamma}=137$ GeV, whereas the leptons are at an energy of 559 GeV (the peak of the observed Fermi spectrum). In both cases, the amplitude is the predicted flux divided by the observed flux from the Fermi satellite, such that a value of 10^{0} means that the predicted flux is equal to the observed value. Boost factors in each case (as given in table 4.2) were fixed to allow the Fermi lepton signal to be explained entirely by the subhalo. The allowed position of each subhalo with respect to earth is therefore the region to the right of each gamma ray curve, up to ~ 2 kpc where the lepton flux starts to fall.

dependence of the interstellar radiation and magnetic fields becomes much less important. We used the method described in ref. [75], with the same diffusion parameters as presented in section 4.2 (of the present work), but with an energy-loss coefficient parametrized by

$$b(x, E) = -\frac{\mathrm{d}E_e}{\mathrm{d}t} = \frac{E_e^2}{\tau_E} \tag{4.19}$$

with $\tau_E = 10^{16}$ s GeV characterizing the local energy loss rate.

We sampled subhalos from the *Via Lactea II* simulation to identify examples that could allow for simultaneously fitting the PAMELA/Fermi lepton fluxes and the Fermi gamma ray fluxes. Four such examples are labeled as SH1-SH4 in table 4.2, and a fifth (SH5) is one that we have "engineered" by choosing parameters that are close to those of SH4, but with a higher density and hence higher circular velocity, dynamically related to each other by eq. (13) of [4],

$$V_{\max}^2 = f_V 4\pi G \rho_s r_s^2 \tag{4.20}$$

with $f_V = 0.897$. Due to the higher density, SH5 requires a lower boost factor to produce the observed lepton signal, and so it represents a kind of best-case scenario. The distribution of *Via Lactea II* subhalos in the space of (r_s, ρ_s) is shown as a scatter plot in fig. 4.8, and the five subhalos of interest are highlighted on this plot. They are atypical in the sense of needing a higher-than-average central density. A further caveat is that such a large r_s is unlikely at small distances from the GC due to tidal disruption. Indeed, subhalos within the visible galaxy in the *Via Lactea II* simulation were of the order $r_s = 0.05 \sim 0.85$ kpc, falling below the $0.9 \sim 1.1$ kpc compatible with the most plausible particle physics scenario discussed in Section 4.5.

Each subhalo was situated along an optimal axis, namely that connecting the earth to the GC. Such an accidental alignment makes it easier to "hide" the gamma rays originating from the subhalo since they are coming primarily from the same direction as the GC, where the background emissions are strongest. This is also the reason that the most stringent ICS constraints on the main halo arise from the regions $4.5° < |b| < 9°$ of galactic longitude instead of the most central region. However in this case we find that the biggest contribution to the emission is from final-state bremsstrahlung rather than ICS. The latter is found to produce gamma ray fluxes that are 3 orders of magnitude smaller than observed. This is consistent with the fact that the main source of ICS is IR radiation and starlight, which is concentrated far from the vicinity of the solar system.

Results were then compared to the Fermi lepton and gamma ray data in order to establish constraints. The strictest gamma constraints were at the largest energy data point from the Fermi LAT analysis of $E = 162$ GeV, because of the shape of the FSR spectrum, which rises steadily until ~ 1 TeV. We used a slightly different region of the sky than in our previous ICS analysis, $4.5^\circ < |b| < 9^\circ$, $9^\circ < |\ell| < 18^\circ$, because there were not enough good data points in this energy bin at lower longitudes to constrain the data. We compared the lepton prediction to the Fermi measurements at 559 GeV, where the observed $e^+ + e^-$ spectrum is at a maximum deviation from a power law. In both cases we included the additional constraints from astrophysical backgrounds computed by GALPROP and by our ICS routine.

Results are shown in fig. 4.9. If the single subhalo is allowed to saturate the observed lepton signal, fig. 4.9 gives clear bounds (summarized in Table 4.2) on the proximity of each subhalo, providing a minimum distance from the solar neighborhhod to such a subhalo. So long as the boost factor for the main halo remains sufficiently small, this scenario can therefore overcome the ICS constraints that restricted the standard MH-only model.

4.4.3 Astrophysical prediction and extragalactic constraints

In figure 4.10 we provide an example of the gamma ray flux predicted by the close subhalo scenario, as compared to the main halo scenario. The gamma ray flux comes predominantly from final state radiation rather than inverse Compton scattering of the annihilation products. We chose the energy bin $E = 23$ GeV, which is the most constraining for the main halo case. Although both scenarios converge at high latitudes, low latitude measurements have already ruled out the main halo scenario, and provide a way to constrain the model. With more exposure and precise removal of point sources, the Fermi LAT may provide a diffuse background low enough to rule out these predictions. As a further test, census experiments such as the upcoming Gaia satellite may provide a precise enough map of the local gravitational potential to confirm or rule out the presence of such a DM overdensity [143]. Direct measurement of such an overdensity would however be difficult: a subhalo such as SH5, located at a distance that would not saturate gamma ray bounds, would contribute less than 0.1% of the local DM density.

From previous works, we infer that extragalactic bounds on this scenario are not as strong as the ones we have computed above. Bounds from dwarf spheroidal galaxies could plausibly be important since the velocity dispersions are of the same order as what is required for our subhalo enhancement, *i.e.* $\sim 10 - 50$ km s^{-1} [144]. However, the most stringent Fermi LAT bounds [145] from such galaxies put the upper limit on DM annihilation into a 2μ final state at around $BF = 3000$ if only final-state radiation is considered, and around 300 if ICS bounds are included as well. [146] computed the cosmological dark matter annihilation bounds for the same 2μ final state scenario, and find that BF larger than 300 is excluded at the 90% confidence level. This is using the results of the Millennium II structure formation simulation, and is indeed model-dependent. Extrapolation to the 4μ scenario is independent of astrophysics. We can therefore take the results of [64, 115] who have construced bounds on both channels. They show that FSR bounds are consistently an order of magnitude weaker in the 4μ case, given the softer photon spectrum in this scenario. We can therefore take these extragalactic results to be far less constraining than the stringent bounds from the center of our own galaxy.

Finally, we verify that this model does not saturate bounds on dipole anisotropy of the cosmic ray $e^+ + e^-$ spectrum. The dipole anisotropy can be defined as

$$\delta = 3\sqrt{\frac{C_1}{4\pi}}, \tag{4.21}$$

where C_1 is the standard dipole power of the measured electron and positron flux in the sky. The Fermi LAT collaboration [147] have presented upper bounds on this

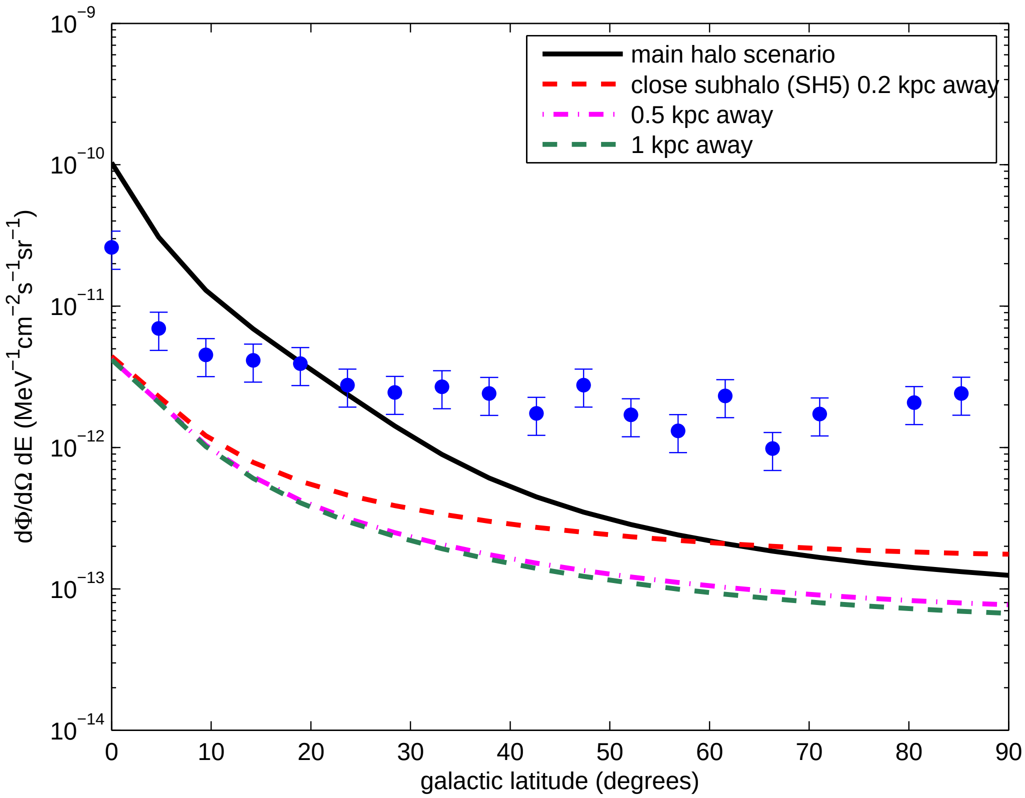

Figure 4.10: Dependence of predicted gamma ray fluxes on galactic latitude b, in the region $-9° < \ell < 9°$ at E = 23 GeV, the most constraining energy bin for the main halo scenario. Black: main halo scenario (Einasto profile, BF = 110) Dashed: subhalo 5, as specified in Table 4.2. Background ICS is included in both predictions, but signal is dominated by final state radiation. Dots are the Fermi data for that region and energy.

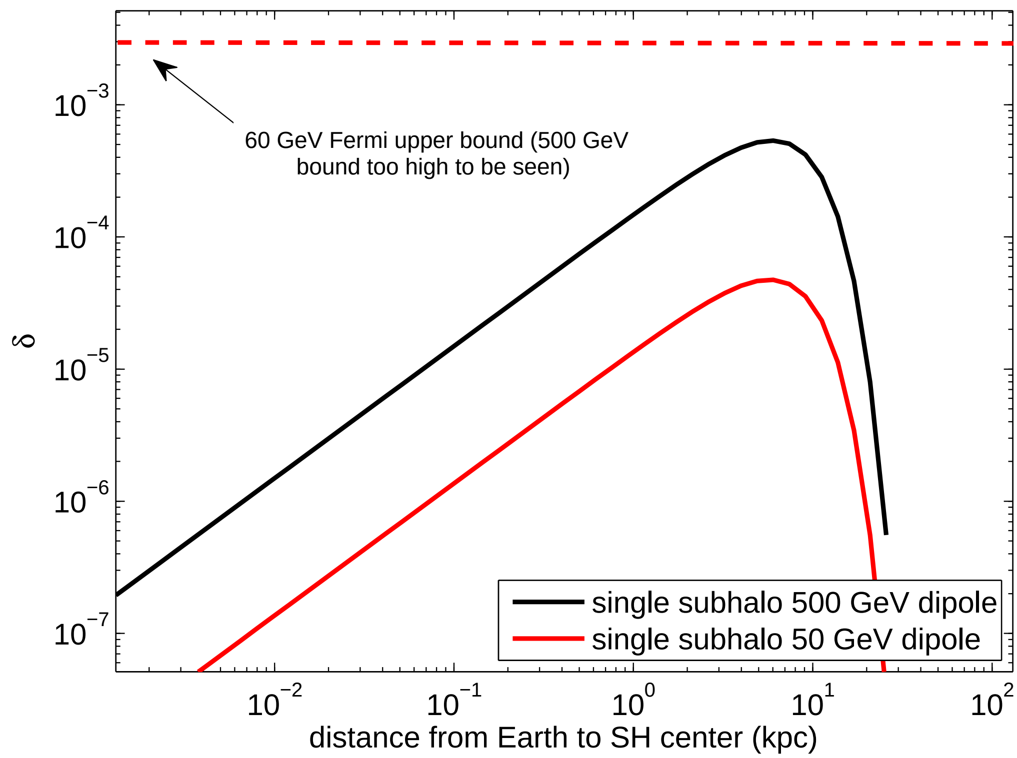

Figure 4.11: Dipole anisotropy δ of the cosmic ray electron and positron flux predicted by SH5 if it saturates the Fermi excess. Background cosmic ray electrons and positrons are included, and taken to be isotropic. δ increases monotonically with energy from the red line (60 GeV) to the black line (500 GeV).

quantity. These range from $\delta \lesssim 3 \times 10^{-3}$ at $E_e \simeq 60$ GeV up to $\delta \lesssim 9 \times 10^{-2}$ at $E_e \simeq 500$ GeV. Given a diffusive model, this can be computed [147]:

$$\delta = \frac{3D(E)}{c} \frac{|\vec{\nabla} n_e|}{n_e}, \tag{4.22}$$

where $D(E)$ is the diffusion coefficient (4.3) and n_e is the density of cosmic ray electrons and positrons, including astrophysical backgrounds. Taking the background to be isotropic, we computed the dipole anisotropy in the case of a single close subhalo producing enough electrons to explain the Fermi excess. In every case δ falls well below bounds. Results for SH5 are presented in Figure 4.11. The anisotropy rises monotonically with energy, from 60 GeV (red line) to 500 GeV (black line).

4.5 Particle physics realizations

In the previous sections we have identified scenarios where subhalos could provide the observed excess PAMELA and Fermi leptons, from a purely phenomenological perspective. In particular, certain values for the annihilation cross section boost factors are needed for the subhalos, and upper bounds for that of the main halo (depending upon assumptions about its density profile) were derived. It is interesting to ask whether simple particle physics models with boost factors from Sommerfeld enhancement can be consistent with these requirements.

The simplest possibility for model building is dark matter that annihilates into light scalar or vector bosons, which subsequently decay into leptons. This class of models automatically gives a boost factor to the annihilation cross section, through multiple exchange of the boson, resulting in Sommerfeld enhancement. However it is not obvious that one can find models with the desired boost factors for the subhalos and main halo. One constraint that limits our freedom is to not exceed the measured density of dark matter. It will turn out that our mechanism works most naturally if the DM responsible for signals in the galaxy is a subdominant component comprising some fraction $1/f$ of the total DM population [131], with $f > 1$.

We focus on the case of a GeV-scale U(1) vector boson that kinetically mixes with the photon. Such models have the advantage of naturally explaining the coupling to light leptons, without producing excess antiprotons that would contradict PAMELA observations. Let us denote the vector's mass by μ and the coupling by g, with $\alpha_g = g^2/4\pi$. If M is the DM mass, then the Sommerfeld boost factor is controlled by two dimensionless parameters: $\epsilon_\phi = \mu/(\alpha_g M)$ and $\epsilon_v = v/(\alpha_g c)$, where v is the DM velocity in the center of mass frame. A reasonably accurate approximation to the exact Sommerfeld enhancement is given by the expression [148, 149]

$$S = \frac{\pi}{\epsilon_v} \frac{\sinh X}{\cosh X - \cos\sqrt{\frac{2\pi}{\bar{\epsilon}_\phi} - X^2}} \tag{4.23}$$

where $\bar{\epsilon}_\phi = (\pi/12)\epsilon_\phi$ and $X = \epsilon_v/\bar{\epsilon}_\phi$. (The cosine becomes cosh if the square root becomes imaginary.)

To take into account leptophilic DM that is only a subdominant component of the total DM, suppose that $\alpha_{g,\mathrm{th}}$ is the value of α_g that would give the correct thermal abundance, which scales like the inverse annihilation cross section $\sigma^{-1} \propto \alpha_g^{-2}$; then we can parametrize $\alpha_g = \sqrt{f}\,\alpha_{g,\mathrm{th}}$. The rate of annihilations goes like $\rho_l^2\sigma \propto 1/f$ if ρ_l stands for the leptophilic component of the DM. We accordingly define an effective boost factor

$$\bar{S} = \frac{S}{f} \tag{4.24}$$

where S is the intrinsic Sommerfeld enhancement factor. Thus any constraint on S in a theory with $f = 1$ becomes a constraint on $\bar{S}$ in the more general situation.

4.5.1 Averaging of boost factor

Of course, the DM velocity has no definite value; instead we need to average over the possible values within the subhalos and the main halo, weighted by the appropriate distribution function. We take it to be Maxwell-Boltzmann with a cutoff at some escape velocity,

$$f(v) = N e^{-3v^2/2v_s^2}\,\theta(v_{\mathrm{esc}} - v) \tag{4.25}$$

This isotropic form is only an approximation since the true distribution has some small anisotropy between the radial and angular components; we will for simplicity ignore this complication. The velocity dispersion $v_s = \langle v^2 \rangle^{1/2}$ depends upon the radial distance r from the center of the halo or subhalo. The dependence has been measured for the subhalos in the *Via Lactea II* simulation; see figure 1.3. The shape is universal, but is scaled along the respective axes by parameters V_{max} and $r_{V_{max}}$ that depend upon the subhalo. The latter is related to the scale radius by $r_{V_{max}} = 2.212\, r_s$; the former is given by (4.20) and also listed in table 4.2 for the subhalos of interest. For numerical purposes we fit the sides of the curve passing through the points of fig. 1.3 by lines (omitting the rightmost point), and the middle by an inverted parabola.[2] We use the same form of v_s for the main halo, with $r_s = 25$ kpc and $V_{\max} = 201$ km/s. Other authors have advocated higher values of the velocity dispersion, $v_s = 309$ km/s at $r = r_\odot$ [150], which would correspond to $V_{\max} = 277$ km/s in the present parametrization. We will also consider the higher value to take account of this uncertainty.

The escape velocity can be computed explicitly for the subhalos from the standard result $\frac{1}{2}v_{\rm esc}^2 = G\int_r^\infty (M(r)/r^2)\,dr$, where $M(r) = 4\pi\int_0^r r^2\rho\,dr$ is the mass within radius r. The result for an Einasto profile is

$$\begin{aligned} v_{\rm esc}^2 &= G\,\rho_s\,e^{2/\alpha}\,\frac{8\pi}{\alpha}\left(\frac{\alpha}{2}\right)^{3/\alpha}\left[\left(\tfrac{2}{\alpha}\right)^{1/\alpha}\Gamma\left(\tfrac{2}{\alpha},\tfrac{2}{\alpha}(\tfrac{r}{r_s})^\alpha\right)\right. \\ &+ \left.\frac{r_s}{r}\left(\Gamma\left(\tfrac{3}{\alpha}\right)-\Gamma\left(\tfrac{3}{\alpha},\tfrac{2}{\alpha}(\tfrac{r}{r_s})^\alpha\right)\right)\right], \end{aligned} \tag{4.27}$$

where $\Gamma(s,x)$ is the upper incomplete gamma function. For the main halo, this procedure would not be correct because of the significant contribution of baryons, not included here. We adopt the result for $v_{\rm esc}$ of ref. [131] for the main halo (see appendix C of that reference).

With these ingredients, we can compute an average Sommerfeld enhancement factor $\langle S\rangle$ for each subhalo:

$$\langle S\rangle = \frac{\int_{r_1}^{r_2} dr\,r^2\,\rho^2\int d^3v_1\,d^3v_2\,f(v_1)\,f(v_2)S(\frac{1}{2}|\vec v_1-\vec v_2|)}{\int_{r_1}^{r_2} dr\,r^2\,\rho^2} \tag{4.28}$$

The factor of $\frac{1}{2}$ in the argument of S occurs because the v appearing in eq. (4.23) through ϵ_v is half of the relative velocity. ρ^2 is the appropriate weighting factor because the rate of annihilations is proportional to $\langle\sigma v\rangle\rho^2$. For the subhalos, the range of integration for r is from 0 to ∞, but for the main halo we take lower and

[2] The velocity dispersion curve is fit by

$$y = \begin{cases} 1.309 + 0.232x, & x < -0.841, \\ 0.976 - 0.3437x, & x > -0.383 \\ 0.9618 - 0.5475x - 0.4413x^2, & \text{in between} \end{cases} \tag{4.26}$$

where $x = \log_{10} r/r_{V_{\max}}$ and $y = v_s/V_{\max}$.

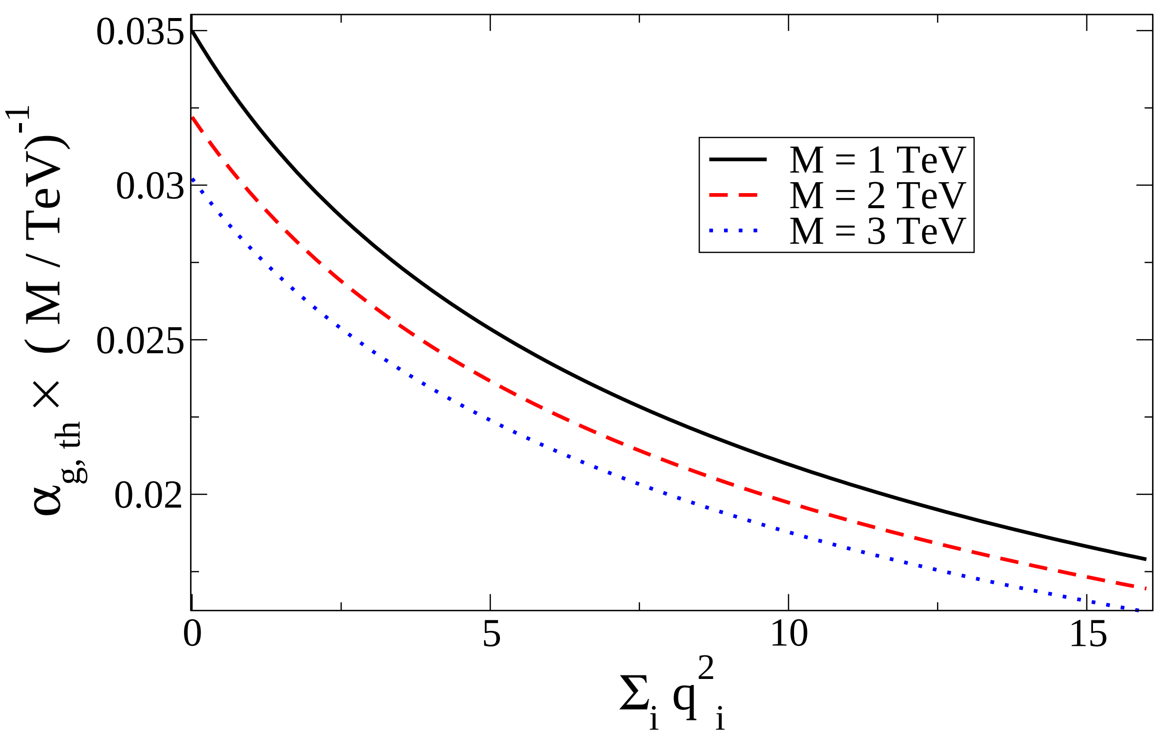

Figure 4.12: Value of gauge coupling leading to correct thermal relic DM density, $\alpha_{g,\text{th}}/M$, versus squared charge of dark Higgs bosons in U(1) model, for several values of DM mass M.

upper limits $r_{1,2}$ that correspond to the angular region of the sky that is used to set the gamma ray constraints: $r_1 = 0.67$ kpc and $r_2 = 1.34$ kpc. The reason is that the bound $\bar{S} < 30$ for the main halo comes from the gamma ray constraint rather than from lepton production. We are thus interested in the boost factor relevant to the region $4.5° < |b| < 9°$ of galactic latitude. The distances of closest approach to the galactic center, hence largest rate of γ ray production associated with these lines of sight, are given by $r = r_\odot \sin b$.

4.5.2 Relic Density Constraint

The enhancement factor (4.23) depends rather strongly on the gauge coupling α_g; therefore it is interesting to know what constraint the relic density places upon α_g. The effect of a Sommerfeld-enhanced DM model on the relic densitie has been discussed by [151]. Notice that DM transforming under a U(1) gauge symmetry as we have assumed must be Dirac and therefore could have a relic density through its asymmetry, similar to baryons. However, unless the DM was never in thermal equilibrium, then α_g should not be less than the usual value $\alpha_{g,\mathrm{th}}$ leading to the correct relic density, since otherwise the thermal component will be too large.

There are two kinds of final states for annihilation of DM in this class of models: into a pair of gauge bosons B_μ, by virtual DM exchange in the t and u channels, or into dark Higgs bosons h, by exchange of a gauge boson in the s channel. Assuming the DM (χ) is much heavier than the final states, the respective squared amplitudes, averaged over initial and summed over final spins, are

$$\frac{1}{4}\sum|\mathcal{M}|^2 = \begin{cases} 4g^4(1+2v^2), & \chi\chi \to BB \\ \frac{1}{2}g^4q^2(1-v^2\cos^2\theta), & \chi\chi \to h\bar{h} \end{cases} \tag{4.29}$$

where q is the U(1) charge of h relative to χ (replace $q^2 \to \sum_i q_i^2$ for multiple Higgs bosons), θ is the scattering angle, and we have included the leading dependence on the initial velocity v in the center of mass frame. The factor $\cos^2\theta$ averages to 2/3 in the integral over θ. In computing the associated cross section, it must be remembered that the $2B$ final state consists of identical particles, while the Higgs channel does not. The total amplitude can therefore be written in the form $\frac{1}{4}\sum|\mathcal{M}|^2 = 4g^4(a+bv^2)$, with

$$a = 1 + \tfrac{1}{4}\textstyle\sum_i q_i^2, \quad b = 2(1 - \tfrac{1}{12}\textstyle\sum_i q_i^2) \tag{4.30}$$

if we use the phase space for identical particles.

To find the cross section relevant during freeze-out in the early universe, we thermally average the v-dependent σv_{rel} following ref. [52]. We include approximately the effect of Sommerfeld enhancement as described there, to obtain

$$\begin{aligned} \langle\sigma v_{\mathrm{rel}}\rangle \;&\cong\; \frac{\pi\alpha_g^2}{2M^2}\left(a\left(1+\alpha_g\sqrt{\pi\tfrac{M}{T}}\right)\right. \\ &+\; \left.\frac{T}{M}(b-\tfrac{4}{3}a)\left(\tfrac{3}{2}+\alpha_g\sqrt{\pi\tfrac{M}{T}}\right)\right) \end{aligned} \tag{4.31}$$

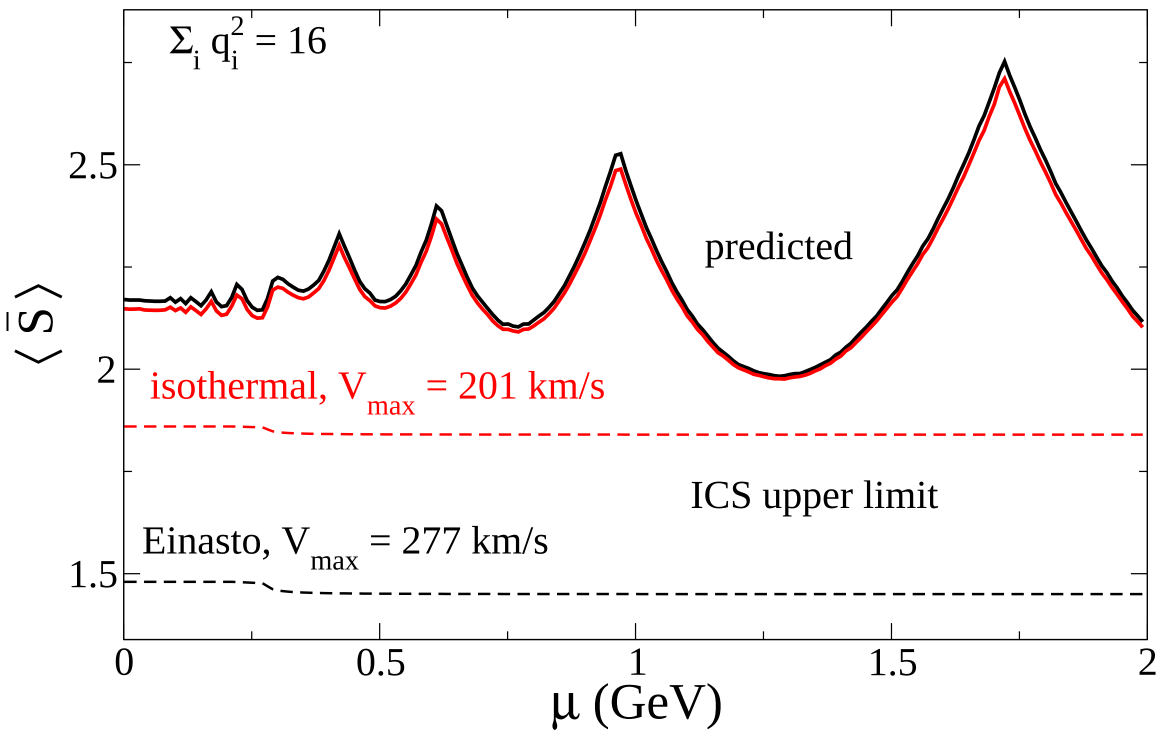

Figure 4.13: Solid lines: predicted main halo boost factor for thermal value of α_g, with dark Higgs boson charges $\sum_i q_i^2 = 16$ and maximum circular velocity $V_{\max} = 277$ km/s. Upper curve is for Einasto profile, lower for isothermal. Dashed line is 2σ upper limit from gamma rays produced by inverse Compton scattering. The failure to satisfy this bound even with large dark Higgs content and large $V_{\max}$ drives us to consider larger than thermal gauge couplings, $f > 1$.

The terms that are subleading in α_g, but enhanced by $\sqrt{M/T}$, are due to the Sommerfeld correction. We approximate the freeze-out temperature as $T \cong M/20$, the usual result of solving the Boltzmann equation for DM in the TeV mass range, and equate $\langle \sigma v_{\rm rel} \rangle$ to the value $\langle \sigma v \rangle_0 = 3 \times 10^{-26}$ cm^3/s usually assumed to give the correct relic density. This gives an implicit equation for $\alpha_{g,\rm th}$ of the form $\alpha_g^2 = c_1 M^2 \langle \sigma v \rangle_0 / (1 + c_2 \alpha_g)$, which however quickly converges by numerically iterating. Fig. 4.12 displays the resulting dependence of $\alpha_{g,\rm th}/M$ on $\sum_i q_i^2$ for several values of M.

The bound that the density of the leptophilic DM component not exceed the total DM density is $\alpha_g > \alpha_{g,\rm th}$. We parametrize the coupling by $\alpha_g = \sqrt{f}\,\alpha_{g,\rm th}$ with $f > 1$ in what follows.

4.5.3 Interpolation between $4e$ and mixed final states

In our numerical computations with GALPROP, we considered two cases for the final state annihilation channels: either $\chi\chi \to 4e$, applicable for gauge bosons with mass $\mu < 2m_\mu$, or to a mixture of electrons, muons and charged pions, appropriate for decays of gauge bosons with mass greater than $2m_\pi$. The relative abundance of e, μ and π in the mixed final state can be computed from the branching fractions of the decays, discussed in connection with eq. (4.8).

For intermediate values of the gauge boson mass, $2m_\mu < \mu \lesssim 2m_\pi$, we can use the branching ratios to interpolate between our maximum-allowed MH or best-fit SH boost factors for the $4e$ case and those of the fiducial $e + \mu + \pi$ case. The maximum allowed boost factors of the main halo complying with the ICS constraints are taken from table II. To estimate the best fit boost factors for the subhalos in the fiducial $e + \mu + \pi$ final state, we rescale the $4e$ results shown in table II by the ratio of best-fit boost factors for the main halo, in the MH-only scenario. These ratios are 118/110 for the Einasto profile and 119/113 for the isothermal, quite close to unity, and so the best-fit values of the SH boost factors hardly depend upon this scaling. More significant is the change in the best-fit mass, from $M = 1.0$ to 1.2 TeV, which enters into the computation of the Sommerfeld enhancement and the value of the gauge coupling ($\alpha_g \sim M$). We use the branching ratios to interpolate M as well. For the MH upper bounds in the small- and large-μ regions, we use the values from Table II, and interpolate similarly for intermediate μ.

4.5.4 Theoretical fits

For a given value of the gauge coupling α_g, we can determine the predicted boost factors as well as the desired values for each subhalo, as a function of the gauge boson mass μ, and similarly for the main halo, except here we have an upper bound on $\langle \bar{S} \rangle$ rather than a best-fit value. This bound in fact presents the biggest challenge to finding a working particle physics model. For α_g close to the thermal relic density value $\alpha_{g,\mathrm{th}}$, the predicted boost factor of the main halo far exceeds the bound $\langle \bar{S} \rangle \lesssim 30$, even if we try to decrease $\langle \bar{S} \rangle$ by reducing α_g via a large hidden Higgs content or by increasing the dispersion of the main halo. Fig. 4.13 illustrates the discrepancy for $\sum_i q_i^2 = 16$ and $V_{\max} = 277$ km/s. Lower values of $V_{\max}$ or $\sum_i q_i^2$ only make this tension worse.

As we mentioned above, even though it is not theoretically possible to make the gauge coupling weak enough to solve this problem, ironically one can rescue the scenario by *increasing* α_g beyond the thermal value, since this suppresses the relic density of the DM component we are interested in, and thus reduces the scattering rate. Allowing $\alpha_g = \sqrt{f}\alpha_{g,\mathrm{th}}$ decreases both the density of the leptophilic component and the effective boost factor by $1/f$. With $f \sim 50 - 500$, depending upon the shape of the main halo DM density profile, we can satisfy the constraint on the MH and still have a large enough boost in certain hypothetical nearby subhalos for them to supply the observed lepton excess. The minimum value of f that is needed is larger for a cuspy main halo.

We give two working examples in figure 4.14, one with $f = 500$ and $V_{\max} = 277$ km/s (the larger value advocated in ref. [150]) and assuming an Einasto profile for the main halo, and the other having $f = 50$ and $V_{\max} = 201$ km/s (the more standard assumption for the velocity dispersion), with an isothermal halo. In these figures the averaged boost factor $\langle \bar{S} \rangle$ of the relevant subhalos are plotted as solid lines, while the required values of $\langle \bar{S} \rangle$ are the dashed curves. Wherever these intersect represents a possible value of the gauge boson mass to consistently explain the observed lepton excess. At the same time, the main halo boost factor (lowest solid curve in the small-μ region) must lie below the black dashed lines to satifsy gamma ray constraints. The rationale for taking the larger value of $V_{\max}$ for the Einasto profile is that larger velocities help to suppress the boost factors and thus make it easier to satisfy the ICS constraint, so that we are not forced to choose an even larger value of f. The isothermal profile is less constrained.

In the first panel of fig. 4.14 with the Einasto profile, only subhalos SH4 and SH5 have large enough boost factors to ever reach the required values. There are many points of intersection, but mainly those for SH5 and in the mass range $\mu < 750$ MeV are consistent with the gamma ray bounds on the main halo. For the isothermal halo, these constraints are less stringent, and it is possible to find points of intersection using $f = 50$ for all five of the sample subhalos, although they are much more rare for SH1−SH3 than for SH4 and SH5. In this example, the intersection points that respect the ICS bound are restricted to $\mu \lesssim 1$ GeV. For larger values of f, all the boost factors will be further suppressed, and $\mu > 1$ GeV will become allowed for SH4 and SH5.

One advantage of requiring large f is that the corresponding dilution of the DM density by $1/f$ insures that the model satisfies stringent CMB constraints from annihilations in the early universe changing the optical depth [127, 152, 128], as pointed out in [131]. The CMB constraint is shown in fig. 4.15, along with the PAMELA/Fermi allowed regions from ref. [115] for $4e$ and 4μ final states. The $4e$ case is allowed by the CMB constraint, but 4μ is ruled out. Because our model has at most a fraction of 0.45 of muons in the final state, it is probably already safe, but the additional weakening of the bound by the factor $1/f$ ensures that this will be the case. Similarly, our scenario overcomes the no-go result of ref. [68], which pointed out that Sommerfeld enhanced annihilation in the early universe leads to constraints on the MH boost factor which are lower than those needed to explain the lepton anomalies. Our MH boost factor can satisfy these constraints since the MH is no longer considered to be the source of the excess leptons.

The Sommerfeld enhancement is nearly saturated for the low velocities of the subhalos at these large values of $\alpha_g \sim 0.1 - 0.35$, so their $\langle \bar{S} \rangle$ curves are nearly overlapping except at the smallest gauge boson masses. The main halo boost factor is not saturated on the other hand, and lies below the FSR bound for most values of μ. We have chosen the gauge couplings, parametrized by f, to nearly saturate the FSR bound. By taking larger α_g (larger f), the bounds could be satisfied by a larger margin. But this would also reduce the $\langle \bar{S} \rangle$ values of the subhalos by a similar amount, making it more difficult to get a large enough lepton signal from SH1−SH3. SH4 and SH5 would remain robust possible explanations.

4.6 Discussion and Conclusions

We have shown that gamma ray constraints on leptophilic annihilating dark matter are significantly stronger than in previous studies, when we take into account the contributions to inverse Compton scattering from primary and secondary electrons and positrons, before including excess leptons from the DM annihilation. We attribute part of this difference to the method of solving the diffusion equation (1) — fully numerical rather than semi-analytic — meaning that the (r, z) space-dependence of the diffusion coefficient is taken into account. The difference between the predicted and observed spectra of gamma rays is greatly reduced, leaving little room for new contributions. Because of this, even cored halos, which were allowed by other analyses, become excluded. However, we find that these constraints can be weakened and possibly overcome if annihilations in a nearby subhalo are the dominant source of anomalous leptons, rather than annihilations in the main galactic DM halo. In this way, the PAMELA/Fermi cosmic ray excesses can be explained, without violating bounds from the recent Fermi LAT diffuse gamma ray survey.

It must be admitted that the subhalo loophole we present is rather special. First, only atypically dense subhalos, relative to the sample provided by *Via Lactea II*, give a large enough boost factor (see fig. 4.8). Second, the subhalo would need to accidentally line up nearly with the galactic center in order for the ICS gamma rays associated with these leptons to be sufficiently hidden by the noisy background of the GC. Of course, had we neglected ICS contributions of background electrons, similar to previous studies, less fine tuning of the subhalo properties would be necessary. Also we do not require the subhalo to be particularly close; fig. 4.9 shows that the lepton flux only starts to fall at distances of ~ 3 kpc. Our finding could be regarded as a proof of concept. It is possible that the effects of unresolved substructure within the subhalo [85], which can increase the boost factor, would also make the scenario work more easily. On the positive side, there is the opportunity of testing whether there is such a nearby subhalo, since we predict the spectrum of ICS gamma rays it contributes (see fig. 4.10). A better understanding of backgrounds, for example from point sources, could make it possible to rule out the proposal. A detailed study of unresolved pulsars [153] may indeed close the gap further.

On the particle physics side, we have shown in detail that the subhalo scenario can be made consistent with one of the simplest models of leptophilic dark matter, where the DM is in a hidden sector that communicates with the standard model only through kinetic mixing with hypercharge of a new gauge boson in the GeV mass range. The relative couplings to leptons and charged pions are completely specified and the model has only two free parameters, the gauge coupling α_g and gauge boson mass μ (the DM mass M is fixed by fitting to the spectrum of anomalous $e^+ + e^-$). The gauge coupling is constrained by the relic density of the DM. The Sommerfeld enhancement factor is completely fixed by (α_g, μ, M) and the kinematical halo properties. We find (similarly to ref. [131]) that the predicted boost factor for the main halo is always *too large* to satisfy ICS constraints unless the leptophilic component of the DM is small, comprising a fraction of order $1/f = 0.02 - 0.002$ of the total DM. The small fraction can be achieved by assuming α_g is larger than the value required for the usual thermal abundance by the factor $f \sim 50 - 500$. This raises the interesting possibility that the DM that may be responsible for the cosmic ray anomalies is distinct from the dominant DM species that might be discovered by direct detection.

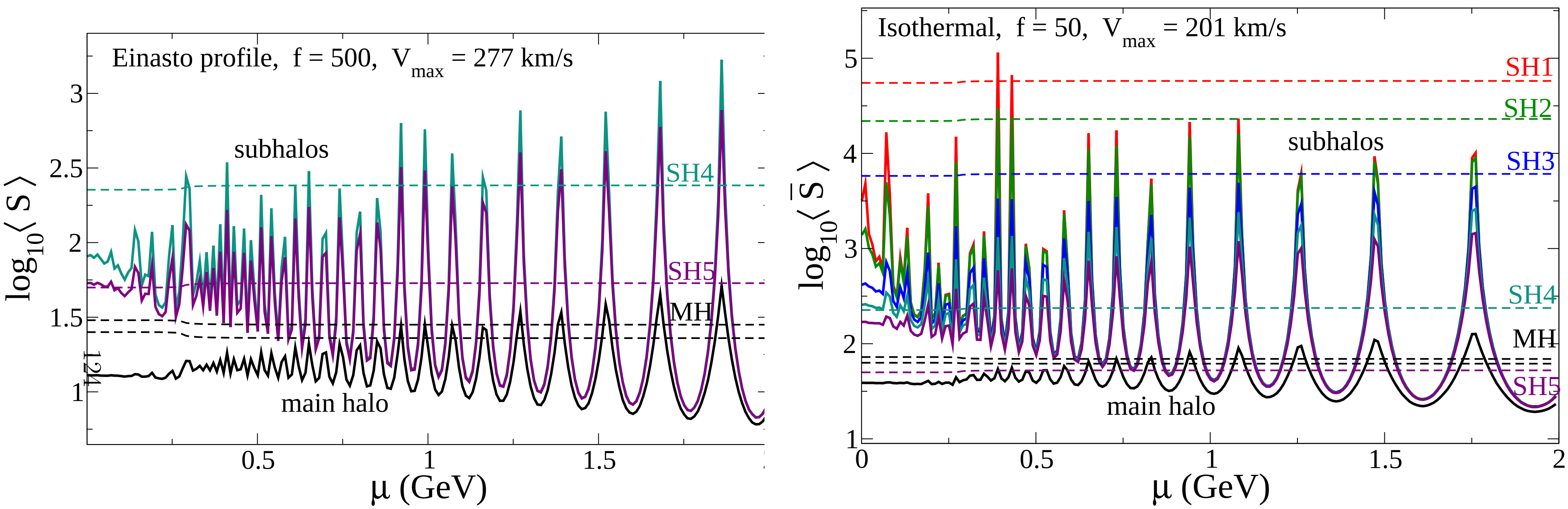

Figure 4.14: Predicted effective boost factors $\langle \bar{S} \rangle$ as a function of gauge boson mass (solid curves) and target values (or upper limit in case of main halo, dashed curves) to explain PAMELA/Fermi lepton observations and Fermi gamma ray constraints. Pair of dashed curves for main halo (MH) correspond respectively to 1 and 2σ upper limits. Left panel is for $f = 100$, $V_{\max} = 277$ km/s, Einasto main halo profile; right is for $f = 25$, $V_{,\max} = 201$ km/s, isothermal main halo profile. Subhalos are those of table 4.2. Points which satisfy all constraints are those where subhalo curves intersect their corresponding dashed line while the main halo curve lies below its dashed lines.

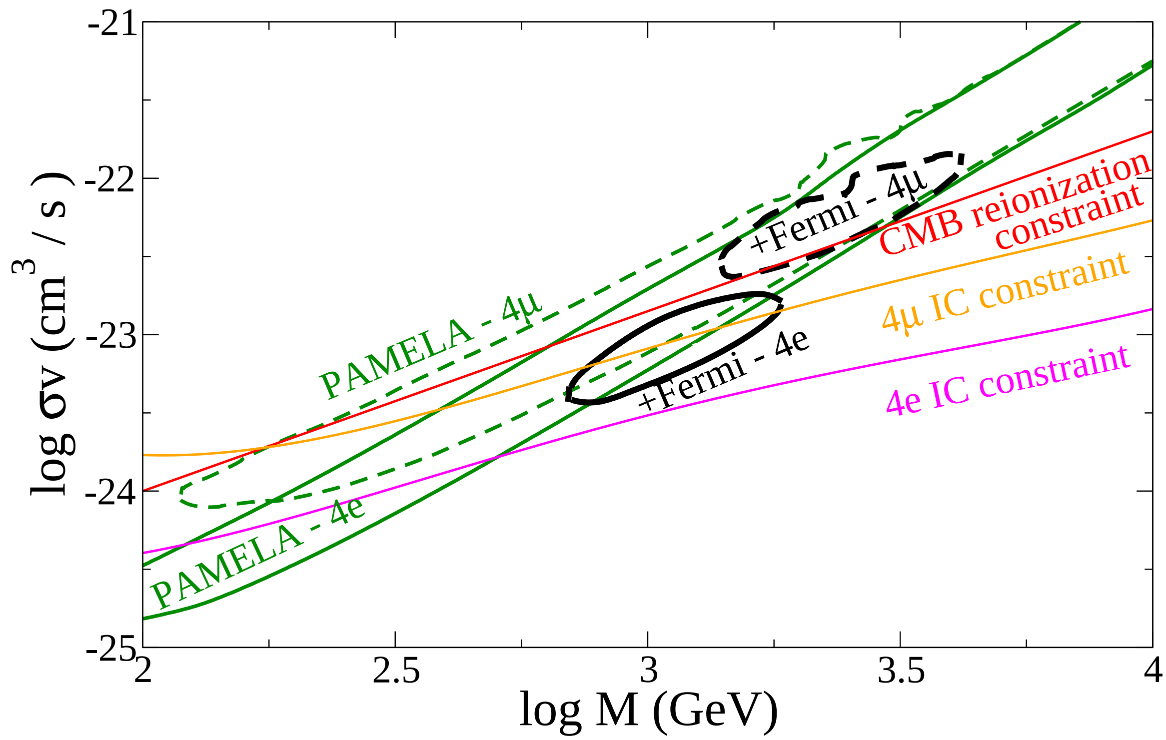

Figure 4.15: Allowed regions for PAMELA and Fermi excess leptons, and upper bounds from inverse Compton gamma rays, from ref. [115], for Einasto profile with $\alpha = 0.17$ and $r_s = 20$ kpc. CMB constraint is from ref. [152].

Chapter 5

Conclusions

We have studied two recently-observed anomalies in the cosmic ray composition of the Milky Way galaxy. First, an observation of 511 keV gamma-rays coming mainly from the galactic center, with a bulge-to-disk ratio that is higher than anything observed in the rest of the electromagnetic spectrum. This lack of correlation with other sources has puzzled observers for the past 40 years. We have shown that the expected distribution of particle dark matter can reproduce the correct morphology, provided that some mechanism exists for the DM particles to collide and release an e^+e^- pair. The significance of this result is on par with the best phenomenological fits to the INTEGRAL/SPI data, but with the advantages of 1) a physical mechanism; and 2) six fewer degrees of freedom required to perform the fit.

The second anomaly we examined is a rise in the positron fraction $e^+/(e^+ + e^-)$ above 10 GeV that is not consistent with the expected secondary cosmic ray flux. We have showed that by including the contribution of the large number of dark matter subhalos expected to be present in the Milky Way, a better fit to the $e^+ + e^-$ measurements can be obtained. This simultaneously lowers the overall flux of gamma rays from the galactic center. Unfortunately, this reduction is not sufficient to overcome the stringent upper limits from the Fermi-LAT experiment. We finally showed that a single close subhalo can provide the required $e^\pm$ flux, on the condition that a Sommerfeld-like enhancement exists to boost the cross-section sufficiently.

Given the strict limits on annihilating TeV-scale DM in our galaxy, in addition to the many assumptions required for the realization of the latter scenario, a dark matter explanation of the PAMELA excess is no longer among the front-runners. Indeed, recent studies favour a local astrophysical object, such as the Geminga pulsar, or a combination of local sources. However, until such a contribution is independently confirmed by other methods, such as a direct observation of the positron transport, the dark matter interpretation cannot be dismissed.

The existence of dark matter necessarily requires a new particle — or particles — not present in the standard model. The WIMP hypothesis, and more broadly the fact that the ratio of dark to baryonic matter is O(1), hints to a portal to the dark side at or above the electroweak scale. High-energy charge-neutral processes, such as matter-antimatter pair-creation, are therefore the ideal place to look for evidence of particle dark matter. The signals explored in this thesis constitute prime examples, in that their shapes and spectra naturally lend themselves to a dark matter explanation.

Future observations may help to constrain, strengthen or rule out these models: at high energies, stronger gamma-ray constraints from Fermi, and better models of background gammas will most likely constrain DM models even further. A true test will most likely come from precision modeling and imaging of astrophysical sources. On the 511 keV side, much more data will be needed to properly understand the morphology. The largest source of uncertainty lies in the galactic magnetic fields. Their strength determines the extent to which positrons propagate before annihilating. More data will of course strengthen the statistics of the model. Observations of the dwarf spheroidals can provide strong corroboration of the DM hypothesis, but current instruments are not sensitive enough for such observations. INTEGRAL/SPI still has five to ten years of observation, but no plans currently exist for a next-generation soft gamma-ray telescope, so it will surely be a decade or more before the required sensitivity of $\sim 10^{-6}$ ph s^{-1} can be attained.

Independent searches through direct production of DM in colliders, direct detection with underground experiments, as well as other indirect observations will therefore be required to corroborate the e^+e^- observations. The great number and variety of planned and ongoing experiments makes us optimistic that some light will be shed on the dark side over the course of the next ten to twenty years.

Appendix A

List of Acronyms

Acronym	**Definition**
B/D	Bulge-to-Disk (ratio)
BAO	Baryon Acoustic Oscillations
BF	Boost Factor
CGRO	Compton Gamma-Ray Observatory
CDM	Cold Dark Matter
CDMS	Cryogenic Dark Matter Search
CMB	Cosmic Microwave Background
CR	Cosmic Ray
CoGeNT	Coherent Germanium Neutrino Technology
CRESST	Cryogenic Rare Event Search with Superconducting Thermometers
DAMA/LIBRA	DArk MAtter/Large sodium Iodide Bulk for RAre processes
DM	Dark Matter
Fermi-LAT	Fermi Large Area Telescope
FSR	Final-State Radiation
GALPROP	GALactic PROPagation code
GC	Galactic Centre
HEAO	High Energy Astronomy Observatory
ICS	Inverse-Compton Scattering

INTEGRAL	INTErnational Gamma-Ray Astrophysics Laboratory
ISM	Interstellar Medium
ISRF	Interstellar Radiation Field
LHC	Large Hadron Collider
LMXRB	Low-Mass X-Ray Binary
MH	Main Halo
MLR	Maximum (log) Likelihood Ratio
NFW	Nevarro-Frenk-White
OSSE	Oriented Scintillation Spectrometer Experiment
PAMELA	Payload for Antimatter Matter Exploration and Light-nuclei Astrophysics
PICASSO	Project in Canada to Search for Supersymmetric Objects
PPB-BETS	Polar Patrol Balloon — Balloon-borne Electron Telescope with Scintillating fibers
PWN	Pulsar Wind Nebula
SCUBA	Self-Contained Underwater Breathing Apparatus
SH	Subhalo
SM	Standard Model
SMBH	Supermassive Black Hole
SNR	Supernova Remnant
SPI	SPectrometer for Integral
WIMP	Weakly-Interacting Massive Particle
XDM	eXcited Dark Matter

References

[1] Aaron C. Vincent, Pierrick Martin, and James M. Cline. Interacting dark matter contribution to the Galactic 511 keV gamma ray emission: constraining the morphology with INTEGRAL/SPI observations. *JCAP*, 1204:022, 2012.

[2] James M. Cline, Aaron C. Vincent, and Wei Xue. Leptons from Dark Matter Annihilation in Milky Way Subhalos. *Phys. Rev.*, D81:083512, 2010.

[3] Aaron C. Vincent, Wei Xue, and James M. Cline. Overcoming Gamma Ray Constraints with Annihilating Dark Matter in Milky Way Subhalos. *Phys.Rev.*, D82:123519, 2010.

[4] M. Kuhlen, P. Madau, and J. Silk. Exploring Dark Matter with Milky Way substructure. 2009.

[5] F. Zwicky. Die Rotverschiebung von extragalaktischen Nebeln. *Helvetica Physica Acta*, 6:110–127, 1933.

[6] F. Zwicky. On the Masses of Nebulae and of Clusters of Nebulae. *Ap. J.*, 86:217, October 1937.

[7] V. C. Rubin and W. K. Ford, Jr. Rotation of the Andromeda Nebula from a Spectroscopic Survey of Emission Regions. *Ap. J.*, 159:379, February 1970.

[8] V. C. Rubin, W. K. J. Ford, and N. . Thonnard. Rotational properties of 21 SC galaxies with a large range of luminosities and radii, from NGC 4605 /R = 4kpc/ to UGC 2885 /R = 122 kpc/. *Ap. J.*, 238:471–487, June 1980.

[9] Benoit Famaey and Stacy McGaugh. Modified Newtonian Dynamics: A Review. 2011.

[10] http://hubblesite.org/newscenter/archive/releases/2008/32.

[11] R. Amanullah, C. Lidman, D. Rubin, G. Aldering, P. Astier, et al. Spectra and Light Curves of Six Type Ia Supernovae at 0.511 ¡ z ¡ 1.12 and the Union2 Compilation. *Astrophys.J.*, 716:712–738, 2010.

[12] J. Zavala, Y.P. Jing, A. Faltenbacher, G. Yepes, Y. Hoffman, et al. The velocity function in the local environment from LCDM and LWDM constrained simulations. *Astrophys.J.*, 700:1779–1793, 2009.

[13] Samuel D. McDermott, Hai-Bo Yu, and Kathryn M. Zurek. Turning off the Lights: How Dark is Dark Matter? *Phys.Rev.*, D83:063509, 2011.

[14] David E. Kaplan, Markus A. Luty, and Kathryn M. Zurek. Asymmetric Dark Matter. *Phys.Rev.*, D79:115016, 2009.

[15] Leanne D. Duffy and Karl van Bibber. Axions as Dark Matter Particles. *New J.Phys.*, 11:105008, 2009.

[16] John Dubinski and R.G. Carlberg. The Structure of cold dark matter halos. *Astrophys.J.*, 378:496, 1991.

[17] Volker Springel et al. The Aquarius Project: the subhalos of galactic halos. *Mon. Not. Roy. Astron. Soc.*, 391:1685–1711, 2008.

[18] J. Diemand et al. Clumps and streams in the local dark matter distribution. *Nature*, 454:735–738, 2008.

[19] Paolo Salucci. Universal properties in galaxies and cored Dark Matter profiles. 2010.

[20] F. Governato, A. Zolotov, A. Pontzen, C. Christensen, S.H. Oh, et al. Cuspy No More: How Outflows Affect the Central Dark Matter and Baryon Distribution in Lambda CDM Galaxies. 2012.

[21] Patricia B. Tissera, Simon D.M. White, Susana Pedrosa, and Cecilia Scannapieco. Dark matter response to galaxy formation. 2009.

[22] Carlos A. Vera-Ciro, Laura V. Sales, Amina Helmi, Carlos S. Frenk, Julio F. Navarro, et al. The Shape of Dark Matter Haloes in the Aquarius Simulations: Evolution and Memory. 2011.

[23] G. Angloher, M. Bauer, I. Bavykina, A. Bento, C. Bucci, et al. Results from 730 kg days of the CRESST-II Dark Matter Search. *Eur.Phys.J.*, C72:1971, 2012.

[24] E. Aprile et al. The XENON100 Dark Matter Experiment. *Astropart.Phys.*, 35:573–590, 2012.

[25] C.E. Aalseth, P.S. Barbeau, J. Colaresi, J.I. Collar, J. Diaz Leon, et al. Search for an Annual Modulation in a P-type Point Contact Germanium Dark Matter Detector. *Phys.Rev.Lett.*, 107:141301, 2011.

[26] S. Archambault, F. Aubin, M. Auger, E. Behnke, B. Beltran, et al. Dark Matter Spin-Dependent Limits for WIMP Interactions on F-19 by PICASSO. *Phys.Lett.*, B682:185–192, 2009.

[27] Z. Ahmed et al. Results from a Low-Energy Analysis of the CDMS II Germanium Data. *Phys.Rev.Lett.*, 106:131302, 2011.

[28] Gilles Vertongen and Christoph Weniger. Hunting Dark Matter Gamma-Ray Lines with the Fermi LAT. *JCAP*, 1105:027, 2011.

[29] F. R. Johnson III, W. N.and Harnden and R. C. Jr.; Haymes. The Spectrum of Low-Energy Gamma Radiation from the Galactic-Center Region. *Astrophysical Journal*, 172:L1, 1979.

[30] M. Leventhal, C. J. MacCallum, and P. D. Stang. Detection of 511 keV positron annihilation radiation from the galactic center direction. *Ap.J.*, 225:L11–L14, October 1978.

[31] W. R. Purcell, L.-X. Cheng, D. D. Dixon, R. L. Kinzer, J. D. Kurfess, M. Leventhal, M. A. Saunders, J. G. Skibo, D. M. Smith, and J. Tueller. Osse mapping of galactic 511 kev positron annihilation line emission. *The Astrophysical Journal*, 491(2):725, 1997.

[32] Patrick Sizun, M. Casse, and S. Schanne. Continuum gamma-ray emission from light dark matter positrons and electrons. *Phys.Rev.*, D74:063514, 2006.

[33] P. Jean et al. Spi instrumental background characteristics. *Astronomy and Astrophysics*, 411:L107, 2003.

[34] G. Weidenspointner et al. First identication and modelling of spi background lines. *Astronomy and Astrophysics*, 411:L113, 2003.

[35] Nikos Prantzos. On the intensity and spatial morphology of the 511-kev emission in the milky way. *Astron.Astrophys.*, 449:869–878, 2006.

[36] Pierre Jean, J. Knodlseder, W. Gillard, N. Guessoum, K. Ferriere, et al. Spectral analysis of the galactic e+ e- annihilation emission. *Astron.Astrophys.*, 445:579–589, 2006.

[37] J. Knodlseder et al. The all-sky distribution of 511-keV electron positron annihilation emission. *Astron. Astrophys.*, 441:513–532, 2005.

[38] Laurent Bouchet, Jean-Pierre Roques, and Elisabeth Jourdain. On the morphology of the electron-positron annihilation emission as seen by SPI/INTEGRAL. *Astrophys.J.*, 720:1772–1780, 2010.

[39] G. Weidenspointner, G.K. Skinner, P. Jean, J. Knodlseder, P. von Ballmoos, R. Diehl, A. Strong, B. Cordier, S. Schanne, and C. Winkler. Positron astronomy with SPI/INTEGRAL. *New Astronomy Reviews*, 52(7-10):454 – 456, 2008.

[40] Roland Diehl, H. Halloin, K. Kretschmer, A.W. Strong, W. Wang, et al. 26al in the inner galaxy. *Astron.Astrophys.*, 449:1025–1031, 2006.

[41] N. Prantzos, C. Boehm, A.M. Bykov, R. Diehl, K. Ferriere, et al. The 511 keV emission from positron annihilation in the Galaxy. 2010.

[42] Georg Weidenspointner, Gerry Skinner, Pierre Jean, Jurgen Knodlseder, Peter von Ballmoos, et al. An asymmetric distribution of positrons in the Galactic disk revealed by gamma-rays. *Nature*, 451:159–162, 2008.

[43] Reba M. Bandyopadhyay, Joseph Silk, James E. Taylor, and Thomas J. Maccarone. On the Origin of the 511 keV Emission in the Galactic Centre. 2008.

[44] Gerry Skinner. The 511 kev sky as seen by integral/spi, cgro-osse and grs/smm combined. 22 March 2012.

[45] Pasquale D. Serpico. Astrophysical models for the origin of the positron 'excess'. 2011.

[46] Celine Boehm, Dan Hooper, Joseph Silk, Michel Casse, and Jacques Paul. MeV dark matter: Has it been detected? *Phys.Rev.Lett.*, 92:101301, 2004.

[47] Douglas P. Finkbeiner and Neal Weiner. Exciting Dark Matter and the INTEGRAL/SPI 511 keV signal. *Phys.Rev.*, D76:083519, 2007.

[48] Maxim Pospelov and Adam Ritz. The galactic 511 keV line from electroweak scale WIMPs. *Phys.Lett.*, B651:208–215, 2007.

[49] Nima Arkani-Hamed, Douglas P. Finkbeiner, Tracy R. Slatyer, and Neal Weiner. A Theory of Dark Matter. *Phys.Rev.*, D79:015014, 2009.

[50] Fang Chen, James M. Cline, Anthony Fradette, Andrew R. Frey, and Charles Rabideau. Exciting dark matter in the galactic center. *Phys.Rev.*, D81:043523, 2010.

[51] Fang Chen, James M. Cline, and Andrew R. Frey. A new twist on excited dark matter: implications for INTEGRAL, PAMELA/ATIC/PPB-BETS, DAMA. *Phys. Rev.*, D79:063530, 2009.

[52] James M. Cline, Andrew R. Frey, and Fang Chen. Metastable dark matter mechanisms for INTEGRAL 511 keV γ rays and DAMA/CoGeNT events. 2010.

[53] Rob Morris and Neal Weiner. Low Energy INTEGRAL Positrons from eXciting Dark Matter. 2011.

[54] S. Torii et al. High-energy electron observations by PPB-BETS flight in Antarctica. 2008.

[55] J. Chang, J.H. Adams, H.S. Ahn, G.L. Bashindzhagyan, M. Christl, et al. An excess of cosmic ray electrons at energies of 300-800 GeV. *Nature*, 456:362–365, 2008.

[56] Oscar Adriani et al. An anomalous positron abundance in cosmic rays with energies 1.5-100 GeV. *Nature*, 458:607–609, 2009.

[57] Aous A. Abdo et al. Measurement of the Cosmic Ray e+ plus e- spectrum from 20 GeV to 1 TeV with the Fermi Large Area Telescope. *Phys. Rev. Lett.*, 102:181101, 2009.

[58] M. Ackermann et al. Measurement of separate cosmic-ray electron and positron spectra with the Fermi Large Area Telescope. *Phys.Rev.Lett.*, 108:011103, 2012. 5 figures, 1 table, revtex 4.1.

[59] Aous A. Abdo et al. Measurement of the Cosmic Ray e+ plus e- spectrum from 20 GeV to 1 TeV with the Fermi Large Area Telescope. *Phys.Rev.Lett.*, 102:181101, 2009.

[60] Marco Cirelli, Mario Kadastik, Martti Raidal, and Alessandro Strumia. Model-independent implications of the e+, e-, anti-proton cosmic ray spectra on properties of Dark Matter. *Nucl. Phys.*, B813:1–21, 2009.

[61] Maxim Pospelov and Adam Ritz. Astrophysical Signatures of Secluded Dark Matter. *Phys. Lett.*, B671:391–397, 2009.

[62] Ilias Cholis, Douglas P. Finkbeiner, Lisa Goodenough, and Neal Weiner. The PAMELA Positron Excess from Annihilations into a Light Boson. 2008.

[63] Ilias Cholis, Gregory Dobler, Douglas P. Finkbeiner, Lisa Goodenough, and Neal Weiner. The Case for a 700+ GeV WIMP: Cosmic Ray Spectra from ATIC and PAMELA. 2008.

[64] Patrick Meade, Michele Papucci, Alessandro Strumia, and Tomer Volansky. Dark Matter Interpretations of the Electron/Positron Excesses after FERMI. 2009.

[65] Fang Chen, James M. Cline, and Andrew R. Frey. Nonabelian dark matter: models and constraints. 2009.

[66] Gordon Kane, Ran Lu, and Scott Watson. PAMELA Satellite Data as a Signal of Non-Thermal Wino LSP Dark Matter. 2009.

[67] Michael Kuhlen, Jurg Diemand, and Piero Madau. The Dark Matter Annihilation Signal from Galactic Substructure: Predictions for GLAST. 2008.

[68] Jonathan L. Feng, Manoj Kaplinghat, and Hai-Bo Yu. Sommerfeld Enhancements for Thermal Relic Dark Matter. 2010.

[69] Steen Hannestad and Thomas Tram. Sommerfeld Enhancement of DM Annihilation: Resonance Structure, Freeze-Out and CMB Spectral Bound. *JCAP*, 1101:016, 2011.

[70] E. A. Helder, J. Vink, C. G. Bassa, A. Bamba, J. A. M. Bleeker, S. Funk, P. Ghavamian, K. J. van der Heyden, F. Verbunt, and R. Yamazaki. Measuring the cosmic-ray acceleration efficiency of a supernova remnant. *Science*, 325(5941):719–722, 2009.

[71] Andrew W. Strong, Igor V. Moskalenko, and Vladimir S. Ptuskin. Cosmic-ray propagation and interactions in the Galaxy. *Ann.Rev.Nucl.Part.Sci.*, 57:285–327, 2007.

[72] Patrick Meade, Michele Papucci, and Tomer Volansky. Dark Matter Sees The Light. *JHEP*, 0912:052, 2009.

[73] galprop.stanford.edu.

[74] http://www.desy.de/ maccione/DRAGON/index.html.

[75] Edward A. Baltz and Joakim Edsjo. Positron Propagation and Fluxes from Neutralino Annihilation in the Halo. *Phys. Rev.*, D59:023511, 1998.

[76] A.W. Strong. Interstellar gamma rays and cosmic rays: new insights from Fermi-LAT AND INTEGRAL. 2011.

[77] http://fermi.gsfc.nasa.gov/cgi bin/ssc/LAT/WeeklyFiles.cgi.

[78] Dan Hooper, Pasquale Blasi, and Pasquale Dario Serpico. Pulsars as the Sources of High Energy Cosmic Ray Positrons. *JCAP*, 0901:025, 2009.

[79] Dmitry Malyshev, Ilias Cholis, and Joseph Gelfand. Pulsars versus Dark Matter Interpretation of ATIC/PAMELA. *Phys.Rev.*, D80:063005, 2009.

[80] V. Barger, Y. Gao, Wai Yee Keung, D. Marfatia, and G. Shaughnessy. Dark matter and pulsar signals for Fermi LAT, PAMELA, ATIC, HESS and WMAP data. *Phys.Lett.*, B678:283–292, 2009.

[81] T. Kamae, S.-H. Lee, L. Baldini, F. Giordano, M.-H. Grondin, et al. Cosmic Ray $e^+/(e^- + e^+)$ and p-bar/p Ratios Explained by an Injection Model Based on Gamma-ray Observations. 2010.

[82] Hasan Yuksel, Matthew D. Kistler, and Todor Stanev. TeV Gamma Rays from Geminga and the Origin of the GeV Positron Excess. *Phys.Rev.Lett.*, 103:051101, 2009.

[83] Pasquale Blasi. The origin of the positron excess in cosmic rays. *Phys.Rev.Lett.*, 103:051104, 2009. 4 Pages, 2 figures.

[84] Michael Schubnell. The Cosmic-Ray Positron and Electron Excess: An Experimentalist's Point of View. 2009.

[85] Jo Bovy. Substructure Boosts to Dark Matter Annihilation from Sommerfeld Enhancement. 2009.

[86] Michael Kuhlen. The Dark Matter Annihilation Signal from Dwarf Galaxies and Subhalos. 2009.

[87] Matthew D. Kistler and Jennifer M. Siegal-Gaskins. Gamma-ray signatures of annihilation to charged leptons in dark matter substructure. 2009.

[88] Shin'ichiro Ando. Gamma-ray background anisotropy from galactic dark matter substructure. *Phys. Rev.*, D80:023520, 2009.

[89] Pierre Brun, Timur Delahaye, Jurg Diemand, Stefano Profumo, and Pierre Salati. The cosmic ray lepton puzzle in the light of cosmological N-body simulations. *Phys. Rev.*, D80:035023, 2009.

[90] Michael Kuhlen and Dmitry Malyshev. Model in-dependence of electron and positron flux from Dark Matter. *Phys. Rev.*, D79:123517, 2009.

[91] Tracy R. Slatyer, Natalia Toro, and Neal Weiner. The Effect of Local Dark Matter Substructure on Constraints in Sommerfeld-Enhanced Models. 2011. 17 pages, 7 figures, submitted to PRD. v2 adds the KITP preprint number and a comment on accelerator searches for light gauge bosons.

[92] Eugene Churazov, R. Sunyaev, S. Sazonov, M. Revnivtsev, and D. Varshalovich. Positron annihilation spectrum from the Galactic Center region observed by SPI/INTEGRAL. *Mon.Not.Roy.Astron.Soc.*, 357:1377–1386, 2005.

[93] John F. Beacom and Hasan Yuksel. Stringent constraint on galactic positron production. *Phys.Rev.Lett.*, 97:071102, 2006.

[94] R. Bernabei, P. Belli, F. Cappella, R. Cerulli, C.J. Dai, et al. New results from DAMA/LIBRA. *Eur.Phys.J.*, C67:39–49, 2010.

[95] Yago Ascasibar, P. Jean, C. Boehm, and J. Knoedlseder. Constraints on dark matter and the shape of the Milky Way dark halo from the 511-keV line. *Mon.Not.Roy.Astron.Soc.*, 368:1695–1705, 2006.

[96] Zainul Abidin, Andrei Afanasev, and Carl E. Carlson. Positron production scenarios and the angular profile of the galactic center 511-keV line. 2010.

[97] Georg Weidenspointner, J. Knoedlseder, P. Jean, G.K. Skinner, J.-P. Roques, et al. The sky distribution of 511-keV positron annihilation line emission as measured with INTEGRAL/SPI. 2007.

[98] K.-W. Chan and R. E. Lingenfelter. Positrons from supernovae. *"Astrophys. J."*, 405:614–636, March 1993.

[99] Pierrick Martin, Jacco Vink, Sarka Jiraskova, Pierre Jean, and Roland Diehl. Annihilation emission from young supernova remnants. 2010.

[100] J. Diemand, M. Kuhlen, P. Madau, M. Zemp, B. Moore, et al. Clumps and streams in the local dark matter distribution. *Nature*, 454:735–738, 2008.

[101] M. Kuhlen, P. Madau, and J. Silk. Exploring Dark Matter with Milky Way substructure. *Science*, 325:970–973, 2009.

[102] P. Salucci, F. Nesti, G. Gentile, and C.F. Martins. The dark matter density at the Sun's location. *Astron.Astrophys.*, 523:A83, 2010.

[103] F. J. Kerr and Donald Lynden-Bell. Review of galactic constants. *Mon.Not.Roy.Astron.Soc.*, 221:1023, 1986.

[104] Charles Picciotto and Maxim Pospelov. Unstable relics as a source of galactic positrons. *Phys.Lett.*, B605:15–25, 2005.

[105] J.C. Higdon, R.E. Lingenfelter, and R.E. Rothschild. The Galactic Positron Annihilation Radiation; The Propagation of Positrons in the Interstellar Medium. *Astrophys.J.*, 698:350–379, 2009.

[106] P. Jean, W. Gillard, A. Marcowith, and K. Ferriere. Positron transport in the interstellar medium. 2009.

[107] Ji-Haeng Huh, Jihn E. Kim, Jong-Chul Park, and Seong Chan Park. Galactic 511 keV line from MeV milli-charged dark matter. *Phys.Rev.*, D77:123503, 2008.

[108] Annie C. Robin, C. Reyle, S. Derriere, and S. Picaud. A Synthetic view on structure and evolution of the Milky Way. *Astron.Astrophys.*, 409:523, 2003.

[109] James M. Cline and Andrew R. Frey. Light dark matter versus astrophysical constraints. *Phys.Lett.*, B706:384–388, 2012.

[110] Torsten Bringmann, Fiorenza Donato, and Roberto A. Lineros. Radio data and synchrotron emission in consistent cosmic ray models. 2011.

[111] C.Moni Bidin, G. Carraro, R.A. Mendez, and W.F. van Altena. No evidence for a dark matter disk within 4 kpc from the Galactic plane. *Astrophys.J.*, 724:L122–L126, 2010.

[112] Jose Luis G. Pestana and Donald H. Eckhardt. The Futile Search for Galactic Disk Dark Matter. *Astrophys.J.*, 722:L70–L74, 2010.

[113] Oscar Adriani et al. An anomalous positron abundance in cosmic rays with energies 1.5.100 GeV. *Nature*, 458:607–609, 2009.

[114] Marco Cirelli, Paolo Panci, and Pasquale D. Serpico. Diffuse gamma ray constraints on annihilating or decaying Dark Matter after Fermi. 2009.

[115] Michele Papucci and Alessandro Strumia. Robust implications on Dark Matter from the first FERMI sky gamma map. 2009.

[116] A. W. Strong and I. V. Moskalenko. Propagation of cosmic-ray nucleons in the Galaxy. *Astrophys. J.*, 509:212–228, 1998.

[117] Melanie Simet and Dan Hooper. Astrophysical Uncertainties in the Cosmic Ray Electron and Positron Spectrum From Annihilating Dark Matter. *JCAP*, 0908:003, 2009.

[118] David Maurin, Richard Taillet, and Fiorenza Donato. New results on source and diffusion spectral features of Galactic cosmic rays: I- B/C ratio. *Astron. Astrophys.*, 394:1039–1056, 2002.

[119] J. J. Engelmann, P. Ferrando, A. Soutoul, P. Goret, and E. Juliusson. Charge composition and energy spectra of cosmic-ray for elements from Be to NI - Results from HEAO-3-C2. *Astron. Astrophys.*, 233:96–111, 1990.

[120] http://www.ucolick.org/ diemand/vl/data.html.

[121] John David March-Russell and Stephen Mathew West. WIMPonium and Boost Factors for Indirect Dark Matter Detection. *Phys.Lett.*, B676:133–139, 2009.

[122] Massimiliano Lattanzi and Joseph I. Silk. Can the WIMP annihilation boost factor be boosted by the Sommerfeld enhancement? *Phys.Rev.*, D79:083523, 2009.

[123] Troy A. Porter and A. W. Strong. A new estimate of the Galactic interstellar radiation field between 0.1 microns and 1000 microns. 2005.

[124] Junji Hisano, Shigeki. Matsumoto, Mihoko M. Nojiri, and Osamu Saito. Non-perturbative effect on dark matter annihilation and gamma ray signature from galactic center. *Phys.Rev.*, D71:063528, 2005.

[125] Marco Cirelli, Alessandro Strumia, and Matteo Tamburini. Cosmology and Astrophysics of Minimal Dark Matter. *Nucl.Phys.*, B787:152–175, 2007.

[126] Francis-Yan Cyr-Racine, Stefano Profumo, and Kris Sigurdson. Protohalo Constraints to the Resonant Annihilation of Dark Matter. 2009.

[127] Gert Huetsi, Andi Hektor, and Martti Raidal. Constraints on leptonically annihilating Dark Matter from reionization and extragalactic gamma background. 2009.

[128] Tracy R. Slatyer, Nikhil Padmanabhan, and Douglas P. Finkbeiner. CMB Constraints on WIMP Annihilation: Energy Absorption During the Recombination Epoch. *Phys. Rev.*, D80:043526, 2009.

[129] Marc Kamionkowski, Savvas M. Koushiappas, and Michael Kuhlen. Galactic Substructure and Dark Matter Annihilation in the Milky Way Halo. *Phys.Rev.*, D81:043532, 2010.

[130] Alessandro Strumia. Dark matter interpretations of the cosmic-ray e+- excesses. *Prog. Theor. Phys. Suppl.*, 180:128–134, 2010.

[131] Marco Cirelli and James M. Cline. Can multistate dark matter annihilation explain the high- energy cosmic ray lepton anomalies? 2010.

[132] Gert Hutsi, Andi Hektor, and Martti Raidal. Implications of the Fermi-LAT diffuse gamma-ray measurements on annihilating or decaying Dark Matter. *JCAP*, 1007:008, 2010.

[133] T. Delahaye et al. Galactic secondary positron flux at the Earth. *Astron. Astrophys.*, 501:821–833, 2009.

[134] Riccardo Catena and Piero Ullio. A novel determination of the local dark matter density. 2009.

[135] Paolo Salucci and Andreas Burkert. Dark Matter Scaling Relations. *Astrophys. J.*, 537:L9–L12, 2000.

[136] Ilias Cholis, Lisa Goodenough, and Neal Weiner. High Energy Positrons and the WMAP Haze from Exciting Dark Matter. *Phys. Rev.*, D79:123505, 2009.

[137] Brandon Anderson, Michael Kuhlen, Robert Johnson, Piero Madau, and Juerg Diemand. Fermi-LAT Sensitivity to Dark Matter Annihilation in Via Lactea II Substructure. *Astrophys. J.*, 718:899–904, 2010.

[138] Andreas Birkedal, Konstantin T. Matchev, Maxim Perelstein, and Andrew Spray. Robust gamma ray signature of WIMP dark matter. 2005.

[139] G. R. Blumenthal and R. J. Gould. Bremsstrahlung, synchrotron radiation, and compton scattering of high-energy electrons traversing dilute gases. *Rev. Mod. Phys.*, 42:237–270, 1970.

[140] T. A. Porter and for the Fermi LAT Collaboration. Fermi LAT Measurements of the Diffuse Gamma-Ray Emission at Intermediate Galactic Latitudes. 2009.

[141] Troy A. Porter, Igor V. Moskalenko, Andrew W. Strong, Elena Orlando, and Laurent Bouchet. Inverse Compton Origin of the Hard X-Ray and Soft Gamma-Ray Emission from the Galactic Ridge. *Astrophys. J.*, 682:400–407, 2008.

[142] Ilias Cholis et al. The Fermi gamma-ray spectrum of the inner galaxy: Implications for annihilating dark matter. 2009.

[143] Anthony G. A. Brown. Learning about Galactic structure with Gaia astrometry. *AIP Conf. Proc.*, 1082:209–215, 2008.

[144] Matthew G. Walker et al. Velocity Dispersion Profiles of Seven Dwarf Spheroidal Galaxies. 2007.

[145] A. A. Abdo et al. Observations of Milky Way Dwarf Spheroidal galaxies with the Fermi-LAT detector and constraints on Dark Matter models. *Astrophys. J.*, 712:147–158, 2010.

[146] A. A. Abdo et al. Constraints on Cosmological Dark Matter Annihilation from the Fermi-LAT Isotropic Diffuse Gamma-Ray Measurement. *JCAP*, 1004:014, 2010.

[147] M. Ackermann et al. Searches for Cosmic-Ray Electron Anisotropies with the *Fermi* Large Area Telescope. 2010.

[148] S. Cassel. Sommerfeld factor for arbitrary partial wave processes. *J. Phys.*, G37:105009, 2010.

[149] Tracy R. Slatyer. The Sommerfeld enhancement for dark matter with an excited state. *JCAP*, 1002:028, 2010.

[150] Christopher Savage, Katherine Freese, Paolo Gondolo, and Douglas Spolyar. Compatibility of DAMA/LIBRA dark matter detection with other searches in light of new Galactic rotation velocity measurements. *JCAP*, 0909:036, 2009.

[151] Jesus Zavala, Mark Vogelsberger, and Simon D. M. White. Relic density and CMB constraints on dark matter annihilation with Sommerfeld enhancement. *Phys. Rev.*, D81:083502, 2010.

[152] Marco Cirelli, Fabio Iocco, and Paolo Panci. Constraints on Dark Matter annihilations from reionization and heating of the intergalactic gas. *JCAP*, 0910:009, 2009.

[153] Alex Geringer-Sameth and Savvas M. Koushiappas. Extracting the unresolved pulsar contribution to the gamma-ray background. *Mon.Not.Roy.Astron.Soc.*, 421:1813–1824, 2012.